

Alma Mater Studiorum - Università di Bologna

**DOTTORATO DI RICERCA IN
GEOFISICA
CICLO 33**

Settore Concorsuale: 04/A4 - GEOFISICA

Settore Scientifico Disciplinare: GEO/10 - GEOFISICA DELLA TERRA SOLIDA

**THE MOHO REFLECTIVITY FROM AMBIENT
SEISMIC NOISE AUTOCORRELATIONS
BENEATH THE WESTERN ALPS**

Presentata da:
Tahira Nicole Ashruf

Coordinatore Dottorato:
Prof.ssa Nadia Pinaridi

Supervisore:
Dott. Andrea Morelli

Co-supervisore:
Prof.ssa Maria Elina Belardinelli

Esame finale anno 2022

Abstract

The lower crustal structure beneath the Western Alps – including the Moho – bears the signature of past and present geodynamic processes. It has been the subject of many studies until now. However, its current knowledge still leaves significant open questions. In order to derive new information, independent from previous determinations, here I wish to address this topic using a different method — ambient seismic noise autocorrelation — that is for the first time applied to reveal Moho depth in the Western Alps. Moho reflections are identified by picking reflectivity changes in ambient seismic noise autocorrelations. I apply two different techniques to pick such reflectivity changes. The first technique is an automatic method to extract the local maxima of the second derivative envelope of the autocorrelation stacks inside an *a priori* time window based on prior Moho information. The second technique finds a change in reflectivity in the stack of daily autocorrelations. The seismic data is retrieved from more than 200 broadband seismic stations, from the dense China–Italy–France Alps (CIFALPS) linear seismic network, and from a subset of the wide large-scale AlpArray Seismic Network (AASN). The automatically-picked reflectivity changes along the CIFALPS transect in the southwestern Alps show the best results in the 0.5–1 Hz frequency band. The autocorrelation reflectivity profile of the CIFALPS transect shows a steeper subduction profile — as compared to other studies — ~ 55 to ~ 70 km, of the European Plate underneath the Adriatic Plate. The dense spacing of the CIFALPS network facilitates the detection of lateral continuity of crustal structure, and of the Ivrea mantle wedge reaching shallow crustal depths in the southwestern Alps. The data of the AASN stations are filtered in the 0.4–1 and 0.5–1 Hz frequency bands. Although the majority of the stations give the same Moho depth for the different frequency bands, the few stations with different Moho depths shows the care that has to be taken when choosing the frequency band for filtering the autocorrelation stacks. The new Moho depth maps by using the AASN stations are a compilation of the first and second picked reflectivity changes based on the background information. The results show the complex crust–mantle structure with clear differences between the northwestern and southwestern Alps.

Contents

Abstract	i
1 Introduction	1
1.1 Thesis overview	3
2 Seismic background information	5
2.1 Western Alpine system	5
2.2 Crustal-scale profiles surrounding the CIFALPS profile	6
2.3 Previous seismological studies on the CIFALPS profile	7
3 Seismic interferometry: theory	11
3.1 1D reflected-wave interferometry	11
4 The Moho reflectivity of the subduction beneath the Southwestern Alps from ambient seismic noise autocorrelations	15
4.1 Introduction	16
4.1.1 Tectonic background	16
4.1.2 Seismic interferometry	17
4.1.3 Applications of seismic ambient noise autocorrelation	18
4.1.4 Research aim and overview	18
4.2 Data and Method	19
4.2.1 Data	19
4.2.2 Ambient noise frequency ranges	19
4.2.3 Autocorrelation workflow	21

4.2.4	Moho reflectivity from autocorrelation stacks	23
4.3	Results	26
4.3.1	Autocorrelation stacks and temporal stability	26
4.3.2	Picked arrival times of the Moho reflectivity	30
4.3.3	Moho reflectivity across the CIFALPS profile	35
4.4	Discussion	40
4.4.1	Moho reflectivity from ambient noise autocorrelation	40
4.4.2	Preferred frequency band	43
4.4.3	Lithospheric structures from ambient noise autocorrelation	45
4.4.4	Intracrustal discontinuity from ambient noise autocorrelation	47
4.5	Conclusions	49
4.6	Supplementary Material	50
5	Moho structure of the Western Alps from seismic noise autocorrelation of AlpArray data	63
5.1	Introduction	64
5.1.1	Moho reflectivity from ambient noise autocorrelation	64
5.1.2	Research aim and overview	66
5.2	Data and Method	66
5.2.1	AlpArray Seismic Network	66
5.2.2	Ambient noise autocorrelation	67
5.2.3	Reflectivity changes related to the Moho reflection	68
5.3	Results	69
5.3.1	Picked reflectivity changes	69
5.3.2	<i>P</i> -wave reflectivity Western Alps	70
5.3.3	Geological setting: European basement, External massifs	83
5.4	Discussion	83
5.5	Conclusions	91
6	Conclusions	93
	Bibliography	95
	Appendices	103

A Station list: CIFALPS	105
B Station list: AASN	107
Acknowledgements	113
Curriculum Vitae	115

Chapter 1

Introduction

Our home, planet Earth, is made up of three principle layers: the crust, the mantle and the core. The Earth's crust only makes up 1% of Earth's volume (Robertson, 2001), and yet is the home of our natural resources, such as oil and gas, and geological hazards. In addition, the Earth's crust plays an important part in the global climate by being one of the largest reservoir for CO₂ (e.g. Zhang & Zindler, 1993). Despite its importance, it was only in 1909 that the croatian scientist Andrija Mohorovičić was able to calculate the crustal thickness, based on evidence from seismic waves (Mohorovičić, 1910). The boundary between the Earth's crust and the underlying layer, Earth's mantle, is called the Mohorovičić discontinuity in honor of Andrija Mohorovičić.

Earth scientists (e.g. Spada et al., 2013) have studied the Mohorovičić (Moho) topography extensively underneath mountain ranges as part of understanding the complex mountain building process. The Alpine mountain range is one of the greatest mountain belt on Earth and is situated between a number of densely populated European countries. This mountain range have seen in the last millennium strong earthquakes with magnitude 5.0 or greater that resulted in enormous human fatalities and economic damages (e.g. Akinci et al., 2004). Imaging the Earth structures, such as the Moho, of the Alps plays an important role into understanding the geodynamical processes that causes the seismically active and hazardous regions of Europe.

The great Alpine orogenic belt is a result of the European and Adriatic plates converging towards each other in a process marked by subduction, accretion and transformation (e.g. Handy et al., 2010; van Hinsbergen et al., 2020). This complex collision has resulted into complex crust–mantle structures, such as varying Moho depths along the subduction zones of the Western Alps. Zhao et al. (2015) studied the subduction zone of the southwestern Alps and imaged depths greater than 70 km for the Moho. However, Kästle et al. (2018) reaches a max Moho depth of 60 km and Beller et al. (2018) images a flatter slope of the subducting Moho. The

seismological studies carried out in the Western Alps to study the crust–mantle structures have used various types of techniques and data, such as active seismic data (e.g. Grellet et al., 1993), earthquake data (e.g. Lombardi et al., 2008) or ambient seismic noise data between two receivers (e.g. Kästle et al., 2018). Despite the different techniques used, the results regarding the depth and extent of the European Plate beneath the Adriatic plate remains controversial. The solving of said controversies, as well as the understanding of the geodynamics behind the seismic hazard prone regions are important reasons for imaging the crust–mantle structures more accurately. Therefore, we have studied the complex Moho in the southwestern Alps (Ashruf & Morelli, 2022) through ambient seismic noise autocorrelation that have never been implemented before in this region.

In the last decade, the ambient noise autocorrelation method of vertical seismic records has been used to retrieve the P -wave reflectivity response of the Earth structure beneath one receiver (e.g. Oren & Nowack, 2016; Becker & Knapmeyer-Endrun, 2018). The theoretical framework of this method, seismic interferometry, was first introduced by Claerbout (1968) for acoustic waves in 1-D media. Ambient noise autocorrelations has not only been used to map the Moho discontinuity (e.g. Tibuleac & von Seggern, 2012; Gorbatov et al., 2013), but also to study sedimentary basins (e.g. Romero & Schimmel, 2018; Viens et al., 2022), subduction zones (e.g. Ito et al., 2012), fault-zones (Taylor et al., 2016) and the lithosphere-asthenosphere boundary (Kennett, 2015). The main goal of this thesis is to image the complex Moho discontinuity in the Western Alps through ambient noise autocorrelation.

The choice of frequency band to filter the ambient noise autocorrelations is important since previous studies have shown that the ability to detect the Moho-reflected P -waves varies for different frequency bands. In Nevada, the Moho reflections have been extracted from the 0.5–1 Hz (Tibuleac & von Seggern, 2012) and 0.2–0.75 Hz (Oren & Nowack, 2016) frequency bands. In Australia, the Moho reflections are extracted from different cut-off frequencies in the 0.5–4 Hz band (e.g. Gorbatov et al., 2013; Kennett, 2015). In Central Europe, the Moho depth is extracted in the 1–2 Hz frequency band by Becker & Knapmeyer-Endrun (2018). The different frequency ranges used in previous studies and the fact that ambient noise autocorrelation has never been used in the Western Alps to image the Moho discontinuity leads to the following research question: *In which frequency range of the ambient noise autocorrelations are the P -wave reflections detectable that are associated to the Moho discontinuity in the Western Alps?*

The ambient noise autocorrelation method has shown the ability to image the Moho discontinuity in different regions. However, it is still debatable whether the Moho-reflected P -waves are associated to a prominent reflector (e.g. Tibuleac & von Seggern, 2012; Mroczek & Tilmann, 2021) or change in reflectivity—amplitude or frequency changes— along the autocorrelation stacks (e.g. Kennett et al., 2015; Becker & Knapmeyer-Endrun, 2018). This discrepancy gives rise to the second

research question: *Are the Moho reflections from ambient noise autocorrelation in the Western Alps related to reflectivity changes or clear pulses?*

Synthetic tests (e.g. Gorbatov et al., 2013; Mroczek & Tilmann, 2021) have shown that several phases of the ambient noise autocorrelation are not related to direct reflections. These phases have shown in previous studies (e.g. Kennett et al., 2015; Becker & Knapmeyer-Endrun, 2018) to cause bias in detecting the Moho-reflected P -waves without prior crust–mantle information. However, identifying the Moho reflections from ambient seismic noise autocorrelations independently of prior information is important in areas that often show controversial results, e.g. subduction zones. Therefore, this importance give rise to the third research question: *Can the Moho reflections from ambient noise autocorrelations in the Western Alps be detected independently of prior crust–mantle information?*

1.1 Thesis overview

To image the complex Moho discontinuity in the Western Alps through ambient noise autocorrelations and give answers to the research questions, the thesis is set up into different chapters. In chapter 2, an overview is given on the seismic background information of the Western Alps with specification on the crust–mantle profiles in the southwestern Alps. In chapter 3, the seismic interferometry theory behind ambient noise autocorrelations is presented. In chapter 4 and 5, the ambient seismic noise data of, respectively, the CIFALPS and AlpArray networks are used to image the Moho discontinuity in the Western Alps. Chapter 4 presents work that is published as Ashruf & Morelli (2022). Chapter 5 presents the research of the enlarged study area — complete Western Alps — of the Moho discontinuity that is the subject of a paper in preparation (Ashruf & Morelli, in preparation). At last, general conclusions are given in chapter 6.

Seismic background information

To understand and interpret the reflections obtained from ambient noise autocorrelation, the geological and geophysical crust–mantle background information of the Western Alps plays an important role. This chapter starts with a general overview of the Alpine system and especially the Western Alps. Followed by detailed crustal scale profiles focused around the CIFALPS profile and previous seismological studies.

2.1 Western Alpine system

The Alpine orogenic system, located in south-Europe, originated in the Cretaceous. The Alps are related to the subduction of the European Plate "eastward-southeastward" underneath the Adriatic Plate (Panza & Mueller, 1979). The Alps are divided into the Western Alps and Eastern Alps. The Western Alps are higher, but also shorter and more curved than the Eastern Alps.

The formation of the Western Alps is divided into 3 stages, the first stage was characterized by N to NNW thrusting during the late Cretaceous to 35 Ma followed by indentation of Adria and the Ivrea (= Adriatic) mantle wedge until the 25 Ma. The final stage of orogeny is associated together with the Apennines and leading to the oroclinal bending in the southern Western Alps (Schmid et al., 2017). The Ivrea mantle wedge, residing at shallow crustal depths and locally reaching the surface, plays an important role into the formation of the Western Alps. This mantle wedge is a positive gravimetric anomaly due to its high-density body (e.g. Closs & Labrouste, 1963; Scarponi et al., 2021). In Fig. 2.1, the tectonic map of the Western Alps is displayed together with the reference profile of the CIFALPS transect. The CIFALPS profile is bounded by the Argentera and Pelvoux transects which are shown in Fig. 2.2 and further described in section 2.2.

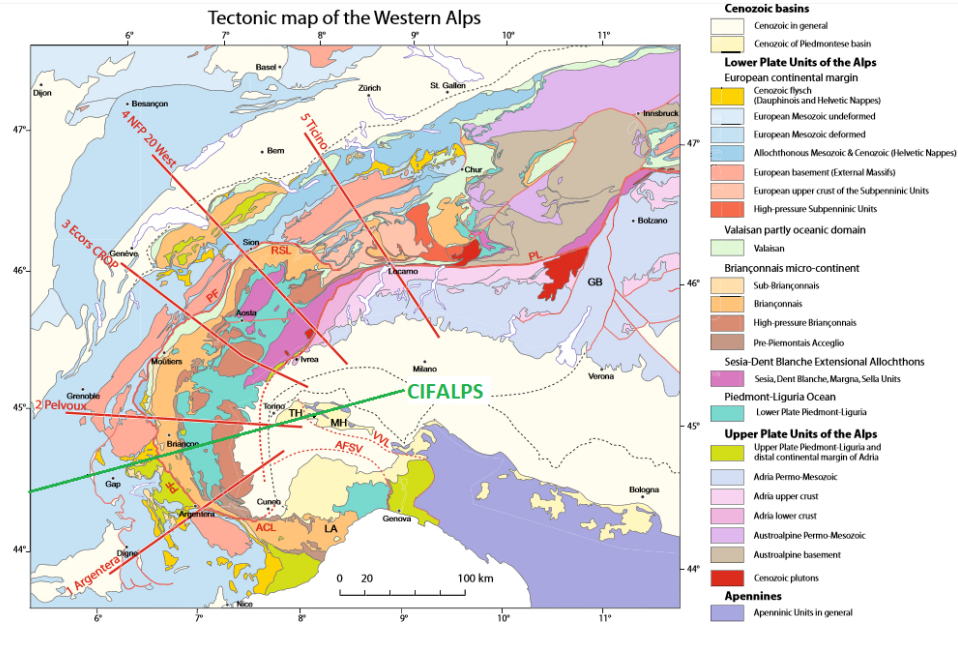


Figure 2.1 The tectonic map of the Western Alps modified after Schmid et al. (2017). The red and green lines are the reference profiles. The CIFALPS is shown by the green line and is surrounded by the Argentera and Pelvoux profiles (red lines).

2.2 Crustal-scale profiles surrounding the CIFALPS profile

Schmid et al. (2017) plotted the geological tectonic section with the P -wave velocity model of Diehl et al. (2009) and the Moho depth compiled by Spada et al. (2013) (Fig. 2.2). The Argentera and Pelvoux profiles follow the assumption of Schmid & Kissling (2000) that the European lower crust is decoupled from the upper crust and goes into subduction together with the underlying mantle below the Ivrea mantle wedge. The European Moho, 30 to 40 km, as defined by Spada et al. (2013) best corresponds to the velocity contours of 7.25 km s^{-1} in areas characterized by a subhorizontal or only weakly inclined Moho (Diehl et al., 2009). Whereas the strongly inclined boundary at the Ivrea mantle wedge, shallower depth $<30 \text{ km}$, follows the 7.0 km s^{-1} contour.

The Argentera profile, Fig. 2.2(a), shows that the European Moho coincided with a velocity gradient between 6.5 and 7.5 km s^{-1} (Diehl et al., 2009). There is a rather abrupt lateral change of velocities at a given depth across the boundary between external and internal Alps. This change coincides with the downward projection of the southern end of a very steeply NNE dipping late Alpine out-of-sequence thrust well documented in the Pelvoux section and known as the Penninic Front. The 6.5 km s^{-1} velocity contour goes steeply towards the NE part into the High-pressure

Briançonnais unit at a depth of <10 km. In addition, the 7.0 km s^{-1} velocity contour that runs parallel and near the Adria Moho rises towards the bottom of the HP Briançonnais (15 km). The contour is taken as the top of the Ivrea mantle wedge. The velocity contours, $5.5\text{-}7.0 \text{ km s}^{-1}$, within the Adria microplate Moho, lower crust and basement-sediment interface are E-dipping.

The Pelvoux profile, Fig. 2.2(b), shows a velocity gradient between 6.5 and 7.5 km s^{-1} within the European lithosphere (near the Moho). However, the 6.0 km s^{-1} contour rises to an unusually shallow depth of <10 km twice, a feature that is considered robust and points to the presence of high-velocity material at shallow depth. The linear extrapolation of the Penninic Front dip observed at the surface to depth is unconstrained by currently available geophysical data along this profile. An extrapolation of the Penninic Front to great depth such as to join the subduction channel at the base of the Ivrea mantle wedge is consistent with what was observed along the Argentera profile. The 6.5 and 7.0 km s^{-1} contours that follow the lower crust of the European lithosphere in the external Western Alps start to rise to shallower levels at an angle of around 45° after having crossed the Penninic Front, indicating that westward they enter the high-pressure Briançonnais units. The top of the Ivrea mantle wedge is constrained by the 7.0 km s^{-1} velocity contour. In addition, the inverse velocity gradient of the 7.5 km s^{-1} contour associated with a downbending of the same contour line points to the existence of a subduction channel below the Ivrea mantle wedge.

In addition, Zhao et al. (2015) shows that the CIFALPS profile has a similar subduction of the European continental lower crust below the Ivrea mantle wedge, based on P -wave receiver function analysis. In comparison, their model proposes a much shallower depth for the top of the Ivrea mantle wedge (at around 10 km) and a much wider (about 30 km) subduction channel below the Ivrea mantle wedge, features that are not compatible with the 3-D velocity model of Diehl et al. (2009) and the Moho depth as compiled by Spada et al. (2013). Section 2.3 summarizes the previous seismological studies on the CIFALPS profile.

2.3 Previous seismological studies on the CIFALPS profile

Zhao et al. (2015) present the first seismic evidence for the subduction of the European crust in the Adriatic mantle beneath the Dora Maira massif. To image the crustal structures along the profile, they used the P receiver function (RF) technique that enhances P to S (Ps) converted waves using teleseismic earthquakes (Langston, 1979). The receiver function records were stacked and migrated from time to depth using the common conversion point method to produce a depth section of Ps converted phases along the profile (Fig. 2.3). In Fig. 2.3(b) the European Moho (black line) is continuously traced as a strong-amplitude positive-polarity converted phase that dips gently to the east-northeast from 35 km at the western end of the profile,

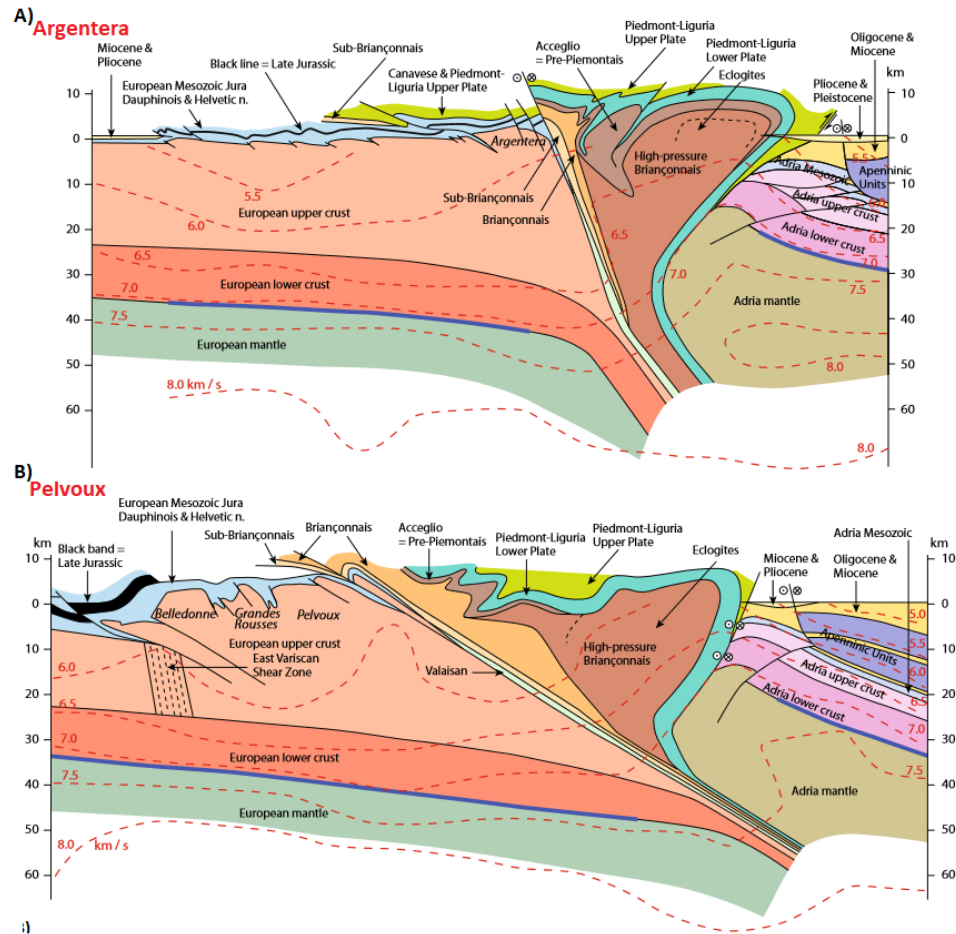


Figure 2.2 The Argentera (a) and Pelvoux (b) crustal-scale profiles by Schmid et al. (2017). The geological profiles are superimposed with the P-wave velocity model of Diehl et al. (2009), red dashed lines, and the Moho, blue line, which is a combination from the results by Wagner et al. (2012) and Spada et al. (2013).

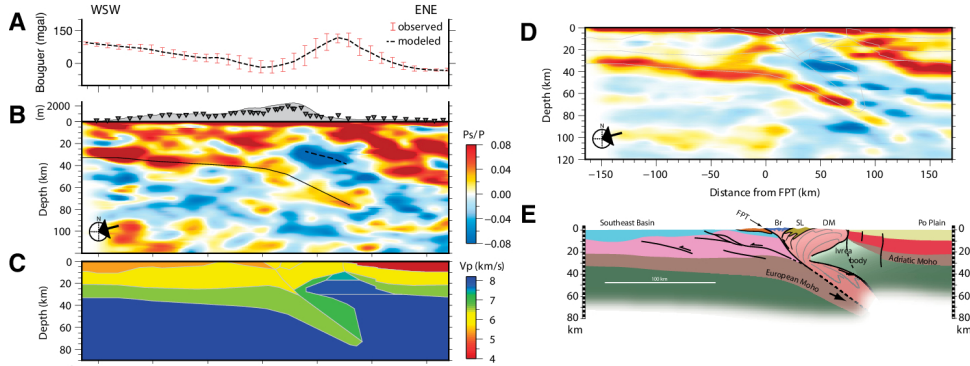


Figure 2.3 *A: The observed and modeled Bouguer gravity anomaly. B: The CCP depth-migrated section from teleseismic events with the red and blue colors representing respectively the positive and negative PS phases. C: The preferred two-dimensional velocity model and the corresponding computed synthetic CCP depth section in D. E: The proposed crustal-scale geological cross section. Br-Briançonnais; DM-Dora Maira; FPT-Frontal Penninic thrust; SL-schistes lustrés (Zhao et al., 2015).*

to 40 km beneath the Frontal Penninic thrust (FPT in Fig. 2.3e). The European Moho reaches a maximum depth of 75 km beneath the Dora Maira massif (DM in Fig. 2.3e) and the westernmost Po Plain.

A thick spot of Ps conversions with negative polarity (dashed line in Fig. 2.3b) and strong amplitudes is present between 20 km and 60 km depth beneath the Dora Maira massif and the westernmost Po Plain. This is located above the weak positive conversion of the European Moho and below the strong shallow positive signals that coincide with the Bouguer gravity anomaly high (red curve in Fig. 2.3a) associated with the so-called Ivrea body. The receiver function common-conversion point, CCP, depth-migrated section shows a thick set of Ps conversions of negative polarity that correspond to downward velocity decreases between the Ivrea body mantle slice on top and the European lower crust underneath thus providing evidence for an inverted Moho structure.

Fig. 2.3(e) shows the crustal-scale cross section of the southwestern Alps that they proposed with the assumption that a broad east-west elongated body of hydrated mantle akin to the Ivrea body indents a thick wedge of high-pressure to ultrahigh-pressure (HP-UHP) metamorphosed European crust of lower velocity that crops out in the Dora Maira massif.

Angular harmonics of P Receiver Functions

In the study of Piana Agostinetti et al. (2017) the RF data-set is migrated at depth and decomposed into azimuthal harmonics. The first, $k=0$, and the second, $k=1$,

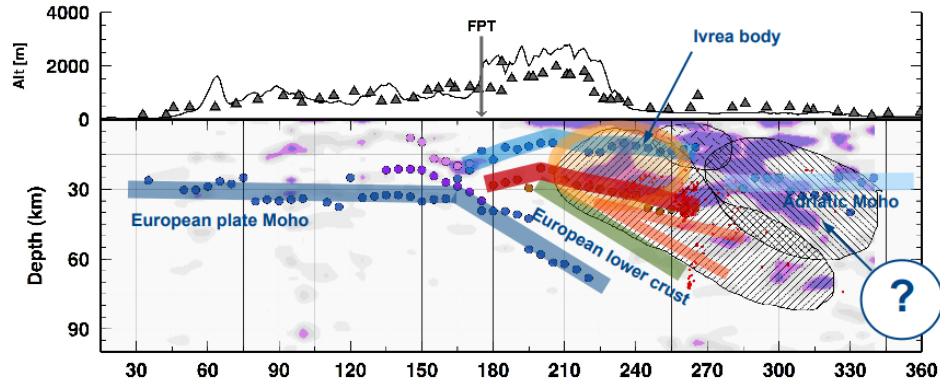


Figure 2.4 The interpretations by Piana Agostinetti et al. (2017) of the main observations from the azimuthal harmonics. All relevant phases from the harmonics are indicated as colored circles and patterns, plotted on the map of the relevant energy on the $k=1$ harmonics. The red line marks the inverted Moho (decrease of velocity) or bottom of the Ivrea Body Topography. In addition, the negative velocity jump with hydrated mantle materials is indicated by the pink-orange lines. The station elevations are shown on top. FPT indicates the position where the profile crosses the Frontal Penninic Thrust. The questions mark, ?, is for the interpretation which is still ongoing (Piana Agostinetti et al., 2017).

harmonics allows to separate the isotropic contribution, due to the change of the isotropic properties of the sampled materials (recorded on the $k=0$ harmonics), from the anisotropic contribution, where the energy is related to the propagation of the P -wave through anisotropic materials (recorded on the $k=1$ harmonics). The first harmonics confirms the subduction of the European Moho and the second harmonics indicate the presence of anisotropic materials at depth 10-30 km that are interpreted as the Ivrea Body (Fig. 2.4).

Seismic interferometry: theory

Claerbout (1968) shows that one side of the autocorrelation of the seismogram due to an impulsive source at depth is the seismogram due to an impulsive source on the surface. This is essentially 1D reflected-wave interferometry. One of the main applications of reflected-wave interferometry is retrieving the seismic reflection response from ambient noise and imaging of the reflectors in the subsurface without requiring knowledge of the subsurface medium parameters or of the positions of the actual sources. This chapter describes the 1D reflected-wave interferometry, the formulas are from Wapenaar et al. (2010).

3.1 1D reflected-wave interferometry

Seismic interferometry refers to the principle of generating new seismic responses of virtual sources by cross-correlating seismic observations at different receiver locations (Wapenaar et al., 2010). Fig. 3.1 is modified after Schuster (2009) and shows the basic principle of 1D reflected-wave interferometry. In Fig. 3.1(c) the virtual source (coloured in red) that is positioned at the first receiver generates the seismic response between the two receivers after cross-correlating, indicated by \otimes , the two seismic responses shown in Figs 3.1(a) and (b).

For a homogeneous lossless layer that is between a free surface and a homogeneous lossless half-space, the global transmission response $T(t)$ for an up-going wavefield emitted by an impulsive unit source in the lower half-space is shown in Fig. 3.2(a). The amplitudes, a are a function of the transmission coefficient of the interface, τ and the reflection coefficient of the interface, r : $a_0 = \tau$, $a_1 = -r\tau$, $a_2 = r^2\tau$ etc. The autocorrelation of the global transmission response, $T(t) * T(-t)$, and by defining the local transmission coefficient $\tau = \sqrt{1 - r^2}$ is at $t=0$, thus for zero time-lag:

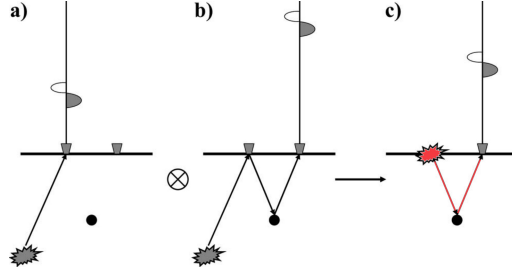


Figure 3.1 The basic principle of reflected seismic interferometry, modified after Schuster (2009). (a) seismic wave travels from a source at depth, where it is received by a geophone. (b) the wave is reflected downward at the surface and reflected upward again by the scatterer in the subsurface. The reflected wave is recorded by the second geophone. (c) By crosscorrelating the two traces, indicated by \otimes , the propagation along the common path is eliminated, leaving only the transmission from receiver 1 to the scatterer, and reflected to receiver 2.

$$\begin{aligned}
 & \delta(t) \sum_{i=0}^{i=\infty} a_i^2 \\
 &= \tau^2 \delta(t) \sum_{i=0}^{i=\infty} r^{2i} \\
 &= \tau^2 (1 - r^2)^{-1} \delta(t) = \delta(t)
 \end{aligned} \tag{3.1}$$

The autocorrelation for $\Delta t = 2\Delta z/c$, where Δz is the thickness of the first layer and c its propagation velocity, becomes:

$$\begin{aligned}
 & \delta(t - \Delta t) \sum_{i=0}^{i=\infty} a_{i+1} a_i \\
 &= -r\tau^2 \delta(t - \Delta t) \sum_{i=0}^{i=\infty} r^{2i} \\
 &= -r\delta(t - \Delta t)
 \end{aligned} \tag{3.2}$$

The arrivals of the autocorrelation of the global transmission response in Fig. 3.2(b) are gathered in the causal part, $-R(t)$, and acausal part, $-R(-t)$. The causal part represents the global reflection response $R(t)$ of a down-going plane wave from the free surface, hence the minus sign. The autocorrelation can be summed up to:

$$T(t) * T(-t) = \delta(t) - R(t) - R(-t) \tag{3.3}$$

Rearranging the equation to $R(t) + R(-t) = \delta(t) - T(t) * T(-t)$, shows that

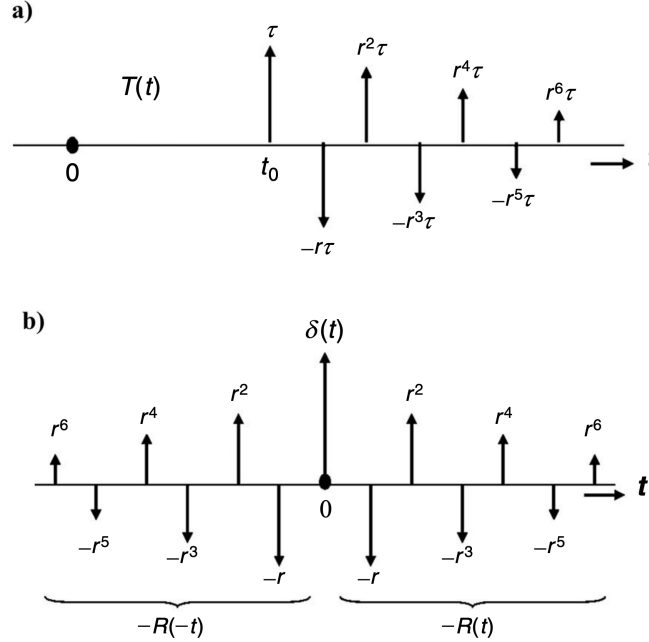


Figure 3.2 From Wapenaar et al. (2010): (a) The transmission response $T(t)$ observed at the free surface. (b) Sketch of the autocorrelation $T(t) \otimes T(-t)$ illustrating the associated reflection response, the causal part, $-R(t)$, and acausal part, $-R(-t)$.

the global reflection response is attainable from the autocorrelation of the global transmission response.

To describe the relation of the up and down-going wave-fields, the principle of power conservation is used (Wapenaar et al., 2010). It is easiest to describe the power flux in the frequency domain. The down-going wavefield is $\hat{D} = 1 - \hat{R}$ and the up-going wavefield is $\hat{U} = \hat{R}$. The net power flux below the free surface is given by:

$$\hat{D}\hat{D}^* - \hat{U}\hat{U}^* = (1 - \hat{R})(1 - \hat{R}^*) - \hat{R}\hat{R}^* = 1 - \hat{R} - \hat{R}^* \quad (3.4)$$

The total down-going transmitted wave-field, \tilde{T} , at the lowest interface includes all surface and internal multiples. In the lower half-space below the lowest interface there is no up-going wave-field, because it is assumed to be homogeneous, therefore the net down-going power flux in the lowest half-space is:

$$\tilde{D}^* \tilde{D} - \tilde{U}^* \tilde{U} = \tilde{D}^* \tilde{D} = \tilde{T}^* \tilde{T} \quad (3.5)$$

Combining equations 3.4 and 3.5 by taking into consideration the principle of

power conservation becomes:

$$\tilde{T}^* \tilde{T} = 1 - \tilde{R} - \tilde{R}^* \quad (3.6)$$

The inverse Fourier transform of this equation becomes equation 3.3. Rearranging the equation gives $R(t) + R(-t) = \delta(t) - T(-t) * T(t)$ in the time-domain and equalizes to the rearranged equation 3.3. This shows that the theory holds for any arbitrary horizontally layered media and states that the reflection response can be obtained from the autocorrelation of the transmission response of an impulsive source in the subsurface, independent of its depth. By taking into consideration a noise signal, $N(t)$, emitted by the source in the lower half-space. The up-going wavefield at the surface is $u(t) = T(t) * N(t)$ and the rearranged equation 3.3 becomes for noise signals:

$$\{R(t) + R(-t)\} * S_N(t) = S_N(t) - \langle u(t) * u(-t) \rangle \quad (3.7)$$

, where $S_N(t)$ is the autocorrelation of the noise. This equation shows that the reflection response of a transient source at the surface can be obtained from the autocorrelation of passive noise measurements. This 1-D approach can be extended to 2-D and 3-D. Seismic interferometry is also often called Green's function retrieval. By decreasing the distance between the two receivers, the limit of the cross-correlation can be obtained resulting in a Green's function version with zero-offset.

The Moho reflectivity of the subduction beneath the Southwestern Alps from ambient seismic noise autocorrelations

Summary The Western Alps shows a complex crustal organization due to the subduction of the European Plate beneath the Adriatic Plate and exhumation of the mantle wedge. The lithospheric structure of the Western Alps, that may hold significance for understanding orogenic processes and evolution, has been the subject of many geophysical studies, but the Moho profile remains unclear, and this has led to controversies about the depth and extent of the European Plate beneath the Adriatic plate. With the goal of retrieving detailed information on crustal constitution, we use autocorrelation of seismic ambient noise as a tool to map the body wave reflectivity structure at the subduction zone under the southwestern Alps. We use data recorded by the China–Italy–France Alps (CIFALPS) seismic transect, that includes 45 stations located approximately 5–10 km apart along a profile crossing the Alpine continental subduction in the Western Alps. We analyse the data set in four different frequency bands between 0.09 and 2 Hz. We automatically pick the arrival time of the Moho reflection in the second derivative of the envelope of the autocorrelation stack using prior Moho information. The 0.5–1 Hz frequency band mostly gives the best result due to the clear changes in reflectivity along the waveforms of the autocorrelation stacks after the picked arrival times of the Moho reflections. We find spatial coherence between 18 and 23 km depth in the western portion of the profile, indicating relatively homogeneous crustal rocks, and highly reflective structure under the central mountain range, due to the existence of a highly faulted zone. The very thin crust and the underlying mantle wedge known

This chapter is published as: Ashruf, T.N. & Morelli, A., 2022. The Moho reflectivity of the subduction beneath the Southwestern Alps from ambient seismic noise autocorrelations, *Geophysical Journal International*, **230**(1), 298–316, doi:10.1093/gji/ggac079

as the Ivrea body show instead high transparency to seismic waves and absence of reflections. The subduction profile of the European Plate shows a steep trend as compared to previous studies. We discuss autocorrelation stacks and Moho depths obtained from the arrival times of the picked reflectivity change in comparison with previous studies to validate the different reflection structures. Stacked ambient noise autocorrelations reliably image varied crustal properties and reflectivity structures in the highly heterogeneous region of the southwestern Alps.

Keywords: Europe, Body waves, Seismic interferometry, Seismic noise, Crustal structure

4.1 Introduction

4.1.1 Tectonic background

The complex geological structure involved in the Alpine orogeny is the result of the European and Adriatic plates converging motion in a process marked by subduction, accretion and transformation (e.g. Handy et al., 2010; van Hinsbergen et al., 2020). This region has been the subject of many geological and geophysical studies focused on understanding its geodynamic evolution, leading to controversial results regarding, for example the amount of crustal subduction under the Alps (e.g. Grellet et al., 1993; Thouvenot et al., 2007). In fact, the subduction of the European Plate underneath the Adriatic Plate during the Cretaceous to Palaeogene (e.g. Handy et al., 2010) has led to complex variation in Moho depths along the Western Alps, especially in the southwestern Alps. This specific area has been probed by several seismological studies. The controlled source seismological study by Grellet et al. (1993) mapped the Moho depth between 47 and 50 km, whereas using the same approach Thouvenot et al. (2007) measured a deeper Moho, down to 55 km, providing evidence of the crustal root being much thicker. Nicole et al. (2007) and Diehl et al. (2009) have used local earthquake data to image the 3-D velocity structure. The latter study was able to gather detailed information of the Ivrea body and the European crust underneath the Adriatic crust down to a depth of 45 km. In addition, the southwestern Alps have been the subject of various studies using teleseismic earthquake records (e.g. Lombardi et al., 2008; Zhao et al., 2015; Beller et al., 2018). In the receiver function study by Lombardi et al. (2008) the Moho reached depths of about 55 km beneath some stations, however only sparse information was available for the southwestern Alps due to the few stations in the area. In 2012 the China–Italy–France Alps seismic survey (CIFALPS) deployed a passive seismic profile cutting completely through the southwestern Alps (see Map in Fig. 4.1) to improve the constraints on the lithospheric structure, with emphasis on the Moho geometry. Zhao et al. (2015) used the teleseismic earthquake records of the CIFALPS data set to create P receiver functions and claimed the first seismic evidence of continental subduction down to 75 km depth beneath the southwestern

Alps. Beller et al. (2018) used the same data set and applied a teleseismic full-waveform inversion method that resulted in Moho depths down to 80–90 km for the v_S model. Furthermore, Lu et al. (2018) and Kästle et al. (2018) have created shear wave velocity models by extracting surface wave information from cross-correlation of ambient seismic noise. Lu et al. (2018) imaged shallower Moho depths than Zhao et al. (2015) beneath the Southeast Basin that is situated at the western end of the CIFALPS profile (Fig. 4.1). In addition, Lu et al. (2018) obtained a posteriori probability densities of interfaces by Bayesian inversion that resulted in a very low probability for the Moho discontinuity at 45–90 km depth beneath the Ivrea body. The results by Kästle et al. (2018) imaged also shallower Moho depths beneath the Southeast Basin and reached a maximum depth of 60 km for continental subduction as opposed to the deeper subductions by previous teleseismic studies. The results of these studies give clear evidence of the uncertainties on the crust–mantle transition zone in the southwestern region of the Alpine belt.

4.1.2 Seismic interferometry

Seismic interferometry is a method to obtain the Green’s function between two seismic receivers by cross-correlating the recorded seismic wavefield. The impulse response or Green’s function is thus obtained at one receiver as produced by a virtual source at the position of the other receiver (e.g. Roux et al., 2005). In recent years, passive seismic interferometry has become a standard tool that uses ambient seismic noise for investigating the Earth structure between two receivers (e.g. Nakata et al., 2019) by obtaining surface wave dispersion. However, imaging sharp discontinuities such as the Moho are difficult because the surface wave velocities reconstructed from ambient noise cross-correlations are not explicitly sensitive to the depth of layer boundaries. When the distance between the two receivers decreases to zero, the cross-correlation becomes the autocorrelation of signal recorded at a single station. The autocorrelation is a zero-offset reflection response by assuming a collocated source and receiver. Claerbout (1968) has shown that the autocorrelation for a vertically incident plane acoustic wave transmitted through a layered structure with a free surface provides sufficient information to recover the reflection response of the medium, including free surface multiples. This can also be applied to ambient noise. In this case, the surface wave component loses its dominance and the body wave interaction with the structure beneath the station increases in importance. Wapenaar et al. (2008) have shown that seismic interferometry works for suitable noise conditions without any earthquake or man-made sources. Therefore, ambient noise seismic data becomes a powerful tool to study sharp discontinuities.

4.1.3 Applications of seismic ambient noise autocorrelation

In the last decade, autocorrelation of ambient seismic noise has often been used to image the Earth structure beneath seismic stations. Tibuleac & von Seggern (2012) created noise autocorrelations on three components of seismic stations in Nevada to extract Moho-reflected body wave phases in the 0.5–1.0 Hz frequency band. Oren & Nowack (2016) found similar results as Tibuleac & von Seggern (2012) by creating noise autocorrelations using different processing techniques in Nevada and the central U.S.A. using different cut-off frequencies between the 0.2 and 0.75 Hz range. Gorbatov et al. (2013) computed noise autocorrelations in the 2.0–4.0 Hz range on the vertical component of stations in Australia to create Moho depth maps. Similar studies have been performed in Australia by Kennett et al. (2015) in the 2.0–4.0 frequency band, and by Kennett (2015) with different cut-off frequencies in the 0.5–4.0 Hz range. Taylor et al. (2016) imaged the crustal structure of the North Anatolian Fault zone in Turkey by bandpass filtering the autocorrelations in the 0.2–0.4 Hz frequency band. Saygin et al. (2017) mapped the *P*-wave reflection response of the Jakarta Basin, Indonesia in the 2.0–4.0 Hz frequency band. The Ebro Basin in Spain was mapped by Romero & Schimmel (2018) using ambient noise autocorrelations, where the data were significantly filtered in broader frequency ranges with the lower and upper corner frequencies ranging between 3.0–4.0 Hz and 9.0–18.0 Hz, respectively. In Central and Eastern Europe, Becker & Knapmeyer-Endrun (2018) and Becker & Knapmeyer-Endrun (2019a) extracted the crustal thickness from noise autocorrelations in the 1.0–2.0 Hz and 2.0–4.0 Hz frequency bands for respectively the vertical and horizontal component data. The detection of the Moho reflectivity depends on the character of the discontinuity. The Moho coincides with a prominent body wave reflection when the discontinuity is sharp (Tibuleac & von Seggern, 2012; Gorbatov et al., 2013; Phạm & Tkalčić, 2017). However, when the discontinuity is marked by a gradational transition between the crustal and mantle wave speed, the detection of the Moho becomes less clear and additional independent information is needed (Kennett, 2015; Kennett et al., 2015; Becker & Knapmeyer-Endrun, 2018, 2019a). Kennett (2015) has shown that in areas with a gradational Moho discontinuity, the base of the crustal reflectivity fits well with the Moho. In addition, Becker & Knapmeyer-Endrun (2018) have shown that the base of crustal reflectivity coincides with the local maximum of the second derivative of the envelope of the autocorrelation, thus providing a criterion useful for automatic detection of the interface. From the shear wave velocity models by Lyu et al. (2017) it is clear that the Western Alps are characterized by a gradational Moho.

4.1.4 Research aim and overview

In this study, we estimate zero-offset reflection responses using ambient noise autocorrelations with the aim of imaging the subduction of the European Plate un-

derneath the Adriatic micro plate in the southwestern Alps. We use prior Moho information by Zhao et al. (2015) to follow the principle proposed by Becker & Knapmeyer-Endrun (2018) for selecting the reflection coinciding to the gradational Moho. After a detailed description of our processing workflow, we present the results of the automatically and manually picked arrival times of Moho reflections for different frequency bands. Further, we discuss the results and geological features detected along the cross-section compared to the geological features from previous studies.

4.2 Data and Method

In this section, we start with the data set used in this study. Afterwards, we describe the range of frequency that has been chosen for imaging body wave reflections from ambient noise autocorrelations. In addition, we outline the processing steps for creating autocorrelation stacks for each station. At last, we show the Moho signature that is picked from the second derivative envelope of the autocorrelation stacks. This method is based on the study by Becker & Knapmeyer-Endrun (2018).

4.2.1 Data

We use the ambient seismic noise data recorded by the broad-band CIFALPS (China–Italy–France Alps) seismic survey (Zhao et al., 2016). The 46 seismic stations of the network were set up through the southwestern Alps with an interstation distance of 5–10 km and operated for 14 months between 2012 and 2013 (see station map in Fig. 4.1). Station information is given in table A.1 of Appendix A. Station CT37 is discarded due to instrumental problems for the majority of the days and it is marked by a red filled star in Fig. 4.1. The seismic waveform data of the vertical channels (HHZ) were downloaded from the Résif Seismological data portal (Zhao et al., 2016) and have a sample rate of 100 Hz. In this work, we only use the vertical components since our focus lies on the reflected P -wave energy that is expected to travel with vertical incidence. We use the term reflectivity for the reflected P -wave energy travelling at vertical incidence.

The seismic data of the CIFALPS (Zhao et al., 2016) experiment is freely available at the Résif Seismological data portal (<http://doi.org/10.17616/R37Q06>). The seismic data are also archived at the data centre of the Seismic Array Laboratory, Institute of Geology and Geophysics, Chinese Academy of Sciences, and at the data centre of the French Seismologic and Geodetic Network.

4.2.2 Ambient noise frequency ranges

Although more than 50 yr ago Claerbout (1968) has shown that body waves extracted from autocorrelations provide the reflection response of the medium below

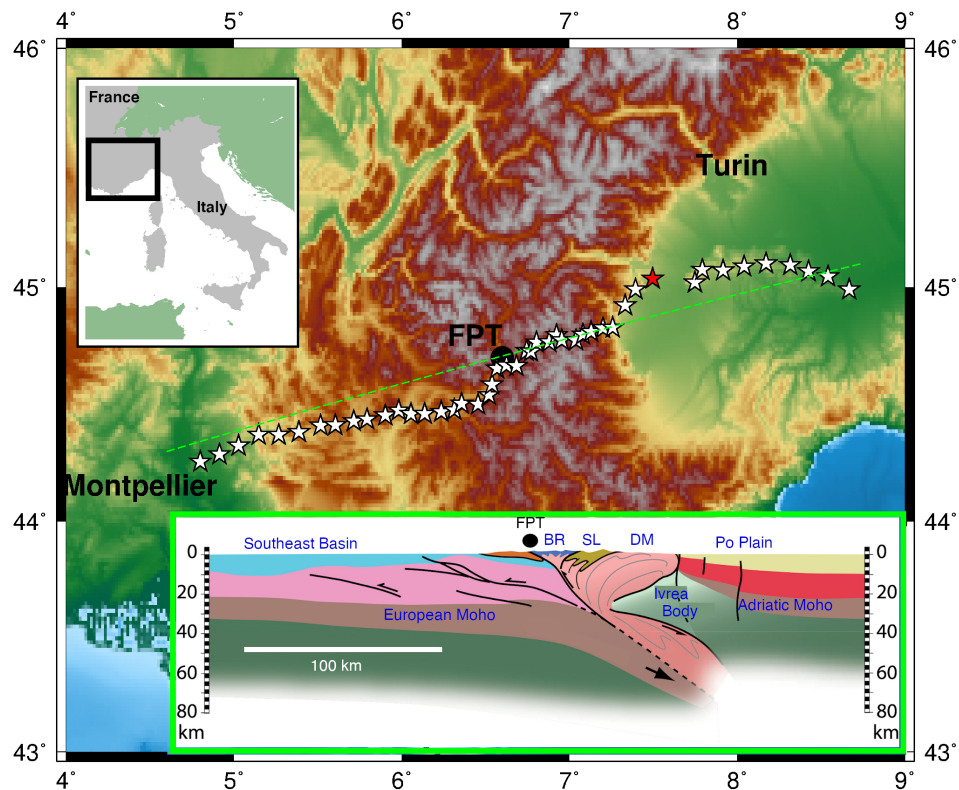


Figure 4.1 Map of CIFALPS stations, marked by white stars, plotted on topographic elevation. The red star is the discarded station CT37. The black circle marks the Frontal Penninic thrust (FPT) through which the dotted green line goes. This dotted line is the reference profile used for projections to compare the final results to the receiver function study by Zhao *et al.* (2015). The crustal-scale geological interpreted cross section by Zhao *et al.* (2015) along the reference profile is shown in the bottom right-hand figure. BR, Briançonnais; SL, Schistes Lustrés; DM, Dora Maira.

the station, only in the last decade this method has been used in passive seismological studies (e.g. Tibuleac & von Seggern, 2012; Becker & Knapmeyer-Endrun, 2018). However, so far there is no standard procedure and frequency range to be used for extracting body wave reflections from autocorrelations. The study of the seismic ambient noise on the dominant type of waves in different frequency bands by Ruigrok et al. (2011) has shown that the vertical components are dominated by body waves with respect to surface waves in the 0.09–1 Hz frequency band. In addition, Asten (1976) has recorded the dominance of P waves microseism energy up to 2 Hz. Seismic ambient noise with frequency above 1 Hz is dependent on more nearby cultural sources and may strongly vary in amplitude based on the location of the station.

Fig. 4.2 shows the probability density function of the power spectral density (PSD) of the vertical channel, HHZ, of station CT14 (the figure is retrieved from: <http://dx.doi.org/10.15778/RESIF.YP2012>). The red rectangle highlights the period range of ambient noise that we use in this study to create autocorrelations taking into consideration the body wave dominance on the vertical component. The ocean-generated primary and secondary microseism peaks are marked by the white arrows and labelled respectively, PM and SM.

From further analysis, we leave out frequencies above 2 Hz, due to the complicated behaviour of the signal at these periods. In this study, the seismic ambient noise will be filtered between 0.09 and 2 Hz using different cut-off frequencies. The cut-off frequencies are based on including or excluding the primary and secondary microseism peak, 0.095 and 0.25 Hz, respectively.

4.2.3 Autocorrelation workflow

We process raw data using ObsPy (Krischer et al., 2015) and Matlab for respectively the first and second processing stages. In the first processing stage of the ambient seismic noise data, we start with subtracting the mean and trend before tapering the ends with a Hanning window width of 0.01. Afterwards, we decimate the data from $f_s = 100$ Hz to $f_s = 20$ Hz. Decimation has been performed to increase the processing speed, while taking into consideration that the highest cut-off frequency, 2 Hz, is well below the Nyquist frequency of 10 Hz. We finish the first processing stage by removing the instrument response over the following trapezoidal frequency range of $f_1 = 0.01$ Hz, $f_2 = 0.02$ Hz, $f_3 = 5$ Hz, $f_4 = 10$ Hz to obtain displacement (nm).

After such preparation, we further process the data with Matlab. Fig. 4.3 shows the sequential order of steps of the second processing stage to create autocorrelations for sample station CT05 on sample Julian day 201 of 2012. The second processing stage starts with filtering of the data by using a zero-phase two-pole Butterworth bandpass filter in the following passbands (frequencies in Hertz): [0.09–0.5], [0.1–0.5], [0.1–1], [0.3–1], [0.4–1], [0.5–1], [0.5–2] and [1–2]. Bandpass filtering can be

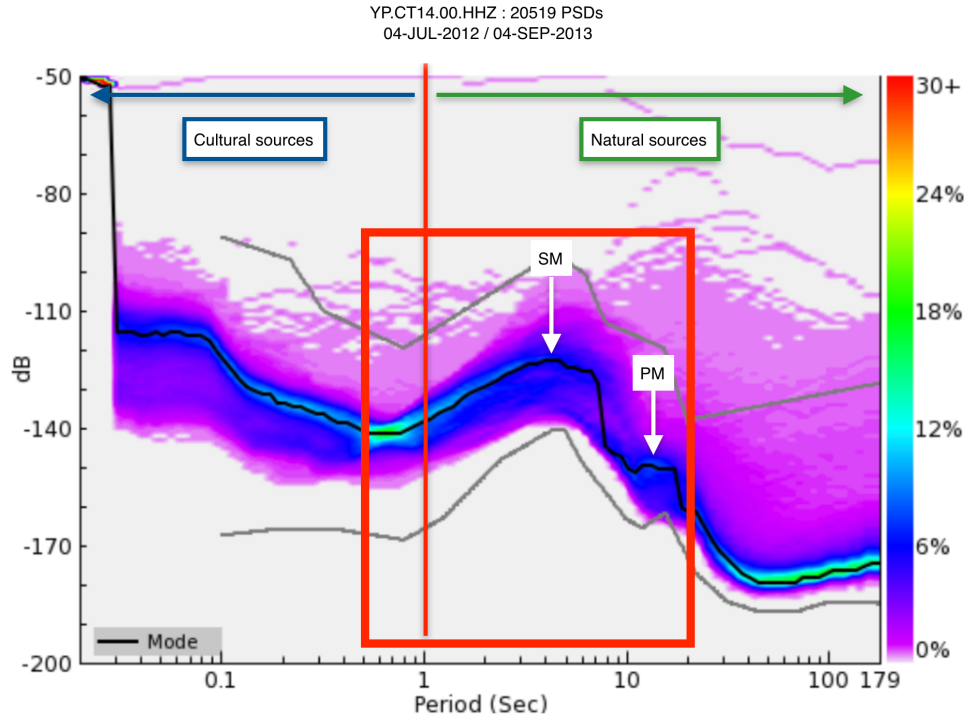


Figure 4.2 The probability density function of the power spectral densities (PSDs) of station CT14 (figure retrieved from: <http://dx.doi.org/10.15778/RESIF.YP2012>). The red rectangle marks the period range used in this study, that is dominated by body waves and include the primary (PM) and secondary (SM) microseism peak, 10.5 and 4 s, respectively.

applied either before (e.g. Romero & Schimmel, 2018) or after (e.g. Oren & Nowack, 2016) computation of the autocorrelations. Mroczek & Tilmann (2021) shows that when applying the bandpass filter after computation of the autocorrelations, more processing is needed to prevent the sidelobes of the zero-lag autocorrelation peak from masking the reflection response of the medium. We have applied the bandpass filter before computation of the autocorrelations. After applying the bandpass filter, we cut the time-series into 1-hr time intervals to autocorrelate, Fig. 4.3(c). In case of an earthquake, waveforms are dominated by high-amplitude wave packets. Bensen et al. (2007) showed that the effect of earthquakes and non-stationary sources close to the stations can effectively be removed by applying a time-domain, or temporal, normalization. Therefore, we also apply such sign-bit normalization that only retains information on zero-crossings in the time domain and obliterates amplitude information, Fig. 4.3(d). Afterwards, we autocorrelate 1-hr data slices, Fig. 4.3(e), and then linearly stack them for the complete data set.

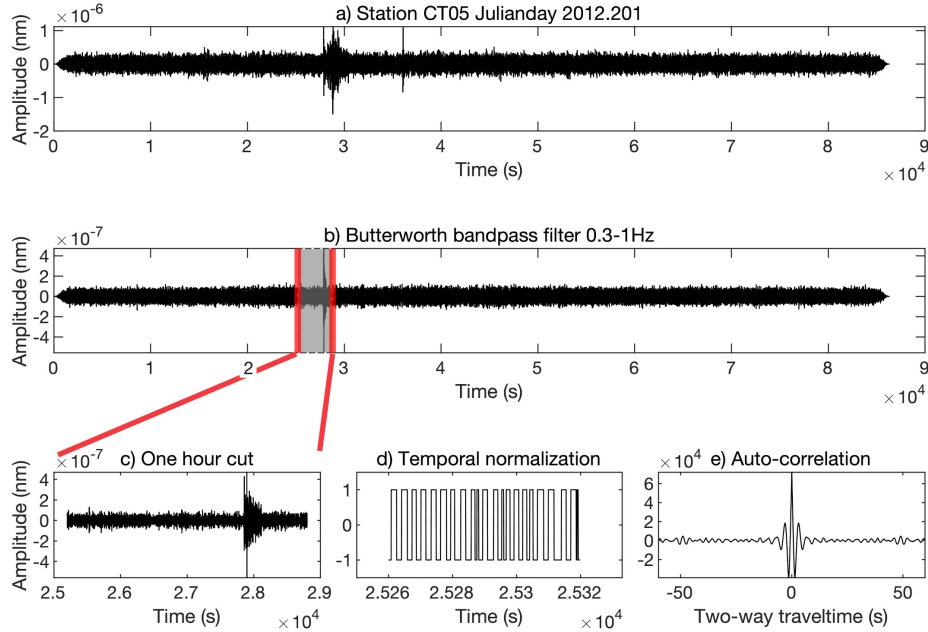


Figure 4.3 The processing steps performed to create autocorrelations for station CT05 on Julian day 201 of 2012. (a) After removing the mean, trend, tapering the end, decimating and removing the instrument response. (b) Data has been filtered between 0.3 and 1 Hz using a zero-phase Butterworth bandpass filter. (c) 1 hr cut of the day. (d) Temporal normalization and (e) hourly autocorrelation for the complete linear stack.

4.2.4 Moho reflectivity from autocorrelation stacks

The Moho discontinuity in autocorrelation stacks will not be a single prominent reflector for areas where the transition of the crust to mantle is gradational (e.g. Gorbatov et al., 2013; Kennett et al., 2015; Kennett, 2015). Kennett et al. (2015) and Kennett (2015) have shown that the base of the crustal reflectivity fits well with the Moho in areas where the Moho is gradational. Synthetic autocorrelation seismograms by Gorbatov et al. (2013) show that in such cases the transition does not originate a simple pulse, such as commonly seen in lower-frequency receiver function studies. Becker & Knapmeyer-Endrun (2018) have used this principle of picking the Moho depth as the base of the crustal reflector by developing an automated method to pick reflectivity changes. The picked reflectivity changes are chosen as the Moho depth if the pick matches a prominent reflectivity change along the waveform of the autocorrelation. Becker & Knapmeyer-Endrun (2018) automatically pick the reflectivity changes by extracting the local maxima inside an *a priori* time window of the 5-s weighted moving average of the second derivative autocorrelation envelope.

Their *a priori* time window is based on the uncertainty of the prior Moho information and the velocity model used. The local maxima coincides with large changes in the slope of the envelope and with changes in reflectivity.

We perform an automated pick of changes in reflectivity inside some *a priori* time window, based on Moho depth information from Zhao et al. (2015), of the second derivative envelope of the autocorrelation stack. The Moho depth is converted into two-way traveltime (TWT) by using the *P*-wave speed model, Fig. 4.4, of Zhao et al. (2015). Fig. 4.5 shows the method to pick the arrival times of the Moho reflections by automatically picking reflectivity changes from the second derivative of the envelope, applied to stations CT05 and CT07 respectively in the [0.3-1] and [0.5-1] Hz frequency band. We have not normalized the second derivative envelope, as opposed to Becker & Knapmeyer-Endrun (2018) since there will be no change in the waveform and the arrival time of the local maxima. The *a priori* time window is shown by the grey filled area, Fig. 4.5, and has a TWT width of 5 s, where the boundaries are set at 2.5 s TWT before and after the *a priori* Moho reflection time. The *a priori* time window is not based on the uncertainty of the prior Moho information and velocity model by Zhao et al. (2015) since these values are not available. The pink dashed-dotted line corresponds to the prior Moho information and the blue circle and blue dashed-dotted line to the local maximum picked inside the time window. To eliminate the noise of the second derivative of the envelope we use a 5-point moving average filter. We have not weighted the second derivative envelope with a five second moving average for assigning higher relevance to high amplitude parts (Becker & Knapmeyer-Endrun, 2018), since it is equally possible to identify the local maxima related to the reflectivity changes without weighting of the second derivative envelope (Becker & Knapmeyer-Endrun, 2019b). Furthermore, the length of the weighting time window has influence on which peaks are favoured because the filtered envelope's amplitude decay is controlled by the bandpass used (Helffrich, 2019; Becker & Knapmeyer-Endrun, 2019b).

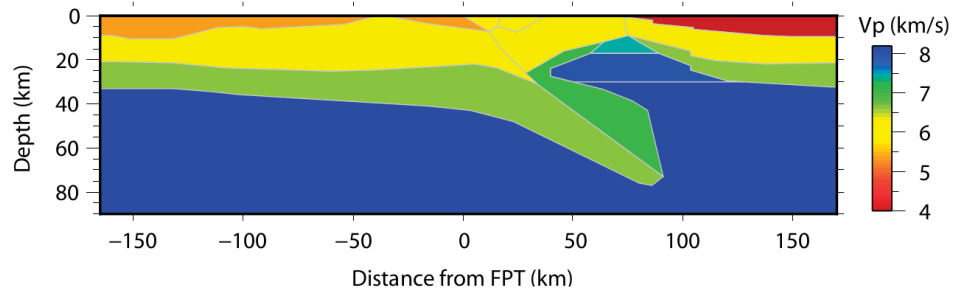


Figure 4.4 We have used the 2-D P-wave velocity model by Zhao et al. (2015). The colour scale is given on the right-hand side.

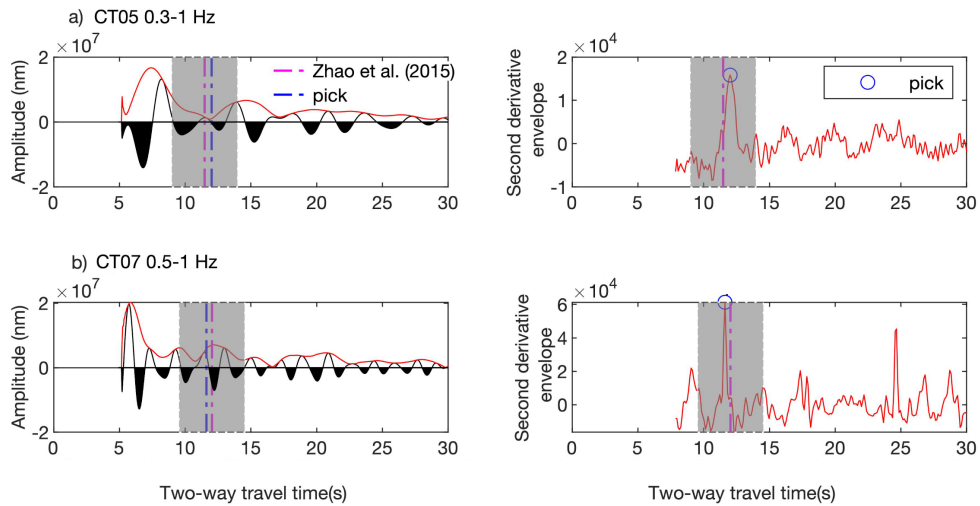


Figure 4.5 The stacked autocorrelations of station (a) CT05 and (b) CT07 are filtered respectively between the 0.3-1 Hz and 0.5-1 Hz frequency ranges. The stacks are shown on the left with the envelope in red, while the arrival times of the automatically picked reflectivity changes and previous Moho information by Zhao et al. (2015) are given by the blue and pink dashed-dotted lines, respectively. The plots on the right-hand side are the second derivative of the envelope, with the local maximum pick inside the a priori time window (grey filled area) shown by the blue circle (blue dashed-dotted line in the left-hand plot).

4.3 Results

We present autocorrelation stacks in the following frequency bands (Hz); [0.3–1], [0.4–1], [0.5–1] and [0.5–2]. First, we analyse the reflectivity changes along the waveforms of the autocorrelation stacks by using visual inspection. Afterwards, we analyse the temporal stability of the stacking process by plotting all daily autocorrelations for the complete data set, which are compared to the final stacks. In addition, we analyse convergence to the final average for the winter and summer months separately, by calculating the correlation coefficient between cumulative and final stacks. Furthermore, we show the automatically picked arrival times of the Moho reflections in different frequency bands. At last, we plot the final autocorrelation stacks of the stations alongside the whole CIFALPS profile, together with the picked arrival times of the Moho reflections, which are scaled to two-way traveltime (TWT) and migrated to depth. The autocorrelated stacks are plotted from 5 s TWT, to avoid the dominance of the large pulses at and after 0 s.

4.3.1 Autocorrelation stacks and temporal stability

The autocorrelation stacks of station CT22 are shown in Figs 4.6(b)–(i) for the following frequency bands (Hz), respectively; [0.09–0.5], [0.1–0.5], [0.1–1], [0.3–1], [0.4–1], [0.5–1], [0.5–2] and [1–2]. The autocorrelation stacks filtered with cut-off frequency less than or equal to 0.1 Hz (Figs 4.6b–d) show signals with long periods and no clear reflection changes. Therefore, it is difficult to detect crust–mantle reflections in these frequency bands and they have been discarded from further analysis. The autocorrelation stack filtered between 1 and 2 Hz (Fig. 4.6i) shows no clear reflectivity changes. The autocorrelation stacks of CT22 that are highlighted by the red box (Figs 4.6e–h) show clearly visible changes in reflectivity along the waveforms and are selected for further analysis. The points of changes in reflectivity are marked by the green dashed–dotted lines. The prior Moho information by Zhao et al. (2015) is marked by the pink dashed–dotted line. In addition, the prior information of the intracrustal discontinuity by Zhao et al. (2015) of the upper to lower crust has also been marked by the red dashed–dotted line to investigate the possibility of associating the changes in reflectivity to the intracrustal discontinuity.

The first changes in reflectivity are associated with a clear decrease in amplitude after the green dashed–dotted line, which lies around 11 s TWT for the 0.3–1 Hz autocorrelation stack and around 8.5 s TWT for the [0.4–1], [0.5–1] and [0.5–2] Hz frequency bands. The 11 s TWT reflectivity change has a difference of around 4 s TWT with the *a priori* intracrustal arrival time, whereas for the 8.5 s TWT reflectivity change there is a close match with the prior intracrustal information with a difference of around 1 s TWT. Furthermore, the first reflectivity change at around 11 s TWT in the 0.3–1 Hz autocorrelation stack, Fig. 4.6(e), lies closer to the *a priori* Moho arrival time with a difference of around 2 s TWT than to the *a*

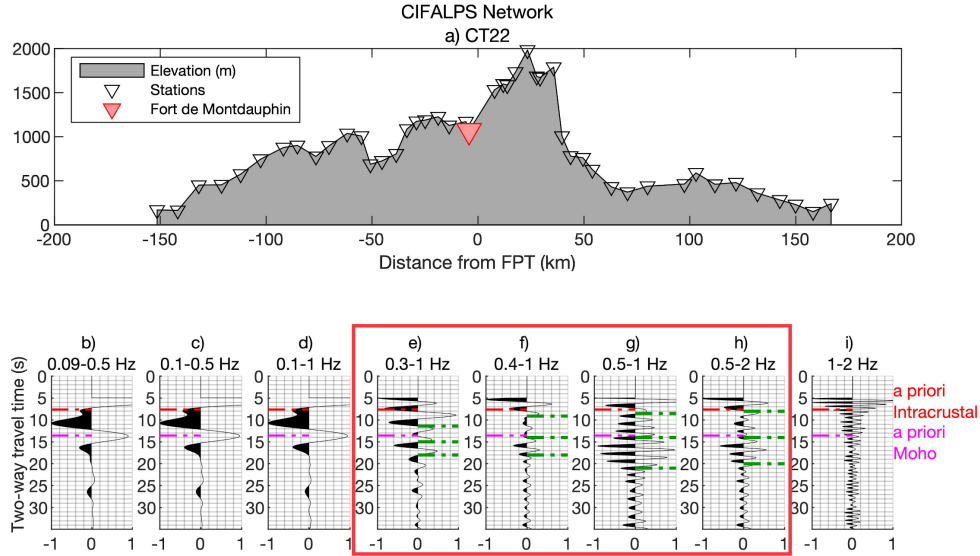


Figure 4.6 (a) Stations of the CIFALPS profile are plotted in elevation (m) from west to east. The position of Station CT22 is highlighted by the red upside down triangle. The autocorrelation stacks of station CT22 are shown in the following frequency bands (Hz); (b) [0.09–0.5], (c) [0.1–0.5], (d) [0.1–1], (e) [0.3–1], (f) [0.4–1], (g) [0.5–1], (h) [0.5–2] and (i) [1–2]. The autocorrelation stacks filtered with a cut-off frequency of ≤ 0.1 Hz show signals with long periods, leading to difficulties in detecting crustal reflections. No clear reflectivity change is visible in the 1–2 Hz frequency band. Therefore, the autocorrelation stacks in the red rectangle area are selected for further analysis. The previous intracrustal and Moho information by Zhao et al. (2015) are given by the red and pink dashed–dotted lines, respectively. The points where the reflection pattern changes along the waveforms of the stacks are marked by the green dashed–dotted line.

priori intracrustal arrival time. Therefore, it becomes difficult to relate this change in reflectivity to a specific discontinuity. The second changes in the reflection pattern along the autocorrelation stacks, at around 14 s TWT, are associated with a clear increase in amplitude and they closely match the prior Moho information by Zhao et al. (2015). There is a third change in reflectivity at later arrival times, at around 20 s TWT, that are marked by a decrease in amplitude. For the autocorrelation stacks filtered in the [0.3–1] and [0.4–1] Hz frequency bands, Figs 4.6(e) and (f), the third reflectivity changes are also associated with a change in frequency. The second change in reflectivity may be related to the base of the crust–mantle transition and the third change in the reflectivity pattern to the end of the crust–mantle reflection phase.

In Figs 4.7(a)–(d) we plot all daily autocorrelation stacks for the complete data set of station CT22 for, respectively [0.3–1], [0.4–1], [0.5–1] and [0.5–2] Hz frequency

bands, along with the sum of the daily stacks for each frequency band (labelled as ‘Final stack’ in the figure). This plot—that we produced and inspected for all stations—is important to assess the coherence of the daily averages that merge into the final sum. The daily autocorrelation stacks in the different frequency bands show overall good temporal stability. The [0.4–1], [0.5–1] and [0.5–2] Hz frequency bands have clear stable crustal reflectivity between 14 and 20 s TWT, outlined in green, which is less distinctive in the 0.3–1 Hz frequency band. In addition, these stable reflections along the daily stacks fall in between the second and third change of reflectivity that has been detected along the waveforms of the final autocorrelation stacks in Figs 4.6(f)–(h). The stable reflections between 14 and 20 s TWT may be less distinctive in the [0.3–1] Hz frequency band due to the longer wavelengths that are not able to detect the finer crustal boundaries. Furthermore, the [0.4–1] and [0.5–1] Hz frequency bands have at around 5–8 s TWT clear stable reflections that are absent in the [0.3–1] and [0.5–2] Hz frequency bands due to the waveforms between the daily autocorrelation stacks being less coherent.

We have further investigated the temporal stability by calculating the correlation coefficient between each daily stack and the final stack for the entire time interval of 5–35 s TWT. In addition, we also compute the correlation coefficient between the running accrued average of past daily stacks and the final total sum. Fig. 4.8(a) shows the time evolution of these correlation coefficients for station CT22 filtered in the 0.5–1 Hz frequency band and Fig. 4.8(b) shows all daily stacks and the final stack. The correlation coefficient between each single day and the final stack is shown by the blue line in Fig. 4.8(a) that displays quite strong oscillating variations along the time interval, denoting the cyclic presence of perturbed (with low correlation) and better days (with high correlation). However, after stacking only 1 month of data the correlation coefficient reaches a stable value, as seen looking at the red line in Fig. 4.8(a) that shows a monotonically increasing trend with time before reaching a clear convergence. The same amount of stacked autocorrelations is needed for the [0.4–1] and [0.5–2] Hz frequency bands in order to reach a stable correlation coefficient. This is not the case for the autocorrelation stacks filtered in the [0.3–1] Hz frequency band, which shows less distinctive stable reflections in Fig. 4.7(a), the correlation coefficient reaches stability only after 4.5 months of data.

We also calculate the stability and convergence separately for the summer and winter months (Figs 4.8c and d), to investigate the seasonal effects on the reflections of the ambient noise autocorrelations. The daily stacks and the final stack of the summer days are shown in Fig. 4.8(e) and the equivalent is shown for the winter days in Fig. 4.8(f). The correlation coefficients in Fig. 4.8(c) are calculated as before between one daily stack of the summer and the final stack of the daily summer stacks, Fig. 4.8(e). The same is done for the winter months and are shown in Figs 4.8(d) and (f). The winter stack reaches a stable correlation coefficient value after just using less than half of the days of December, whereas the stack of the summer days reaches

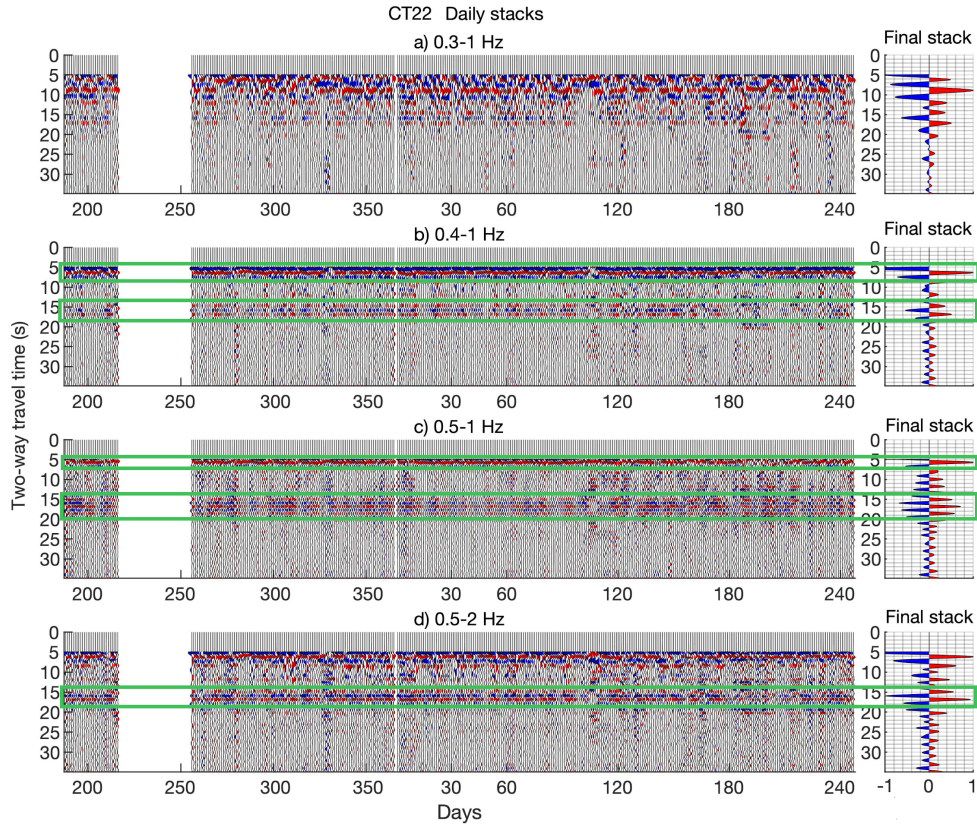


Figure 4.7 The daily autocorrelation stacks of station CT22 are filtered in the (a) [0.3–1], (b) [0.4–1], (c) [0.5–1] and (d) [0.5–2] Hz frequency bands. The final stack of the daily stacks in each frequency band are shown in the graph on the right-hand side. The areas outlined by the green rectangles, between ~ 14 s TWT and ~ 20 s TWT, are the distinctive stable reflectivities that may be due to the crust–mantle boundary. In addition, the stable reflectivities detected at earlier arrival times in the [0.4–1] and [0.5–1] Hz frequency bands may be due to the intracrustal discontinuity. The positive and negative amplitude lobes are filled with the red and blue colour, respectively.

a strong correlation after one month which then suddenly decreases and reaches stability at a lower value. This decrease in stability, Fig. 4.8(c), can also be explained by the variance of the daily autocorrelation stacks. We calculate the amplitude variance of each correlogram for the entire time interval of 5–35 s TWT. Schimmel et al. (2021) have evaluated signal stability—used to compute autocorrelations—in connection to variability of noise root-mean squared amplitude, but we evaluate instead the variance of entire correlograms as a measure of complexity. Such variance clearly increases in the summer months, see Fig. 4.9. This increase may be associated with a decrease of natural sources during the summer months, such as the absence of winter storms, that may reasonably generate a more diffused noise field, that yield clearer autocorrelations. In addition, the mean variance of the summer months, Fig. 4.9(c), is higher than both the mean of the complete data set and the mean of only the winter months.

We marked the prior Moho and intracrustal arrival time along the waveform of the final summer and winter stack, Figs 4.8(e) and (f), together with the manually picked changes in reflectivity of Fig. 4.6(g). The striking outcome is that the manually picked changes in reflectivity are also associated with clearly visible reflectivity changes in the final winter stack, which is not the case for the final summer stack. The daily summer stacks show strong stable reflections, but they are hard to associate to a clear change in reflectivity along the final summer stack. Furthermore, the correlation coefficient between the final winter stack, Fig. 4.8(f), and the complete final stack, Fig. 4.8(b), has a value of 0.99 compared to the correlation coefficient of 0.93 between the final summer stack, Fig. 4.8(e), and the complete final stack. The final winter stack has a higher correlation with the complete final stack that may be due to the atmospherical winter storms that favour reaching stability faster.

4.3.2 Picked arrival times of the Moho reflectivity

For stations CT22 and CT15, Figs 4.10 and 4.11, we show the autocorrelation stacks along with the automatically picked changes in reflectivity, blue dashed–dotted line in the left plot, based on the prior Moho information by Zhao et al. (2015), pink dashed–dotted line. To investigate the possibility of associating the intracrustal discontinuity to the automatically picked reflectivity changes, we have also plotted the prior intracrustal information by Zhao et al. (2015) as a red dashed–dotted line. For each autocorrelation stack, the second derivative envelope is shown in the right-hand plot with the automatically picked reflectivity change (blue circle), which is based on the method by Becker & Knapmeyer-Endrun (2018). For each station we show the results in the following frequency bands (Hz): (a) [0.3–1], (b) [0.4–1], (c) [0.5–1] and (d) [0.5–2]. In the next paragraph, we analyse for each station separately the automatically picked changes in reflectivity that may be associated with the Moho reflectivity or the intracrustal discontinuity.

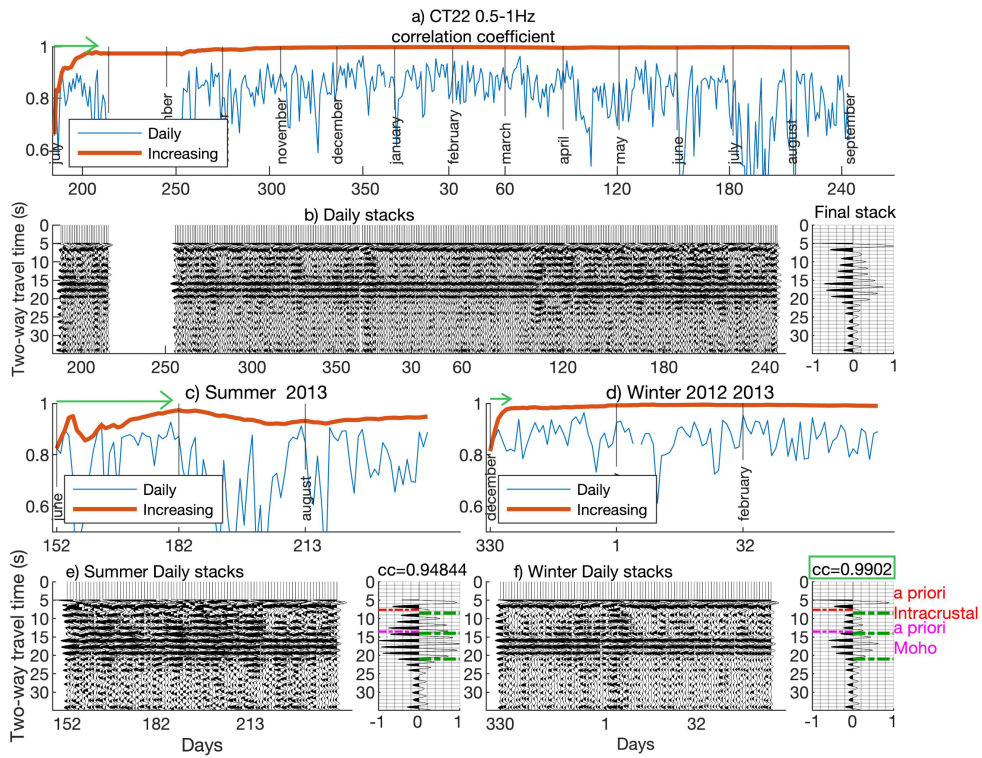


Figure 4.8 (a) The correlation coefficient for station CT22 filtered in the 0.5–1 Hz frequency band between the daily autocorrelation stacks and final stack shown in (b). The correlation coefficient between one day and the final stack is shown by the blue line. The red line is the correlation coefficient between stacked number of daily autocorrelations, that is increasing along with the operation time, and the final stack. The same procedure has been done separately for the summer months (c) and winter months (d). The daily stacks and final stack for the summer and winter are shown respectively in (e) and (f). The correlation coefficient between the final winter stack and the complete final stack shown in (b), given by the value cc , is marked by a green box due to the higher correlation as compared to the correlation coefficient value between the final summer stack and complete final stack. In addition, the prior Moho and intracrustal arrival time derived from Zhao et al. (2015) are plotted as a pink and red dashed-dotted line, respectively. The changes in reflectivity detected along the waveform of the final stack, see Fig. 4.6(g), are marked by the green dashed-dotted lines.

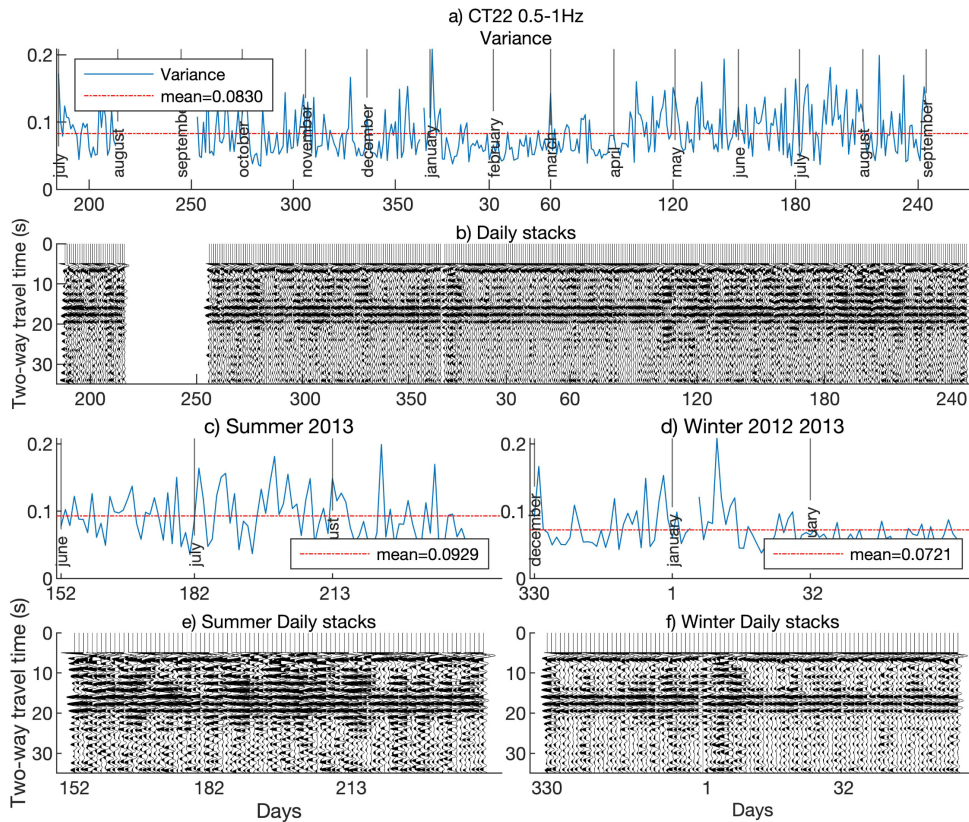


Figure 4.9 (a) The variance of the daily autocorrelation stacks filtered in the 0.5–1 Hz frequency band is shown by the blue curve. The mean variance is indicated by the red dashed-dotted line. (b) The daily autocorrelation stacks of the complete data set. (c) The variance, blue curve, of only the summer daily stacks and (d) the winter daily stacks. The mean variance of the summer daily stacks (e) is ~ 0.093 and higher than both the mean of the complete daily autocorrelation stacks (b) and the mean of only the winter daily stacks (f).

For station CT22, Fig. 4.10, the arrival times of the automatically picked reflectivity changes in the *a priori* time windows correspond to a clear change in reflectivity along the waveforms of the autocorrelations. Therefore, the arrival times of the automatically picked reflectivity changes are chosen as the arrival time of the Moho reflection and the intracrustal discontinuity. The automatically picked arrival times of the intracrustal discontinuity, are related to a clear decrease in amplitude along the waveforms of the autocorrelation stacks that are filtered in the [0.4–1], [0.5–1] and [0.5–2] Hz frequency bands. However, in the [0.3–1] Hz frequency band the automatically picked arrival time of the intracrustal discontinuity is marked by an increase in amplitude that decreases shortly afterwards. The automatically picked arrival times of the Moho reflections are related to a clear increase in amplitude along the waveforms of the autocorrelation stacks that are filtered in all the four different frequency bands. These automatically picked reflectivity changes are very close—difference of ~ 0.89 s TWT—to the manually picked changes in reflectivity, see Figs 4.6(e) to (h), except for the pick related to the intracrustal discontinuity in the [0.3–1] Hz frequency band that has a difference of ~ 3.15 s TWT with the manual pick. Furthermore, the mean difference between the arrival times of the automatically picked reflectivity changes and prior information are ~ 0.46 s TWT, which is smaller than the mean difference between the manually picked reflectivity changes and prior information, ~ 1.17 s TWT, that is mainly due to the manually picked arrival time of the intracrustal discontinuity at a much later time in the [0.3–1] Hz frequency band. The automatically picked reflectivity changes that are associated with the Moho reflections correspond to a clear peak in the *a priori* time window of the second derivative envelope for all the four different frequency bands.

For station CT15, the local maximum inside the *a priori* time window of the second derivative envelope in the 0.3–1 Hz frequency band (Fig. 4.11a) does not identify a single clear value. In addition, for the 0.5–1 Hz frequency band in Fig. 4.11(c) the local maximum is not the only clear peak in the *a priori* time window of the second derivative envelope. Therefore, in stations where the automatically picked arrival time of changes in reflectivity do not correspond to a single clear peak within the *a priori* time window, we associate the Moho reflection with the manually picked arrival time of the most stable reflection along the daily autocorrelation stacks that coincides with a clear change in reflectivity along the final autocorrelation stack. Fig. 4.11(e) shows the daily autocorrelation stacks filtered in the 0.5–1 Hz frequency band together with the manually picked arrival time, green dashed line, at the most stable reflection that coincides with a strong increase in amplitude after the pick along the waveform of the final stack. To have a clear view of the daily stacks, the green dashed line is plotted starting from the middle of the daily plots.

In Figs 4.11(a)–(d), we have only plotted the *a priori* time window of the prior Moho information due to the overlap with the *a priori* time window of the intracrustal discontinuity. The *a priori* time windows overlap when the difference

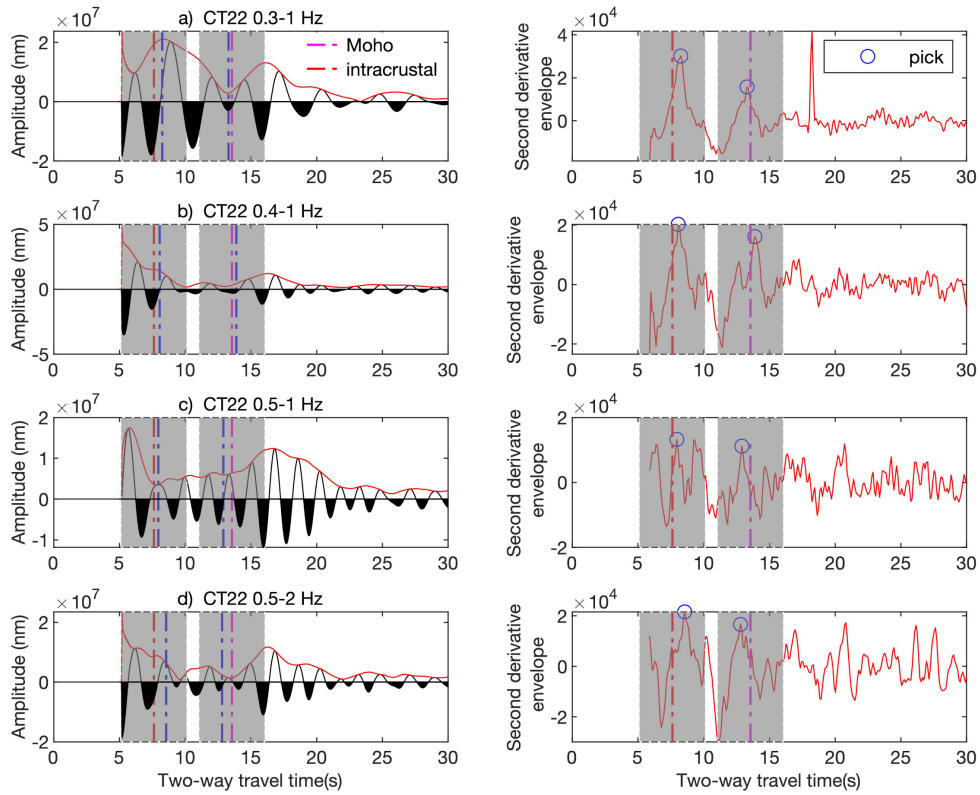


Figure 4.10 Plots on the left: the final autocorrelation stacks of station CT22 after processing the complete data set filtered in the following frequency bands (Hz); (a) [0.3–1], (b) [0.4–1], (c) [0.5–1] and (d) [0.5–2] with the arrival times of the automatically picked reflectivity changes, blue dashed–dotted lines, related to the Moho discontinuity and intracrustal discontinuity. The envelope of the autocorrelation stack is the red line. Plots on the right-hand side; the second derivative of the envelope with the picked reflectivity changes or local maxima, blue circles, inside the a priori time windows, grey windows. The prior Moho information by Zhao et al. (2015) is the pink dashed–dotted line and the red dashed–dotted line is the prior intracrustal information by Zhao et al. (2015).

between the prior Moho and intracrustal discontinuity is smaller than 5 s TWT. We also show the overlap of the *a priori* time windows in Fig. 4.11(f) with the automatically picked changes in reflectivity. The local maximum that is associated with the intracrustal discontinuity is at the border of the *a priori* time window. In addition, this local maximum falls inside the *a priori* time window that is related to the prior Moho information and very close to the manually picked change in reflectivity, green dashed-dotted line, that is selected as the Moho reflection.

In Figs 4.18–4.29, supplementary material in section 4.6, we show the arrival times of the Moho reflections used for the final reflectivity profile in section 4.3.3.

4.3.3 Moho reflectivity across the CIFALPS profile

After picking the arrival times of the Moho reflections, we plot these arrival times with the final autocorrelation stacks of the stations alongside the reference profile (see Fig. 4.1) to image possible lithospheric structures and the Moho discontinuity. In Fig. 4.12(a) the altitude profile of the stations are plotted across the whole CIFALPS transect from west to east, and for each station the autocorrelation stacks filtered in the 0.5–1 Hz frequency band are plotted in the reflectivity profile, Fig. 4.12(b). The autocorrelations and automatically picked arrival times are in two-way traveltime (s) and stacked over the complete data set. The autocorrelation stacks filtered in the 0.5–1 Hz frequency band have been chosen for the reflectivity profile across the CIFALPS transect due to the clear reflectivity changes along the waveforms of the autocorrelation stacks. The reflections of the stations CT30–CT36 are dominated by a repeated 1 Hz signal throughout the stack. After analysing the probability power spectral densities—see section 4.3.3—we exclude the frequency of 1 Hz and create autocorrelation stacks with a lower cut-off frequency of 0.3 Hz frequency. For further analysis of the reflectivity profile across the CIFALPS transect, we have replaced the autocorrelation stacks of stations CT30–CT36 with the stacks filtered in the 0.3–0.9 Hz frequency band (Fig. 4.12c) due to the improved reflection responses and clear reflectivity changes after the picked arrival times of the Moho reflections. In Fig. 4.12(c) the manually picked arrival times of the Moho reflections, green short horizontal lines, are selected for calculation of the Moho depth for the stations where the automatically picked arrival times did not correspond to a clear peak in the *a priori* time window of the second derivative envelope.

In Fig. 4.12(d) the reflectivity profile and the arrival times of the Moho reflections are converted into depth (km), using the velocity model by Zhao et al. (2015), and corrected for elevation. There is some spatial coherence at ~ 18 –23 km depth between the waveforms of the autocorrelation stacks of different stations from the beginning of the CIFALPS line, -150 km from the Frontal Penninic thrust (FPT—0 km), to -70 km and from -30 to 30 km after the FPT. Coherence then disappears into strong lateral variations towards the eastern end of the profile. Furthermore, from

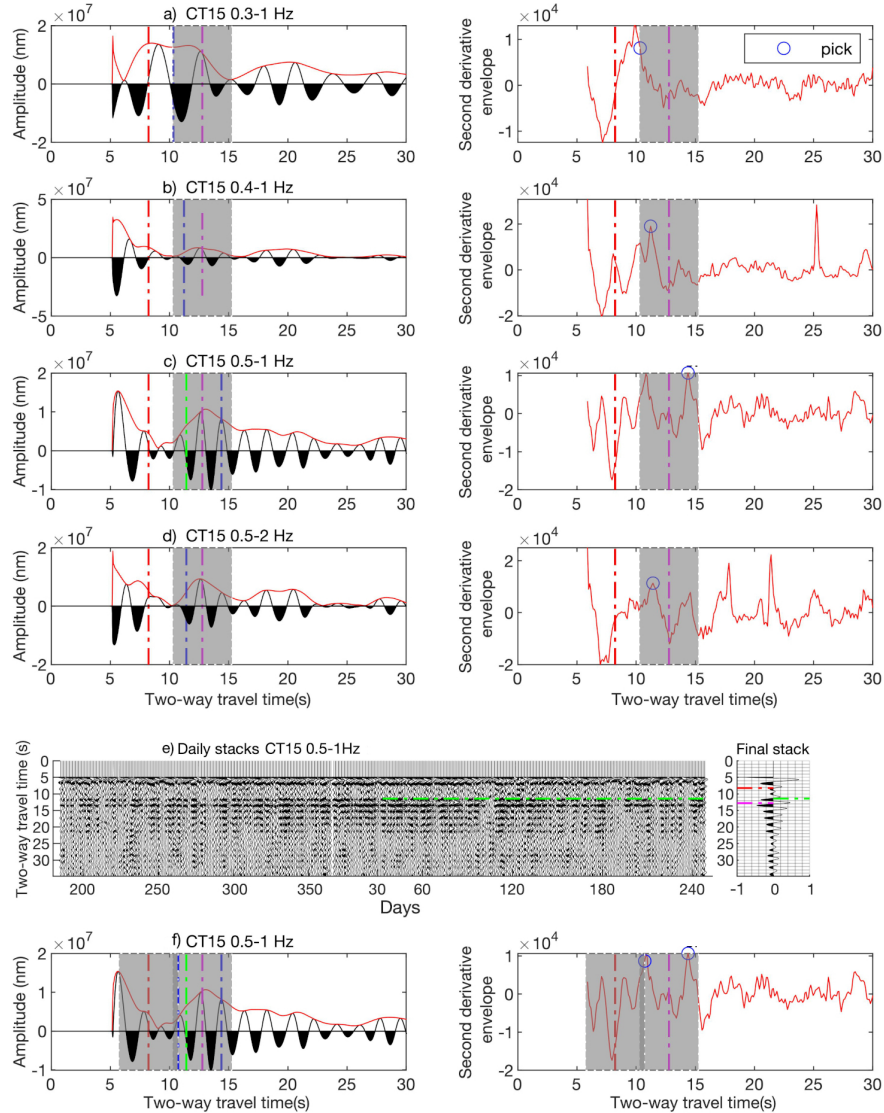


Figure 4.11 Plots on the left: the final autocorrelation stacks of station CT15 after processing the complete data set filtered in the following frequency bands (Hz); (a) [0.3–1], (b) [0.4–1], (c) [0.5–1] and (d) [0.5–2] with the arrival times of the automatically picked reflectivity changes, blue dashed–dotted lines, related to the Moho discontinuity and (f) intracrustal discontinuity. The envelope of the autocorrelation stack is the red line. Plots on the right-hand side; the second derivative of the envelope with the picked reflectivity changes or local maxima, blue circles, inside the a priori time windows, grey windows. The prior Moho information by Zhao et al. (2015) is the pink dashed–dotted line and the red dashed–dotted line is the prior intracrustal information by Zhao et al. (2015). The manually picked arrival time associated with the Moho reflection is shown by the green dotted line in (c) at the most stable reflection along the daily stacks (e) and coincides with a clear change in reflectivity along the waveform of the final stack. (f) The automatically picked arrival time of the intracrustal discontinuity is close to the manually picked arrival time of the Moho reflection as opposed to the prior intracrustal information by Zhao et al. (2015).

–150 to –100 km from the FPT the reflectivity fades after the Moho reflections, due to a clear decrease in amplitude along the waveforms of the autocorrelation stacks. However, from –100 km to the FPT there is vertical continuity of reflectivity down to 75 km depth and in between the stations there is weak spatial coherence. The Moho reflections in the eastern part of the profile line, 100–170 km after the FPT, are shallower than in the western part, –150 to 50 km after the FPT. The deepest Moho reflections are at the stations CT30 and CT31, at a depth of around 70 km.

Analysis autocorrelation stacks CT30

In Fig. 4.13 the results of the autocorrelation stacks for station CT30 are shown. The stack filtered in the 0.5–1 Hz frequency band is very noisy. This behavior in the 0.5–1 Hz frequency band has also been observed for nearby stations, CT31–CT36. Therefore, the probability power spectrum and spectrogram, Figs 4.13(h) and 4.13(i) (retrieved from: <http://dx.doi.org/10.15778/RESIF.YP2012>), has been analyzed to detect the ambient noise behaviour along the seismic frequency. In the probability power spectrum there is a high probability value observed around 1 s period, 1 Hz, that has been outlined by the green rectangle in Fig. 4.13(h). We exclude the frequency of 1 Hz with a smaller cut-off frequency of 0.3 Hz, the autocorrelation stacks show a clear reflection response in the 0.3–0.8 Hz and 0.3–0.9 Hz frequency bands. The 0.3–0.9 Hz frequency band, Fig. 4.13(c), has been chosen for the CT30–CT36 stations in the final reflectivity profile across the CIFALPS. The 1 Hz signal may be due to instrumental problems since at this specific frequency there is very little variance in the probability power spectrum.

There is a change in reflectivity at ~ 30 s TWT, that is characterized by a decrease in amplitude along the waveform of the autocorrelation stack, Fig. 4.13(c). This change in reflectivity might be associated with the end of the crust–mantle reflection phase. The 30 s TWT is in depth ~ 100 km. Assigning this reflectivity change to a layer at ~ 100 km is most unlikely since there is no evidence of such deep layers in this area.

Moho reflectivity from manual picking

We have also picked the Moho reflections manually for the stations where the automatic method corresponded to a single clear peak within the *a priori* time window of the second derivative envelope. The depth of the manually picked Moho reflections are shown together with the outline of the geological cross-section by Zhao et al. (2015), see Fig. 4.14. The mean difference between the depth of the manually picked Moho reflections and the depth by Zhao et al. (2015) is 1.1 ± 1.3 km. The Moho depths from the manually picked reflections are mostly deeper beneath the western end of the profile, –75 km to the FPT, than the study by Zhao et al. (2015). The mean difference between the depth of the automatically picked Moho reflections and the depth by Zhao et al. (2015) is -1.8 ± 0.9 km. The Moho depths from the automatically picked reflections are mostly shallower than the study by Zhao et al.

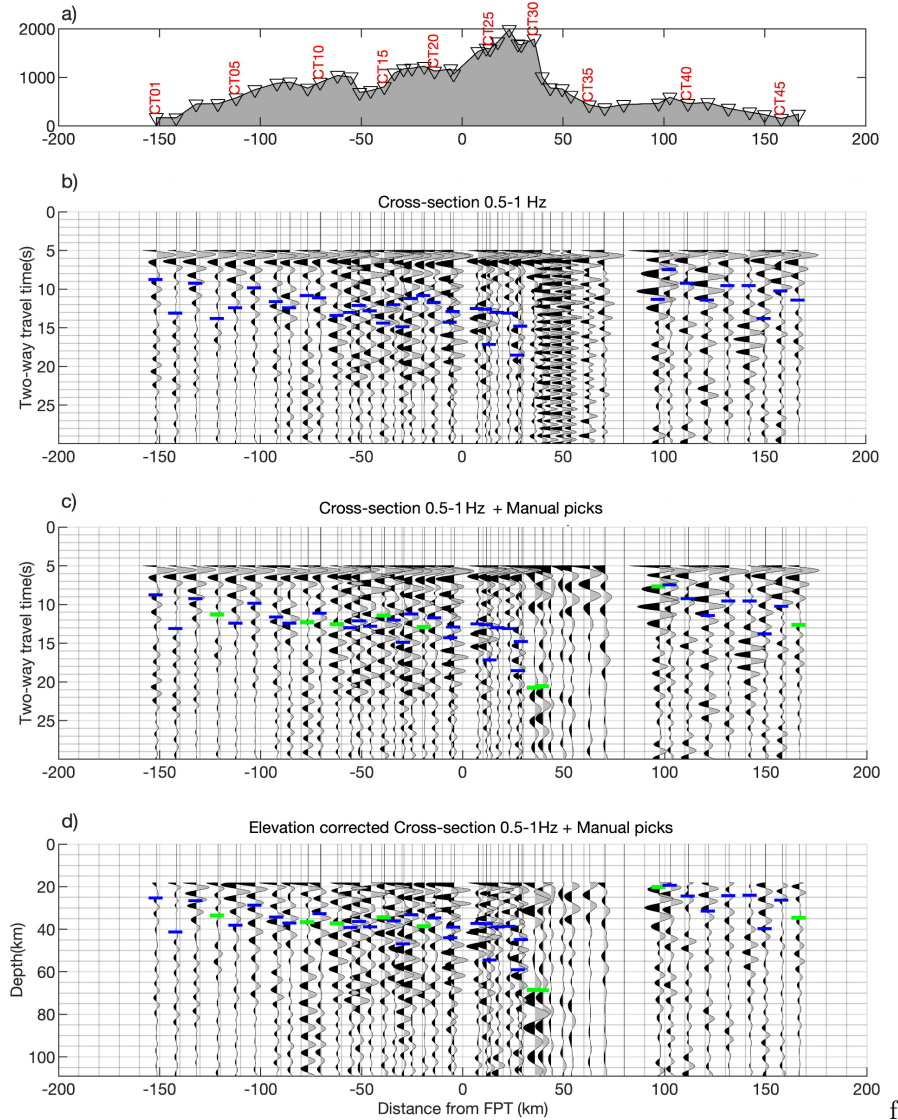


Figure 4.12 (a) Altitude profile in metres for the CIFALPS transect from west to east. Stations are shown by the inverted triangles; labels in red represent the station codes. The distance is measured from the Frontal Penninic Thrust (FPT) shown in Fig. 4.1. (b) The autocorrelation stacks in the 0.5–1 Hz frequency band of the CIFALPS stations are plotted in two-way traveltime, with the arrival times of the automatically picked reflectivity changes that are related to the Moho reflection, blue short horizontal lines. (c) The stacks of stations CT30–CT36 are replaced with the 0.3–0.9 Hz autocorrelation stacks due to the improved reflection response after excluding the 1 Hz signal. The automatically picked arrival times that do not correspond to a clear change in reflectivity along the waveforms of the autocorrelation stacks are replaced by the arrival times of the most stable reflection that are chosen as the Moho reflection, green short horizontal lines. (d) The autocorrelation reflectivity profile and the arrival times of the Moho reflection are migrated to depth (km), and corrected for elevation, using the velocity model by Zhao et al. (2015).

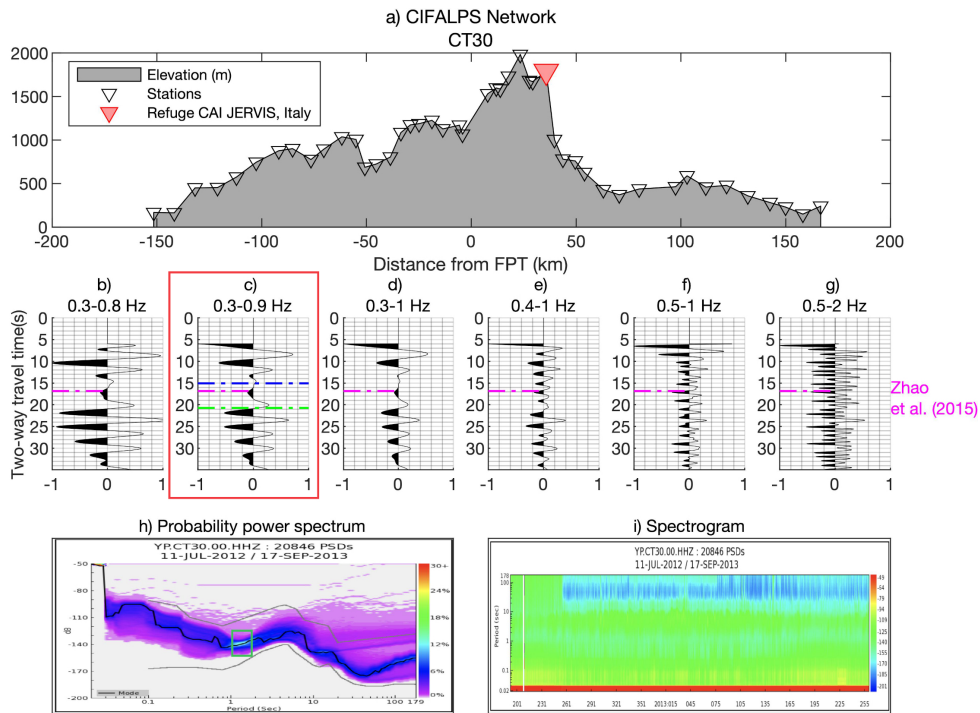


Figure 4.13 (a) Stations of the CIFALPS profile are plotted in elevation (m) from west to east. The position of Station CT30 is highlighted by the red upside down triangle. (b) The autocorrelation stacks of station CT30 are shown in the following frequency bands (Hz); (b) [0.3–0.8], (c) [0.3–0.9], (d) [0.3–1], (e) [0.4–1], (f) [0.5–1], (g) [0.5–2]. The autocorrelation stack in the 0.3–0.9 Hz frequency band, highlighted by the red rectangle, is selected for the final autocorrelation reflectivity profile along the CIFALPS transect (see Fig. 4.16). The prior Moho information by Zhao et al. (2015) is indicated by the pink dashed–dotted line, the arrival time of the manually picked Moho reflection is indicated by the green dashed–dotted line and the arrival times of the automatically picked Moho reflection by the blue dotted line. (h) Probability power spectrum. The green rectangle highlights the high probability signal with little variance. (i) Spectrogram. Panels (h) and (i) are retrieved from: <http://dx.doi.org/10.15778/RESIF.YP2012>.

(2015), see Fig. 4.14(c). For each station, the difference between the Moho depth from manual picking and the Moho depth obtained from the automatic method is shown in Fig. 4.14(d). There are large differences at the beginning of the line, the middle of the western end of the profile, -75 to -10 km from the FPT, and at the start of the subduction zone, 30 – 50 km after the FPT. The mean difference between the Moho depth from manual picking and Moho depth from the automatic method is 2.8 ± 1.8 km.

4.4 Discussion

The main goal of this study is to image the reflectivity of the crust–mantle boundary, and where possible detect reflectivity structures of the lithosphere, from autocorrelations of ambient seismic noise along the CIFALPS profile. Autocorrelation stacks for all the stations show indication of a gradational, as opposed to sharp, Moho interface because of the absence of a corresponding dominant pulse. In this case it is helpful to identify the Moho based on prior information (e.g. Kennett et al., 2015; Becker & Knapmeyer-Endrun, 2018). Therefore, the method of Becker & Knapmeyer-Endrun (2018) that is based on prior information is a helpful tool to pick the reflectivity changes that are associated with the Moho discontinuity. We have only used the prior information by Zhao et al. (2015) due to the well-defined final crustal model that aid in the interpretation of the autocorrelation reflectivity profile.

4.4.1 Moho reflectivity from ambient noise autocorrelation

In Fig. 4.15, we use the Moho from the ambient noise tomography study by Lu et al. (2018) to investigate the effect on picking the arrival time of the Moho reflection with a different prior information. The study by Lu et al. (2018) resulted into a shallower Moho depth of 5 – 8 km at the western end of the profile, beneath the Southeast Basin, than the study by Zhao et al. (2015). In other areas along the profile it is in good agreement with Zhao et al. (2015). Therefore, we have selected station CT01 that is positioned at the western end of the profile where the Moho from Zhao et al. (2015) and Lu et al. (2018) have the largest difference, ~ 8 km. The local maximum inside the *a priori* time window of the second derivative envelope is the same peak with the same arrival time, see Fig. 4.15, for using the prior Moho by; (a) Zhao et al. (2015), (b) Lu et al. (2018) or (c) average of the aforementioned prior Moho. This shows that the picked arrival times of the Moho reflections, for stations where previous studies resulted in large Moho depth differences, are robust since the arrival time stays the same when using a different prior Moho.

The reflectivity changes are automatically picked inside *a priori* time window set at a length of 5 s TWT that is around 18 km and is not defined by uncertainties of the prior Moho information or velocity model by Zhao et al. (2015) since these values are

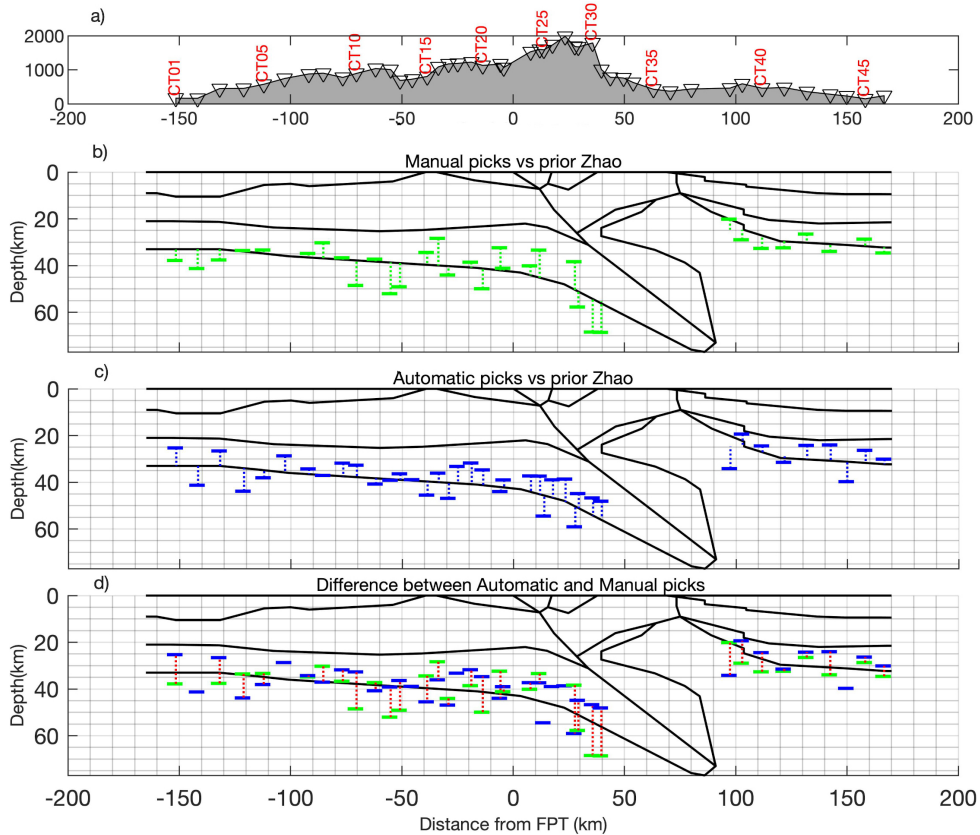


Figure 4.14 (a) Altitude profile in metres for the CIFALPS transect from west to east. Stations are shown by the inverted triangles; labels in red represent the station codes. The distance is measured from the Frontal Penninic Thrust (FPT) shown in Fig. 4.1. (b) The green horizontal lines: Moho depths calculated from the manually picked arrival times of the Moho reflections. The green vertical dotted lines indicate the differences with the Moho depth determined by Zhao et al. (2015). The mean difference is 1.1 ± 1.3 km. (c) The blue horizontal lines: Moho depths calculated from the automatically picked arrival times of the Moho reflections. The blue vertical dotted lines indicate the differences with the Moho depth determined by Zhao et al. (2015). The mean difference is -1.8 ± 0.9 km. (d) The red vertical dotted lines indicate the differences between the (b) Moho depths from the manually picked arrival times, green lines, and the (c) Moho depths from the automatically picked arrival times, blue lines. The mean difference is 2.8 ± 1.8 km.

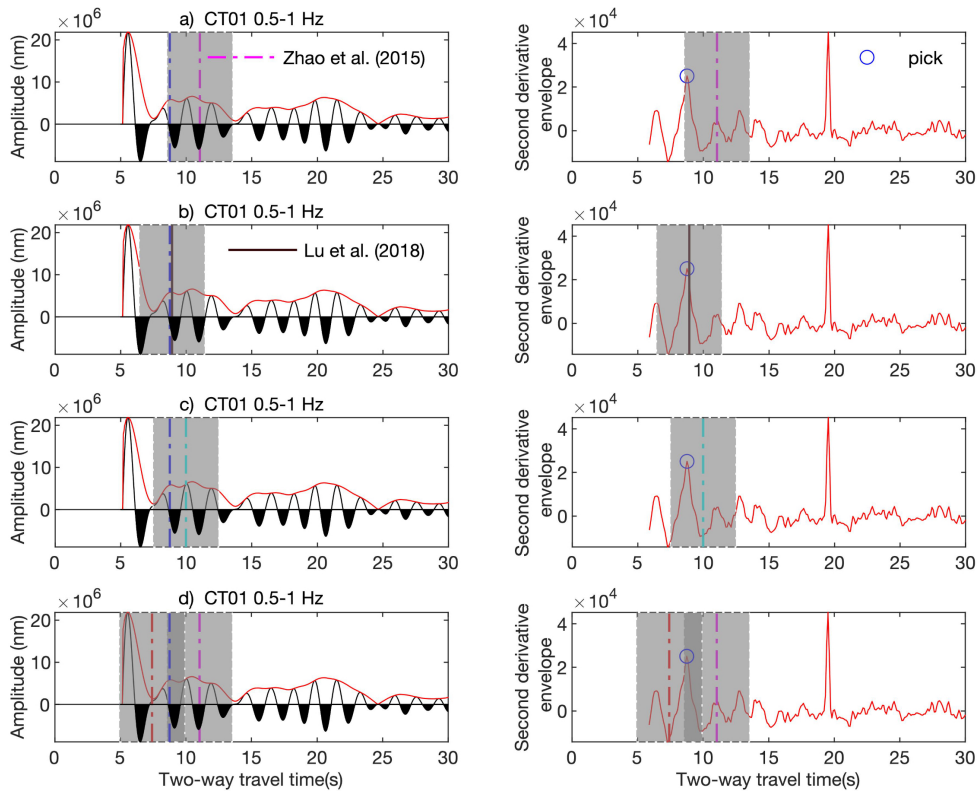


Figure 4.15 Plots on the left: the final autocorrelation stacks of station CT01 in the 0.5–1 Hz frequency band with the automatically picked arrival times of the Moho reflections, blue dashed–dotted lines, based on the prior information by: (a) Zhao et al. (2015), pink dashed–dotted line, (b) Lu et al. (2018), brown dashed–dotted line and (c) the average of the aforementioned Moho information, cyan coloured line. (d) The prior intracrustal, red dashed–dotted line, and Moho information by Zhao et al. (2015). The envelope of the autocorrelation stack is the red line. Plots on the right-hand side: the second derivative of the envelope with the picked reflectivity changes or local maxima, blue circles, inside the a priori time window, grey window.

not available. In the study by Becker & Knapmeyer-Endrun (2018), the arrival time of the Moho reflections across the Trans-European Suture Zone are picked inside *a priori* time windows that vary based on the uncertainties of the selected prior Moho and velocity model. Their prior time windows generally resulted in shorter windows, < 5 s TWT. However with the larger *a priori* time window that is fixed at 5 s TWT, we take into consideration more changes in reflectivity that may be associated with the Moho reflection and the results are less biased to the uncertainties of the prior information. Furthermore, the manually picked arrival times of the Moho reflections are not confined to a fixed *a priori* time window. This results in a maximum of ~ 1.4 s TWT, which is at station CT30, outside the *a priori* time window.

We have not applied Automatic Gain Control (AGC), that is commonly used in exploration seismology, since the method of Becker & Knapmeyer-Endrun (2018), that we also use here, is based on picking reflectivity changes. The reflectivity changes that we have observed in Figs 4.6, 4.10 and 4.11 are mainly associated with changes in amplitude. AGC increases the amplitude levels of weak signals. In our study, the changes in amplitude are important to detect reflectivity changes that are associated with the Moho interface. Therefore, we leave the character of the autocorrelations in its original state.

We have shown that by stacking only the daily autocorrelations of the winter months in the time interval of 5–35 s TWT (Fig. 4.8f), the final winter stack is very similar to the final stack of the complete data set with a correlation coefficient of 0.99. The winter daily stacks reach stability faster, most likely because of the winter storms resulting in a more diffuse and stable noise field, and hence more stable *P*-wave reflection signals. In a very different environment, Schimmel et al. (2021) have shown that autocorrelation convergence speed generally worsen with increasing lag time. In our data, we observe that convergence is faster for the whole correlogram in winter as opposed to summer. Weaker generation of ambient noise may therefore lead to a general increase of variance in the broad lag time window.

4.4.2 Preferred frequency band

The choice of frequency band is very important as we can see from the results of Figs 4.7, 4.10 and 4.11. In Fig. 4.7 the waveforms of the daily autocorrelation stacks filtered in the [0.3–1] and [0.5–2] Hz frequency bands are less coherent than the daily stacks filtered in the [0.4–1] and [0.5–1] Hz frequency bands. The coherence between the waveforms of the daily stacks is important since the manually picked arrival time of the Moho reflection is associated with the most stable reflection along the daily stacks that coincides with a clear change in reflectivity along the final autocorrelation stack. In Figs 4.10 and 4.11, the arrival time of the automatically picked reflectivity changes are associated with a clear change in amplitude along the waveforms of the autocorrelations that are filtered in the 0.5–1 Hz frequency band.

The change in amplitude is also visible in the 0.4–1 Hz frequency band, but not as notable. Therefore, we have chosen the seismograms that are filtered in the 0.5–1 Hz frequency band, as we observe a clear change in reflectivity after the picked arrival times of the Moho reflections due to the transition between the crust and mantle.

Below 1 Hz, the dominant source of the ambient seismic wavefield is oceanic gravity waves. The 0.5–1 Hz frequency band is within the secondary microseisms range (0.1–1 Hz) whose excitation sources are distributed in both shallow, coastal areas and pelagic areas (Nishida, 2017). Above 1 Hz, the dominant source of the wavefield is human activities (Bonney-Claudet et al., 2006). In the 0.5–2 Hz frequency band, the wavefield is excited by both oceanic gravity waves, below 1 Hz, and human activities, above 1 Hz. At frequencies higher than 1 Hz, seismic noise systematically exhibits daily and weekly variations linked to human activities. These human activities that change on a daily base may explain the high variance observed between the daily stacks in the 0.5–2 Hz frequency band (Fig. 4.7d).

In contrast to our best results in the 0.5–1 Hz frequency band, the studies by Becker & Knapmeyer-Endrun (2018) and Becker & Knapmeyer-Endrun (2019a) show best results in the 1–2 Hz range. The chosen frequency range may be different due to the different characteristics of the seismic station sites, and the noise field. The stations in this study are situated near the Ligurian Sea while those of Becker & Knapmeyer-Endrun (2018) near the Baltic Sea, two very different geological environments. A further study on the effects of ambient seismic noise level from different sea regions and site characters can give more insight on the best frequency window range.

In addition to the different chosen frequency ranges, different types of processing might influence the waveform of the final stack due to the signal and noise characteristics (Schimmel, 1999). We have applied a classical autocorrelation with amplitude normalization by using 1-bit time-domain normalization whereas Becker & Knapmeyer-Endrun (2018) has used the phase autocorrelation method by Schimmel (1999). Schimmel et al. (2018) have shown that for the extraction of Earth orbiting surface waves from vertical-component seismograms the waveform of the amplitude unbiased phase autocorrelation stacks closely matches to the classical autocorrelation that uses amplitude normalized data. However, the same results were not achieved for the autocorrelation stacks filtered in a higher frequency band that might have been due to the quantity of the data used for the final stack. Therefore, there might be an influence of different processing steps. Nevertheless, more research can be done to give insight on how different processing steps behave in different frequency bands and on the extraction of Moho reflected P -waves.

In this study we can observe layers starting from around 18 km, Fig. 4.12(d), since the autocorrelated stacks are plotted from 5 s TWT, to avoid the dominance of the large pulses at and after 0 s. To estimate the vertical resolution of the reflectivity

profile in the the 0.5–1 Hz frequency band, we take into consideration the general threshold of $\lambda/4$ (e.g. Yilmaz, 2001). In the upper crust along the CIFALPS profile, the seismic wavelength ranges from 6 km for the 1 Hz seismic wave to 12 km for the 0.5 Hz seismic wave. The 6 km wavelength can observe an upper crust down to 1.5 km thick, whereas the 12 km wavelength can observe a minimum thickness of 3 km. In the lower crust the wavelengths are ranging from 6.6 to 13.2 km and the minimum resolvable layer thickness ranges between 1.65 and 3.3 km. The minimum thickness of the upper and lower crust are ~ 4 and ~ 6.6 km (Zhao et al., 2015), respectively, so even with the longer wavelengths of the 0.5 Hz frequency wave the interfaces of the upper and lower crust may be resolved. To improve the vertical resolution and resolve layers that are shallower than 18 km, including higher frequency waves may be of great importance.

4.4.3 Lithospheric structures from ambient noise autocorrelation

In Fig. 4.16 we compare the Moho depths calculated from the arrival times of the picked reflectivity changes along the autocorrelation stacks in the 0.5–1 Hz frequency band to the structure of the geological cross section by Zhao et al. (2015). This comparison aids also in interpreting the different characters observed along the reflectivity profile, marked by cyan–green outlines from (1) to (4). The eastward dipping subduction trend of the European Moho going underneath the Adriatic Moho can clearly be followed with the Moho depths obtained in this study. From –150 to 30 km from the FPT, the Moho depths of this study are mostly shallower than the receiver function study by Zhao et al. (2015) and matches more closely to the Moho depths estimated by Lu et al. (2018). The earlier Moho arrivals in the eastern part of the cross section are related to the shallow depths of the Adriatic Moho. These shallow Moho depths have also been detected in the Moho maps by Lu et al. (2018) from surface wave tomography. The spatial coherence in the western part of the profile between ~ 18 and 23 km depth, marked by the cyan–green lines (1) in Fig. 4.16(c), falls within the relatively homogenous crustal structure by Zhao et al. (2015). This homogenous behaviour has also been detected in the shear wave velocity models by Lyu et al. (2017). The coherence at these shallow depths after conversion of the time domain reflectivity profile starting from 5 s TWT, is unlikely to be influenced by the zero-lag sidelobes. The sidelobes wavelength are highly dependent on the frequency bandwidth: Romero & Schimmel (2018) have shown that the sidelobes are longer and arrive at later lag times for the frequency bands with a lower cut-off frequency. In our study, the effect of the zero-lag sidelobes from 5 s TWT has been discarded since the coherence detected between the waveforms of the daily autocorrelation stacks at early arrival times in the 0.5–1 Hz frequency band, Fig. 4.7(c), is not detected in the 0.3–1 Hz frequency band, Fig. 4.7(a), that would otherwise also show coherence but with longer wavelengths if there were influence from the zero-lag sidelobes.

The deeper reflections after the Moho reflections, marked by the cyan–green ellipse (2) in Fig. 4.16(c), from -100 km to the FPT along the CIFALPS profile fall right below the fault zone underneath the Southeast basin. The high amplitudes of these reflections were observable at stations in or near the fault zone, but not at stations further away. Li et al. (2007) demonstrated that the boundaries of fault zones create multiple reflections on synthetic seismograms. In addition, Lai et al. (2010) detected fault-zone trapped waves caused by multiple reflections between two boundaries of the fault and the wave interference. Whereas, Taylor et al. (2016) detected reduced reflectivity of the crustal–mantle boundary in the autocorrelations near the North Anatolian Fault zone fault. In our study, the Moho will not be affected by reduced reflectivity since the crustal–mantle boundary is based on the highest change of the slope in the envelope. So the deeper reflections detected in this study after the Moho reflection may be related to multiple reflections inside the fault zone. They cannot be related to deeper layers since there is no evidence of such layers in this study area. Furthermore, Kennett (2015) and Becker & Knapmeyer-Endrun (2019a) concluded that associations of deeper arrivals to asthenospheric depths is questionable since contaminations from shallow structures might influence those arrivals. Another study by Tibuleac & von Seggern (2012) associated deeper arrivals to Moho-reflected- S waves since there is no support of deeper layers from previous studies in their study area. However, we are considering to create synthetic autocorrelations in a further study to give more insight on these arrivals.

The highly reflective Moho along the CIFALPS becomes suddenly transparent to seismic waves between 50 and 100 km from the FPT, marked by the cyan–green circle (3) in Fig. 4.16(d). The reflection-free, transparent area falls within the position of the Ivrea body by Zhao et al. (2015). The Ivrea body is a high density and high-velocity body that reaches crustal depths as a slice of serpentinized Adriatic upper mantle (Closs & Labrousse, 1963; Nicolas et al., 1990). The reflective transparency might be due to the presence of upper-mantle material at shallow depths, which has also been detected by the active seismic study of Nicolas et al. (1990). The ambient noise of the stations in the reflective transparent area have for the frequency range of 0.3–1 Hz the same level, ~ -150 to -120 dB, and follow the same trend as compared to stations outside this area (see Fig. 4.17). Therefore, it is most unlikely that the transparency of the seismic reflection might be due to different ambient noise levels.

Furthermore, the lateral variations observed towards the eastern end of the profile has also been observed in the v_S velocity models by Lyu et al. (2017) that shows strong lateral variations and very high velocities of lithospheric mantle beneath the Po Plain with very low velocities at the deeper parts. The deepest Moho reflections at the stations CT30 and CT31 are ~ 70 km, and ~ 15 km deeper than the prior Moho depth of ~ 55 km by Zhao et al. (2015) underneath the same stations. The extent of the Moho that is marked by the cyan–green line (4) in Fig. 4.16(d) follows a steeper trend compared to the prior Moho profile by Zhao et al. (2015) and Lyu

et al. (2017). The shape of the Moho shows a clear steeper dip from ~ 55 to ~ 70 km.

Associating the Moho reflection to the most stable reflection along the daily autocorrelation stacks without prior information might result into picking a stable reflection from another discontinuity. In Fig. 4.11(e) there is a stable reflection along the daily stacks, at ~ 7 s TWT, that is associated with a clear change in reflectivity along the final stack and very close to the intracrustal discontinuity obtained from Zhao et al. (2015), at ~ 8 s TWT. Furthermore, the Moho depths obtained from picking manually the most stable reflections along the daily autocorrelation stacks (Fig. 4.14b) resulted mostly deeper in the middle of the CIFALPS profile, -70 to -10 km from the FPT, than the results from the automatic method and prior information by Zhao et al. (2015). These results might be biased due to the stable multiple reflections, from the fault zone area underneath the Southeast basin, that are arriving at later times. The method of Becker & Knapmeyer-Endrun (2018) that is based on prior information to extract the largest changes in the slope of the envelope has proven to not be affected by the deeper reflections or by stable reflections from the intracrustal discontinuity.

4.4.4 Intracrustal discontinuity from ambient noise autocorrelation

In addition to picking the arrival times associated with the Moho reflection, we apply the automated picking method by Becker & Knapmeyer-Endrun (2018) to investigate the possibility of detecting the intracrustal discontinuity. For station CT22, the automatically picked arrival time of the intracrustal discontinuity is clearly separated from the arrival time of the Moho discontinuity. This is not the case for station CT15, Fig. 4.11(f), where the automatically picked arrival time of the intracrustal discontinuity is very close to the reflectivity change associated with the Moho reflection. Another outcome is that the automatically picked arrival time of the intracrustal discontinuity corresponds to the same peak that is associated with the reflectivity change of the Moho discontinuity, and thus at the same arrival time, see Fig. 4.15(d) for station CT01. The automatically picked arrival time closely matches the shallower Moho information by Lu et al. (2018), Fig. 4.15(b). Shortening the *a priori* time windows may solve the problem but would not exclude the possibility that the arrival time of the automatically picked change in reflectivity related to the intracrustal discontinuity might be associated with a deeper discontinuity.

The seismic *P*-wave velocity changes across the intracrustal and Moho discontinuity might give insight on the character of the reflectivity changes or local maxima inside the *a priori* time window of the second derivative envelope when the two discontinuities lie close to each other. The *P*-wave velocity model of Zhao et al. (2015) increases from 6.0 to 6.6 km s $^{-1}$ for the upper to lower crust, intracrustal

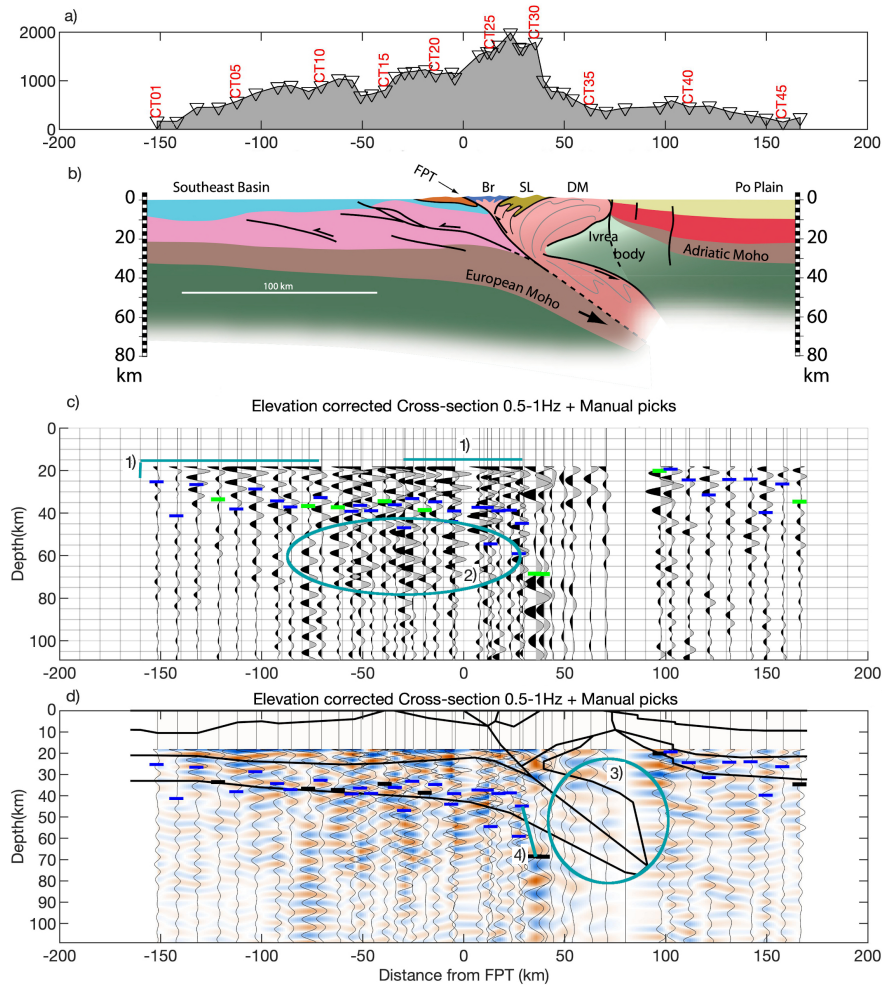


Figure 4.16 (a) Altitude profile in metres of the CIFALPS stations from west to east, the distance is given from the Frontal Penninic Thrust (FPT) show in Fig. 4.1. (b) The geological cross-section from the receiver function study by Zhao et al. (2015). (c) The autocorrelation reflectivity profile plotted in depth (km) after correcting for elevation. The Moho depths calculated from the arrival times of the automatically picked reflectivity changes are given by the blue short horizontal lines and the depths of the Moho reflections from manual picking by the green and black short horizontal lines in (d). The velocity model by Zhao et al. (2015) has been used. The spatial coherence in the western part of the profile, marked by the cyan–green lines (1), coincide with the relatively homogeneous crustal structure. In addition, the deeper reflections after the depths of the Moho reflections that are marked by the cyan–green circle (2) might be the multiple reflections due to the fault zone. See text for further explanation. (d) The autocorrelation stacks are plotted on the image view created from the reflections. The positive lobes are plotted on top of the red colour and the negative lobes on top of the blue colour. The outline, thick black lines, of the geological cross-section in (b) are plotted on top of the reflection profile. The cyan–green circle (3) highlights the transparent reflectivity profile and might be due to the effect of the Ivrea Body. The steep extent of the Moho is marked by the cyan–green line (4). See text for further explanation.

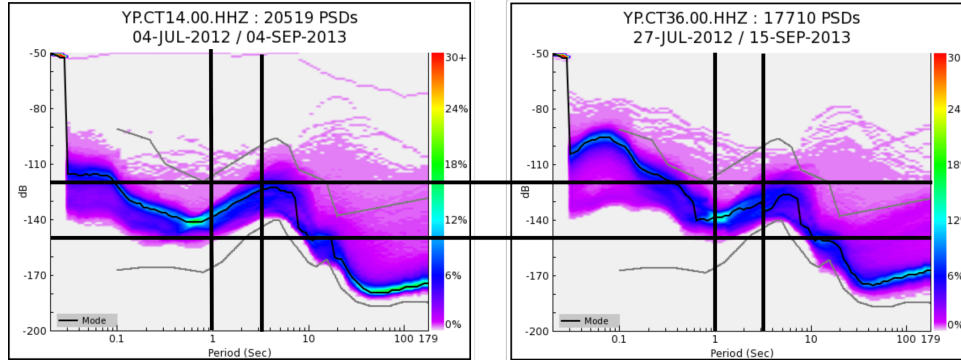


Figure 4.17 The probability density function of the power spectral densities (PSDs) of the stations CT14 and CT36 (figures retrieved from: <http://dx.doi.org/10.15778/RESIF.YP2012>). The black lines outline the periods along the x-axis at 1 s and ~ 3.3 s, 1 Hz and 0.3 Hz, respectively. In addition, the noise level values of -120 and -150 db are outlined at the y-axis. The stations that are at different positions along the CIFALPS line show the same behaviour, the noise increases from -150 to -120 db for wavelengths from 1 s to ~ 3.3 s.

discontinuity, and from 6.6 to 8.2 km s^{-1} for the lower crust to mantle, Moho discontinuity. The velocity change for the intracrustal discontinuity is not as large as the Moho discontinuity. These different velocity changes might result into the peak of the reflectivity change associated with the intracrustal discontinuity being lower than the peak of the Moho discontinuity. This higher peak of the Moho discontinuity outweighs the lower peak of the intracrustal discontinuity when picking the local maximum inside the *a priori* time window. Therefore, when two discontinuities are close to each other the discontinuity with the smaller velocity change might be biased by the discontinuity with a larger change in velocity that creates a higher peak inside the *a priori* time window of the second derivative envelope. A further study needs to be done on how the reflectivity change of the intracrustal discontinuity is affected by the reflectivity change of the Moho discontinuity when they lie close to each other.

4.5 Conclusions

We show that ambient noise autocorrelations coherently image the reflectivity structure of the crust–mantle boundary, and thus clearly depict the subduction of the European Plate underneath the Adriatic micro plate. We have created autocorrelations in the $[0.09-0.5]$, $[0.1-0.5]$, $[0.1-1]$, $[0.3-1]$, $[0.4-1]$, $[0.5-1]$, $[0.5-2]$ and $[1-2]$ Hz frequency band by stacking hourly segments over the complete data set of the CIFALPS. The effects from earthquakes and powerful events have been removed by applying sign-bit normalization (Bensen et al., 2007). We have picked the arrival

time of the Moho reflection by automatically picking reflectivity changes (Becker & Knapmeyer-Endrun, 2018) and using prior information from Zhao et al. (2015). The results are the best in the 0.5–1 Hz frequency band due to the clear change in reflectivity along the waveforms of the autocorrelation stacks after the arrival time of the Moho reflections. The dense station spacing of the CIFALPS makes it easy to detect the different geological structures along the autocorrelation reflectivity profile. The western part of the profile is characterized by spatial coherence at shallow arrivals, due to the homogenous crustal structure at shallow depths (Zhao et al., 2015). After the depth of the Moho reflections in the western part there is a zone with strong reflections, that are possibly due to the multiple reflections caused by the boundaries of the fault zone (Li et al., 2007). The eastern part of the profile is marked by a reflective transparent area due to the Ivrea body reaching shallow crustal depths (Closs & Labrouste, 1963; Nicolas et al., 1990). The subduction profile of the European Plate shows a steep trend as compared to previous studies by Zhao et al. (2015) and Lyu et al. (2017). Our observations show the ability of mapping not only homogenous structures but also highly laterally heterogeneous structures.

4.6 Supplementary Material

In Figs 4.18 to 4.29, we show the arrival times of the Moho reflections used for the final reflectivity profile in section 4.3.3. Figs 4.28 and 4.29 show the stations with the arrival times of the Moho reflections from manual picking. The stacks are plotted in shorter normalized time windows for better visualization of the stable reflections along the daily stacks.

For the following stations; CT01, CT02, CT03, CT04, CT05, CT07, CT09, CT11, CT15, CT17, CT19, CT22, CT23, CT24, CT27, CT28, CT29, CT30, CT31, CT38, CT41, CT43, CT45, CT46, the reflectivity changes are clear at the picked arrival times of the Moho reflections. These changes are related to either an increase or decrease in amplitude of the reflections. The stations CT21 and CT25 are related to a change in frequency at the picked arrival times of the Moho reflections. For the stations; CT06, CT08, CT10, CT12, CT13, CT14, CT16, CT18, CT20, CT26, CT39, CT40, CT42, CT44, the reflectivity changes are not as clearly visible at the picked arrival times of the Moho reflections. But the picked arrival times are still related to changes in the slope that can be detected by using the method of Becker & Knapmeyer-Endrun (2018). We have not detected different types of reflectivity changes that may be dependent on the type of tectonic regime.

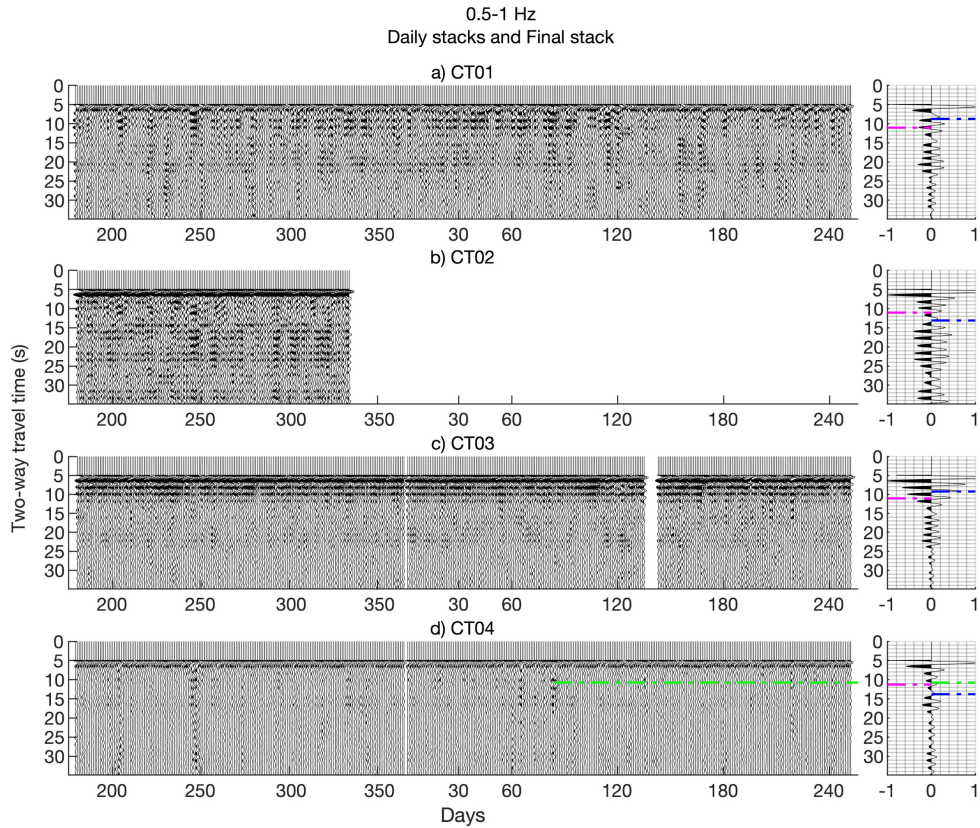


Figure 4.18 The daily autocorrelation stacks for stations (a) CT01, (b) CT02, (c) CT03 and (d) CT04. The final stack of the daily stacks is shown in the graph on the right-hand side for each station. The prior Moho information by Zhao et al. (2015) is indicated by the pink dashed-dotted line and the arrival time of the Moho reflection from the automated method by Becker & Knapmeyer-Endrun (2018) by the blue dashed-dotted line. The arrival time of the Moho reflection from picking the most stable reflection along the daily stacks, green dashed-dotted line, is used for the final reflectivity profile. See Fig. 4.28(a) for better visualization of the stable reflection.

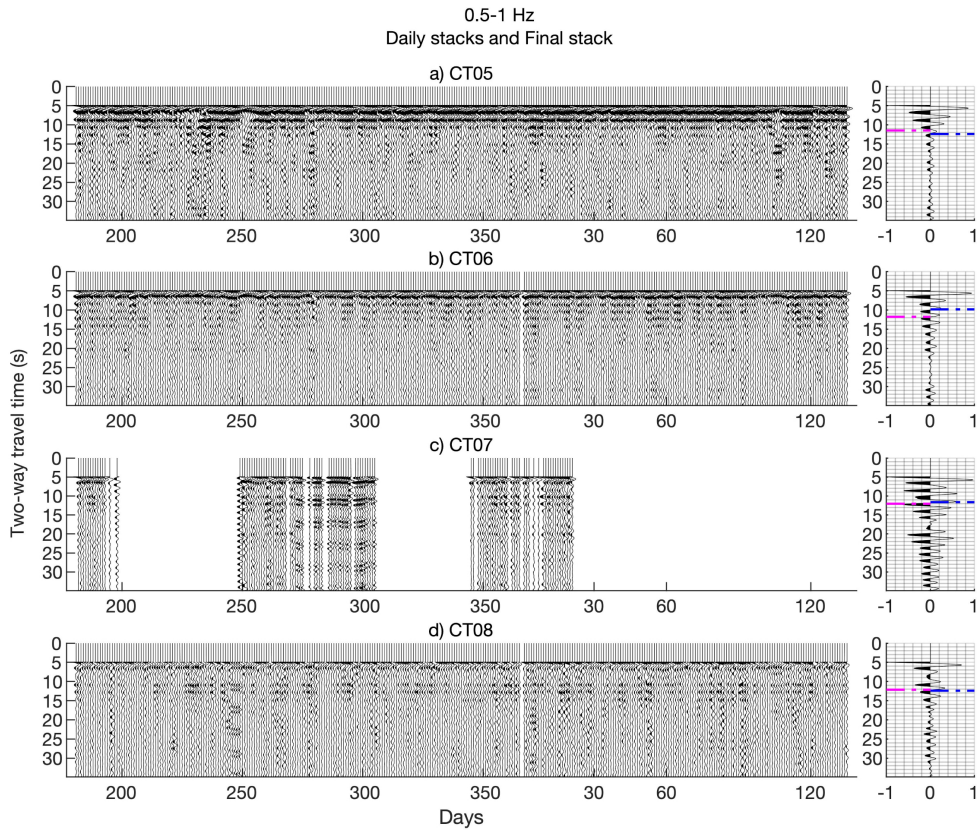


Figure 4.19 The daily autocorrelation stacks for stations (a) CT05, (b) CT06, (c) CT07 and (d) CT08. The final stack of the daily stacks is shown in the graph on the right-hand side for each station. The prior Moho information by Zhao et al. (2015) is indicated by the pink dashed-dotted line and the arrival time of the Moho reflection from the automated method by Becker & Knapmeyer-Endrun (2018) by the blue dashed-dotted line.

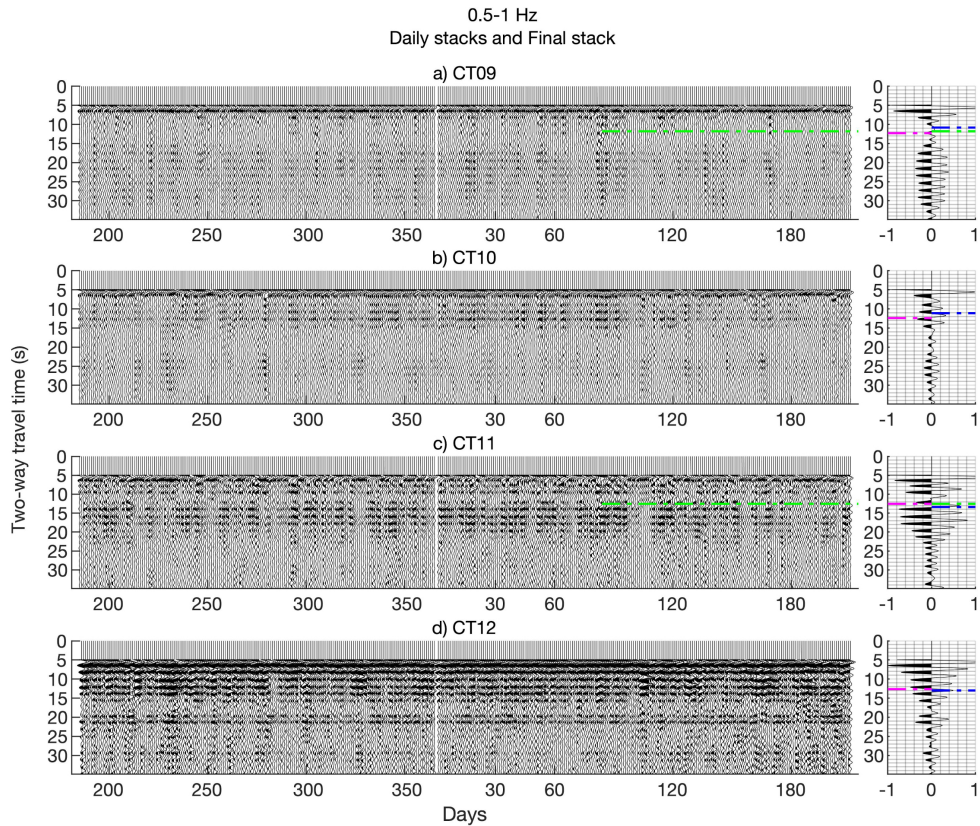


Figure 4.20 The daily autocorrelation stacks for stations (a) CT09, (b) CT10, (c) CT11 and (d) CT12. The final stack of the daily stacks is shown in the graph on the right-hand side for each station. The prior Moho information by Zhao et al. (2015) is indicated by the pink dashed-dotted line and the arrival time of the Moho reflection from the automated method by Becker & Knapmeyer-Endrun (2018) by the blue dashed-dotted line. The arrival time of the Moho reflection from picking the most stable reflection along the daily stacks, green dashed-dotted line, is used for the final reflectivity profile. See Figs 4.28(b) and (c) for better visualization of the stable reflections.

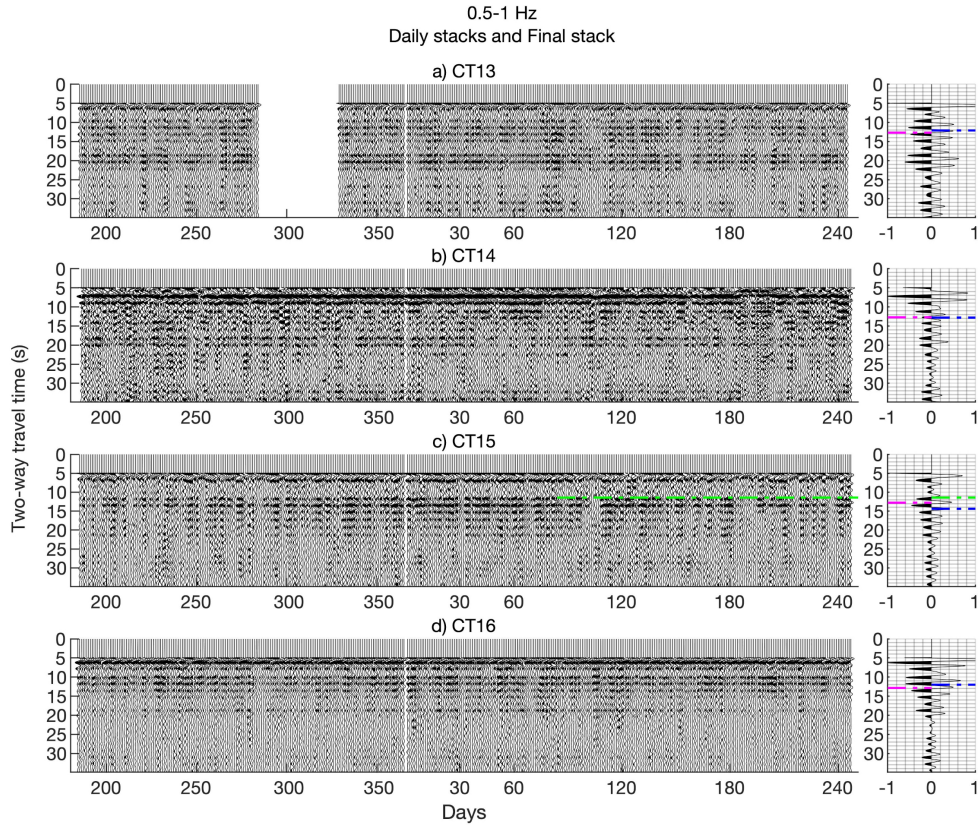


Figure 4.21 The daily autocorrelation stacks for stations (a) CT13, (b) CT14, (c) CT15 and (d) CT16. The final stack of the daily stacks is shown in the graph on the right-hand side for each station. The prior Moho information by Zhao et al. (2015) is indicated by the pink dashed-dotted line and the arrival time of the Moho reflection from the automated method by Becker & Knapmeyer-Endrun (2018) by the blue dashed-dotted line. The arrival time of the Moho reflection from picking the most stable reflection along the daily stacks, green dashed-dotted line, is used for the final reflectivity profile. See Fig. 4.28(d) for better visualization of the stable reflection.

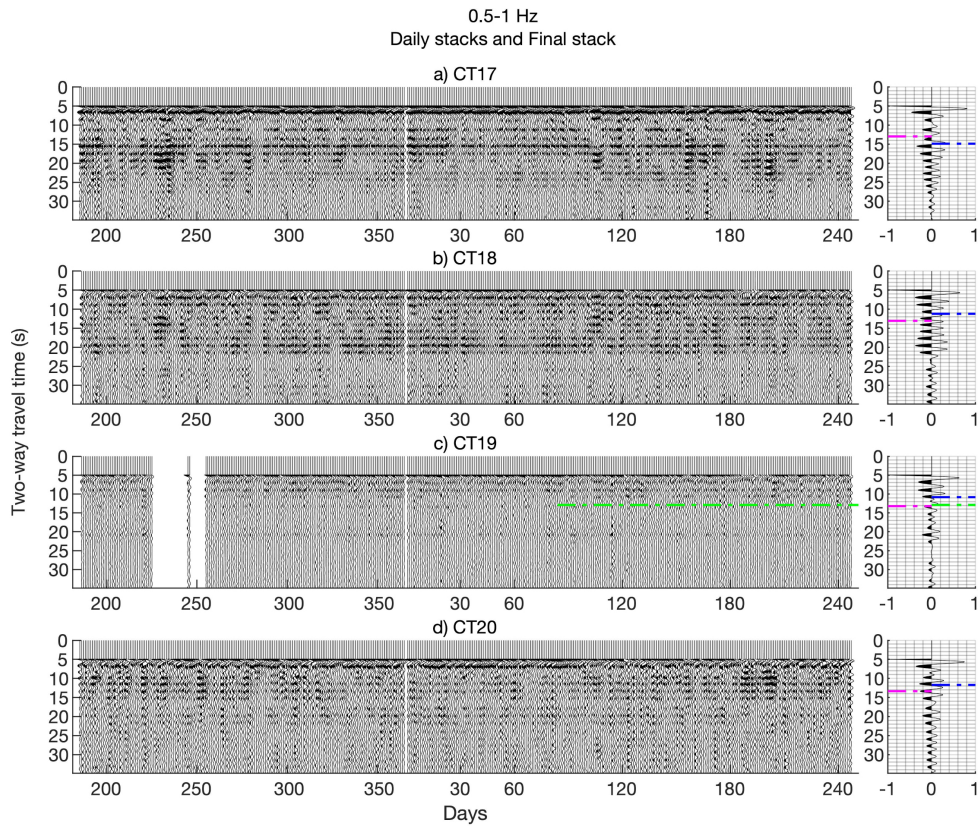


Figure 4.22 The daily autocorrelation stacks for stations (a) CT17, (b) CT18, (c) CT19 and (d) CT20. The final stack of the daily stacks is shown in the graph on the right-hand side for each station. The prior Moho information by Zhao et al. (2015) is indicated by the pink dashed-dotted line and the arrival time of the Moho reflection from the automated method by Becker & Knapmeyer-Endrun (2018) by the blue dashed-dotted line. The arrival time of the Moho reflection from picking the most stable reflection along the daily stacks, green dashed-dotted line, is used for the final reflectivity profile. See Fig. 4.28(e) for better visualization of the stable reflection.

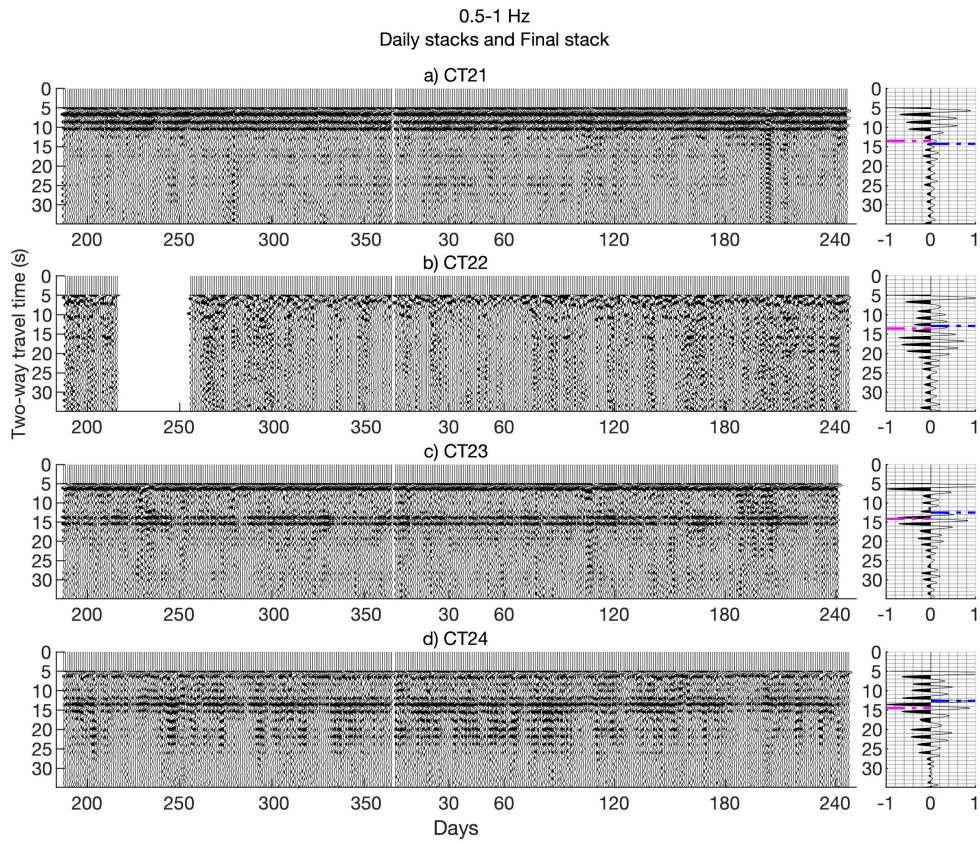


Figure 4.23 The daily autocorrelation stacks for stations (a) CT21, (b) CT22, (c) CT23 and (d) CT24. The final stack of the daily stacks is shown in the graph on the right-hand side for each station. The prior Moho information by Zhao et al. (2015) is indicated by the pink dashed-dotted line and the arrival time of the Moho reflection from the automated method by Becker & Knapmeyer-Endrun (2018) by the blue dashed-dotted line.

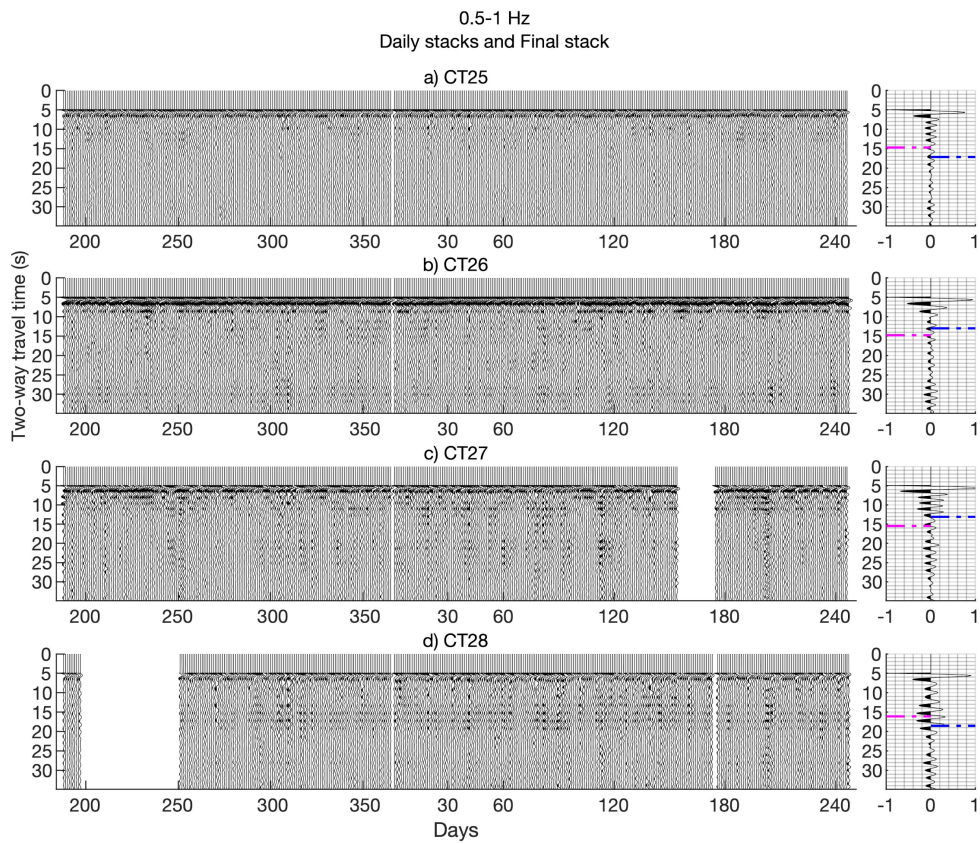


Figure 4.24 The daily autocorrelation stacks for stations (a) CT25, (b) CT26, (c) CT27 and (d) CT28. The final stack of the daily stacks is shown in the graph on the right-hand side for each station. The prior Moho information by Zhao et al. (2015) is indicated by the pink dashed-dotted line and the arrival time of the Moho reflection from the automated method by Becker & Knapmeyer-Endrun (2018) by the blue dashed-dotted line.

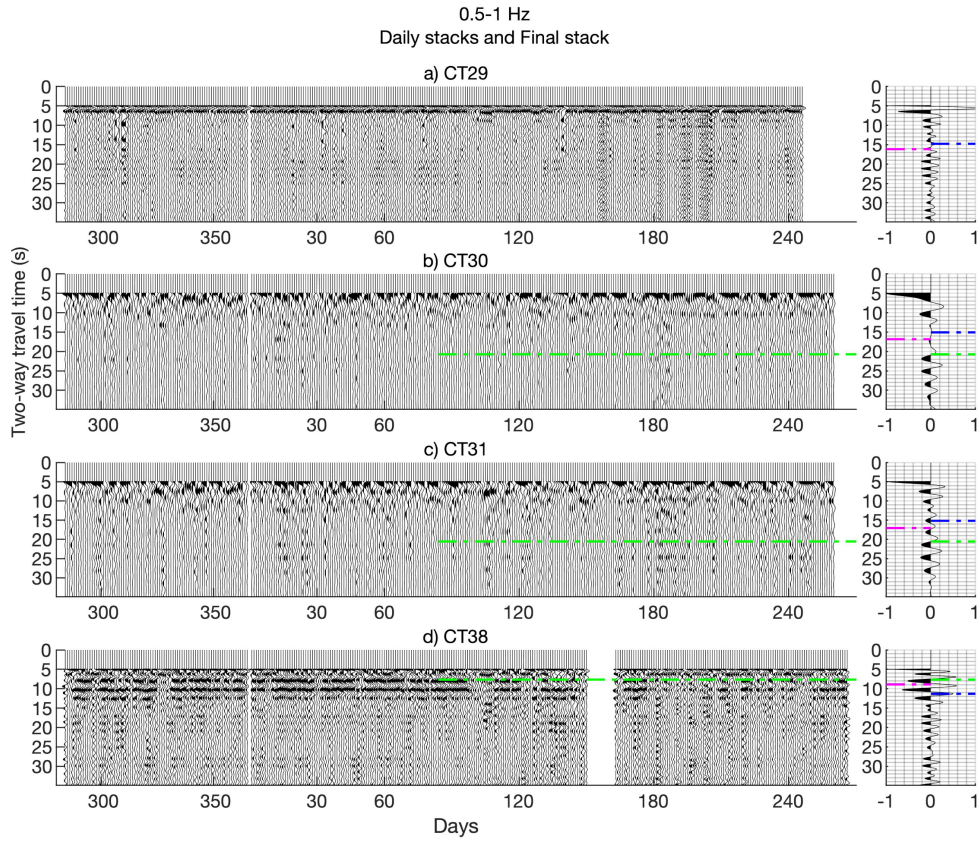


Figure 4.25 The daily autocorrelation stacks for stations (a) CT29, (b) CT30, (c) CT31 and (d) CT38. The final stack of the daily stacks is shown in the graph on the right-hand side for each station. The prior Moho information by Zhao et al. (2015) is indicated by the pink dashed-dotted line and the arrival time of the Moho reflection from the automated method by Becker & Knapmeyer-Endrun (2018) by the blue dashed-dotted line. The arrival time of the Moho reflection from picking the most stable reflection along the daily stacks, green dashed-dotted line, is used for the final reflectivity profile. See Figs 4.29(a)–(c) for better visualization of the stable reflections.

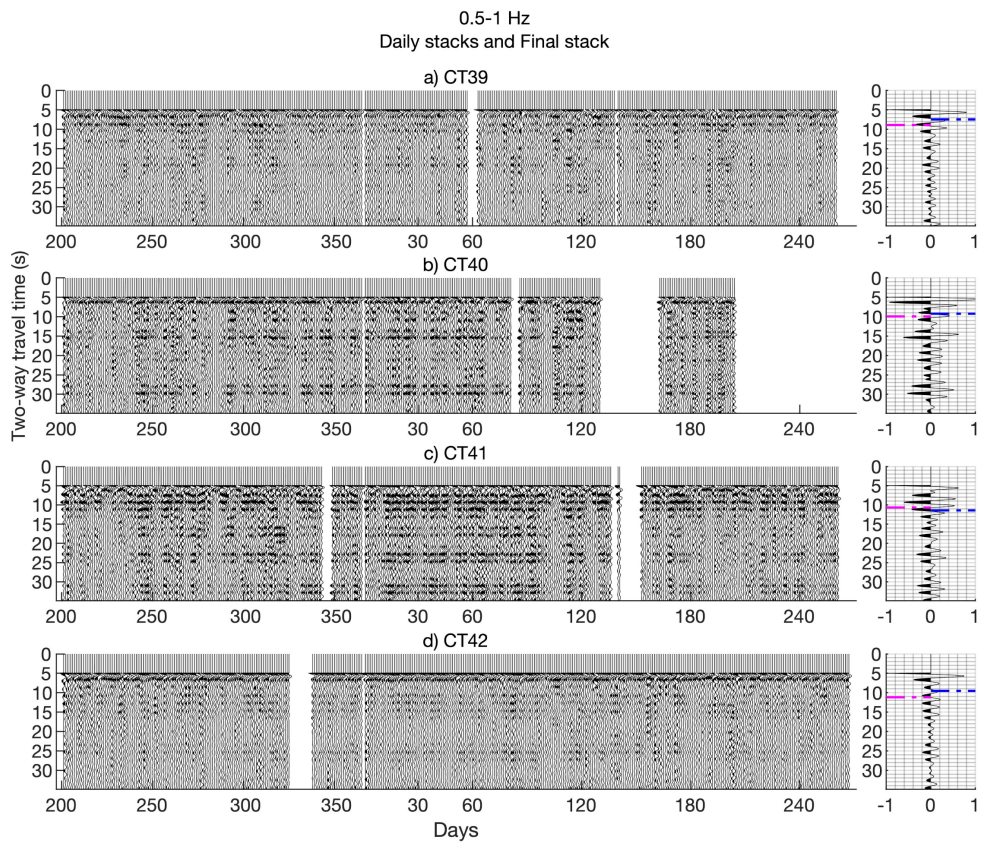


Figure 4.26 The daily autocorrelation stacks for stations (a) CT39, (b) CT40, (c) CT41 and (d) CT42. The final stack of the daily stacks is shown in the graph on the right-hand side for each station. The prior Moho information by Zhao et al. (2015) is indicated by the pink dashed-dotted line and the arrival time of the Moho reflection from the automated method by Becker & Knapmeyer-Endrun (2018) by the blue dashed-dotted line.

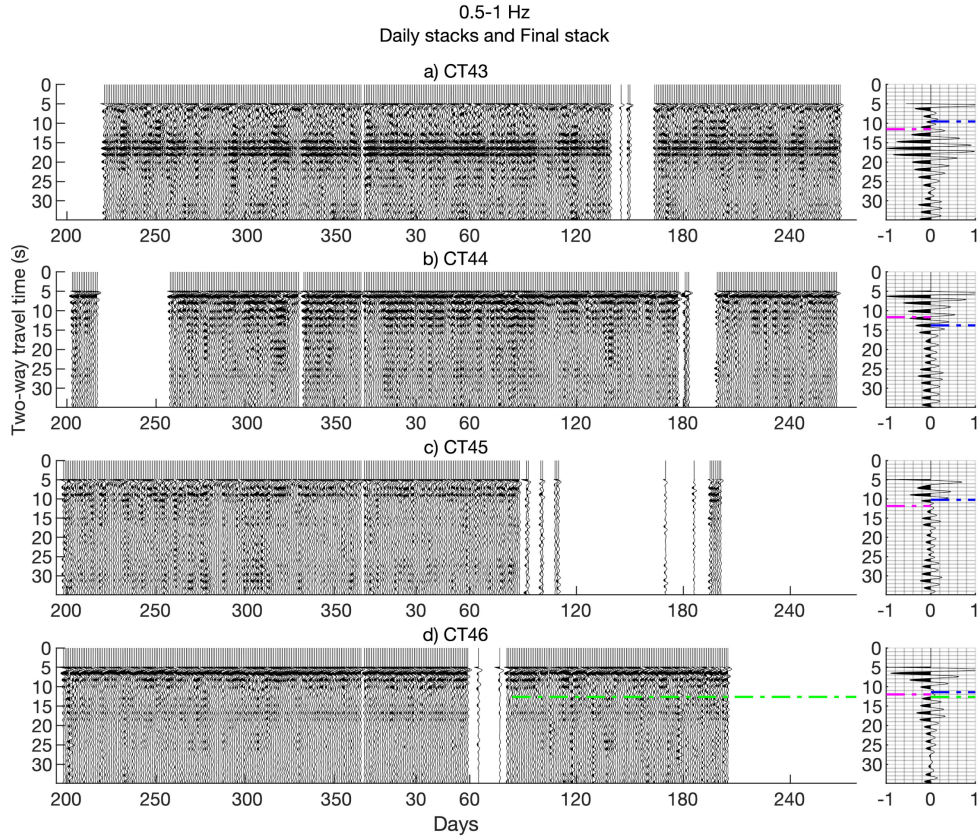


Figure 4.27 The daily autocorrelation stacks for stations (a) CT43, (b) CT44, (c) CT45 and (d) CT46. The final stack of the daily stacks is shown in the graph on the right-hand side for each station. The prior Moho information by Zhao et al. (2015) is indicated by the pink dashed-dotted line and the arrival time of the Moho reflection from the automated method by Becker & Knapmeyer-Endrun (2018) by the blue dashed-dotted line. The arrival time of the Moho reflection from picking the most stable reflection along the daily stacks, green dashed-dotted line, is used for the final reflectivity profile. See Fig. 4.29(d) for better visualization of the stable reflection.

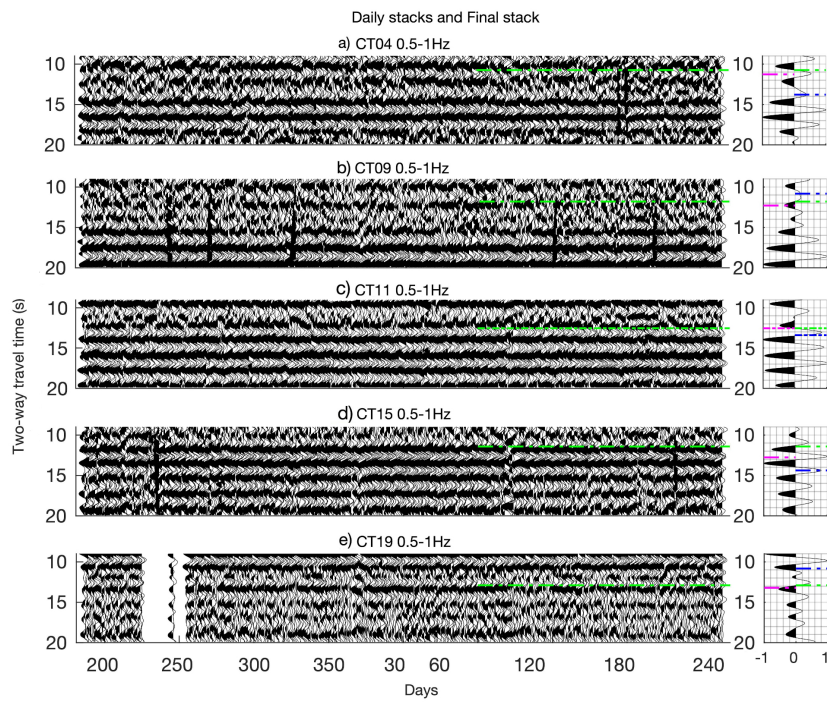


Figure 4.28 The stacks are plotted in shorter normalized time windows for better visualization of the stable reflections along the daily stacks for stations (a) CT04, (b) CT09, (c) CT11 (d) CT15 and (e) CT19.

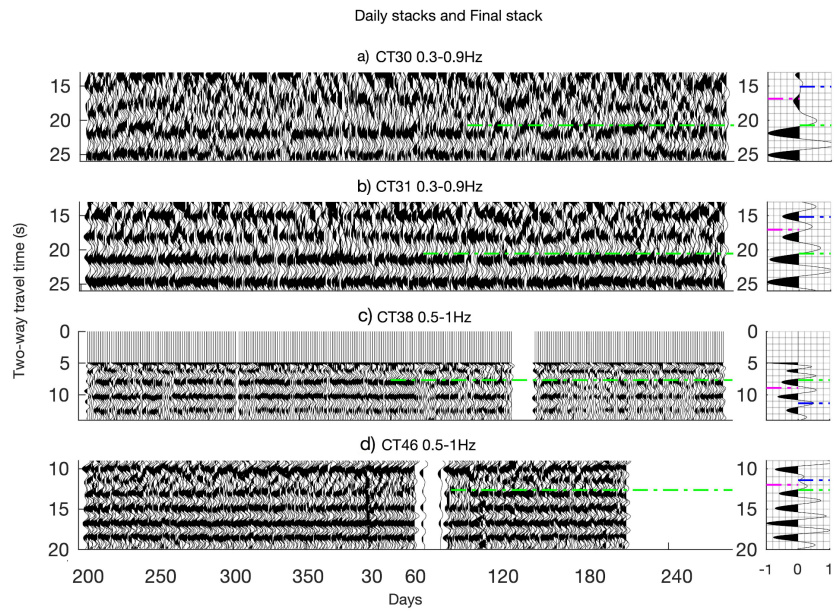


Figure 4.29 The stacks are plotted in shorter normalized time windows for better visualization of the stable reflections along the daily stacks for stations (a) CT30, (b) CT31, (c) CT38 (d) CT46.

Moho structure of the Western Alps from seismic noise autocorrelation of AlpArray data

Summary The lower crustal structure of the Western Alps has been extensively studied through seismology, but its current knowledge leaves significant questions open. We wish to address this topic with another approach, independent from previous determinations in this region, based on single-station analysis of ambient seismic noise, that has been successfully applied elsewhere. We autocorrelate ambient noise on vertical-component seismograms in the 0.4–1 and 0.5–1 Hz frequency bands. We use 175 stations from the AlpArray Seismic Network (AASN). We manually pick the reflectivity changes from the stacked autocorrelations without any use of prior Moho information. We show that the Moho reflections from ambient noise autocorrelations in the Western Alps are related to reflectivity changes. We analyse the final autocorrelation stacks and picked reflectivity changes of stations that are positioned alongside previous geological, *S*-wave velocity and receiver function cross-sections throughout the Western Alps. The depths of the picked reflectivity changes are close to the expected values. In the arc of the Western Alps the depths of the second picked reflectivity changes favour the Moho discontinuity as opposed to the depths of the first picked reflectivity changes that are close to the prior Moho in the European basement and Po Plain. We create two maps of the Moho depths for each frequency band by combining the first and second picked reflectivity changes.

5.1 Introduction

The seismic structure of the crust to upper mantle in the Western Alps has been extensively studied by using active seismic methods (e.g. Grellet et al., 1993; Thouvenot et al., 2007), local earthquake tomography (Diehl et al., 2009), receiver function studies (e.g. Zhao et al., 2015; Paul et al., 2021), seismic anisotropy analysis (Salimbeni et al., 2018), surface wave tomography (e.g. Lu et al., 2018; Kästle et al., 2018), full-wave form inversion (Beller et al., 2018) and trans-dimensional inversion (Zhao et al., 2020). Recent studies (e.g. Paul et al., 2021; Nouibat et al., 2022) show varying structures below the northwestern and southwestern Alps. The continental subduction in the northwestern Alps does not appear as deep as in the southwestern Alps. In addition, the Ivrea body is not as deep in the northwestern Alps as compared to the southwestern Alps.

These seismological studies have used active seismic data, earthquake data or ambient seismic noise data. So far the studies focused on ambient seismic noise (e.g. Lu et al., 2018; Kästle et al., 2018) in the Western Alps, have only created the Green's function between two receivers by cross-correlation. In areas where seismic activity is absent, e.g. passive continental margins, or coverage of the area by seismic receivers is scarce, these seismological techniques are less effective to study crust–mantle structures. In such cases, single station ambient seismic interferometry becomes an important tool to investigate the reflectivity structure underneath each station without the need of controlled sources, earthquake signals or a second receiver. Ashruf & Morelli (2022) were the first in the southwestern Alps to extract the Green's function by using only the ambient seismic noise data of one seismic receiver through autocorrelations.

5.1.1 Moho reflectivity from ambient noise autocorrelation

Detecting the Moho discontinuity from ambient noise autocorrelations has proven to be a challenging task since the Moho reflection is not related to a clear single prominent reflector (e.g. Gorbatov et al., 2013; Ashruf & Morelli, 2022) as commonly seen in receiver function studies (e.g. Zhao et al., 2015; Paul et al., 2021). Here we give an overview of previous studies that obtained the arrival time of the Moho reflection from autocorrelations by using seismic ambient noise of the vertical component seismic record. Ruigrok et al. (2011) identified the Moho reflected *P*-wave from ambient noise autocorrelations by comparison with synthetic reflection responses. This Moho reflection did not correspond to the first stable reflection along the daily stacks or a clear single prominent reflector along the final stack. Ito et al. (2012) created ambient noise autocorrelations in the northeastern Japan subduction zone to detect the Moho by comparison with previous seismic results. Their autocorrelations resulted into stable reflectivities of up to 50 s two-way travel time (TWT). The first stable signals that they detected corresponded to the travel

time of the PP reflection arrival from the continental Moho discontinuity. They assumed the weak detected PmP phases to be due to the Moho forming a transition zone rather than a sharp boundary with a large velocity jump. Tibuleac & von Seggern (2012) assigned the P -wave Moho reflection to the first prominent arrival in the Nevada area. Gorbatov et al. (2013) has created autocorrelograms for stations on the Australian continent for data that not only involved ambient noise but also earthquakes. They chose the deepest prominent reflected phase as the P -wave Moho reflection, that resulted for some areas in deeper and shallower Moho depth than the Moho map of Kennett et al. (2011). In their study they performed synthetic testing, showing that the character of the Moho reflection in ambient noise autocorrelation for a sharp Moho is different than for a gradual Moho discontinuity. The Moho cannot be directly related to the strongest reflection phase when there is a gradual change as opposed to a sharp Moho. In the study by Kennett et al. (2015), the picked Moho reflections in southeastern Australia are not based on a single prominent reflector due to the frequent absence of a distinct reflector. The depth of the Moho reflector was extracted by tracking the base of crustal reflection with the aid of prior Moho and crust–mantle transition information derived from receiver functions or prior reflection profiling. Furthermore, they were the first to obtain Moho depths from spatially stacked autocorrelograms by stacking stations that are within a certain distance of a certain stack point. Kennett (2015) has shown for stations—positioned on top of a strong crust–mantle gradient—in Australia that the Moho discontinuity is related to a fade of crustal reflectivity and afterwards a shift in frequencies. Taylor et al. (2016) used ambient noise autocorrelations to retrieve body wave reflections from the North Anatolian Fault zone. The reflection profiles showed Moho reflected P -waves that were not related to the first prominent reflection along the profiles or reflectivity changes along the stacks. They interpreted the arrival time of the Moho reflection in close correspondence with the theoretical arrival time of the PmP reflection from prior information. Furthermore, they suggested the arrival times of earlier prominent reflectors to reflections from the crystalline basement and mid crustal discontinuity. Oren & Nowack (2016) obtained the Moho reflections in the Nevada and the central U.S. by comparing their autocorrelations with previous Moho reflections from ambient noise autocorrelations and synthetic waveforms. Becker & Knapmeyer-Endrun (2018) picked the arrival times of the Moho reflections in the Trans-European Suture Zone by developing an automated procedure to pick the local maxima inside *a priori* time window of the second derivative envelope. They have used the principle of picking the Moho reflector as the base of the crustal reflector (Kennett et al., 2015) and showed that the local maxima is related to reflectivity changes along the autocorrelation stack. Mroczek & Tilmann (2021) extracted the Moho depth in the Bohemian Massif with the use of prior receiver function information. They relate the Moho reflection to a clear phase rather than a reflectivity change. However, their results show that the

prior Moho information is not only related to a clear phase in the autocorrelation stacks but also to reflectivity changes. Ashruf & Morelli (2022) were able to detect the Moho discontinuity of the subduction zone in the southwestern Alps by using the dense—5–10 km station distance— CIFALPS seismic network (Zhao et al., 2016). They obtained the arrival times of the Moho reflections by using the automatic picking method by Becker & Knapmeyer-Endrun (2018). Despite the numerous works, there is still no clear trend to be found to detect the Moho reflected *P*-waves without prior crust–mantle information. This demonstrates the need for further analysis of the autocorrelation stacks to fully realize ambient seismic noise autocorrelations as a reliable method independent of previous studies.

5.1.2 Research aim and overview

Extracting the Moho discontinuity from ambient seismic noise autocorrelations independently of prior information favours areas where there is no prior information or areas, e.g. subduction zones, that have controversial results. To investigate the structural differences in the Western Alps and how they can be identified from ambient noise autocorrelation, we use stations from the broad AlpArray Seismic Network (AASN) (AlpArray Seismic Network, 2015). Our aim is to associate reflectivity changes along the final stacks to the Moho discontinuity without the use of prior information. We analyse the autocorrelation stacks and independently picked reflectivity changes alongside previous cross-sections throughout the Western Alps. We select the reflectivity changes that might be associated to the Moho discontinuity. We do not focus on the processing part or how to improve the body wave reflections through processing steps.

5.2 Data and Method

5.2.1 AlpArray Seismic Network

We use the ambient seismic noise data recorded by the AlpArray Seismic Network, AASN (AlpArray Seismic Network, 2015), that is composed of 628 seismic stations across the greater Alpine region (Hetényi et al., 2018). We only use a total of 175 broadband stations, 81 permanent and 94 temporary, since our focus lies in the Western Alps. The permanent stations of the AASN belong to the following networks with codes: 8D (Swiss Seismological Service (SED) At ETH Zurich, 2005), C4 (CERN, 2016), CH (Swiss Seismological Service (SED) At ETH Zurich, 1983), GU (University of Genoa, 1967), IV (INGV Seismological Data Centre, 1997) and MN (MedNet Project Partner Institutions, 1988). The temporary stations are all part of the AASN and belong to the Z3 network code (AlpArray Seismic Network, 2015). The seismic stations have a hexagonal deployment with an inter-station distance of 52 km and an operation time between 2015 and 2022 (see station map

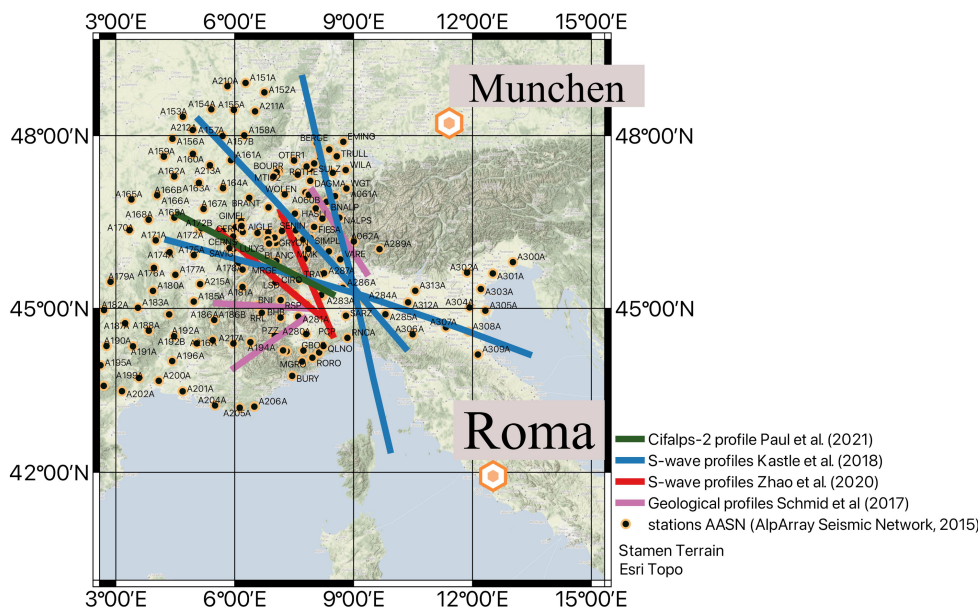


Figure 5.1 Map of the AASN stations used in this work, marked by circles, and lines of the profiles used for analysis of the autocorrelation stacks and reflectivity changes in Figs 5.10–5.12. The thick coloured lines mark the locations of the 9 profiles used for analysis throughout the Western Alps. The legend at the bottom right-hand side describes to which study the profiles belong. We used Stamen Terrain and Esri Topo in QGIS (QGIS Development Team, 2022) to create the map.

in Fig. 5.1). The seismic waveform data of the vertical channels (HHZ) have sampling rates varying between 50 and 250 Hz. In this work, we only use the vertical components since our focus lies on the reflected P -wave energy that is expected to travel with vertical incidence. We use the term reflectivity for the reflected P -wave energy traveling at vertical incidence. See table B.1 in Appendix A for information of the stations used.

5.2.2 Ambient noise autocorrelation

We process raw data using ObsPy (Krischer et al., 2015) in a pre-processing stage of the ambient seismic noise data, where we start by subtracting the mean and trend before tapering the ends with a Hanning window width of 0.01. Afterwards, we decimate the data from $f_s = 100$ Hz to $f_s = 20$ Hz. We remove the instrument response over the following trapezoidal frequency range of $f_1 = 0.01$ Hz, $f_2 = 0.02$ Hz, $f_3 = 5$ Hz, $f_4 = 10$ Hz to obtain displacement (nm). We finish the first processing stage with a further decimation from $f_s = 20$ Hz to $f_s = 8$ Hz. Decimation has been performed to increase the processing speed, while taking into consideration that the

highest cut-off frequency, 1 Hz, is well below the Nyquist frequency of 4 Hz.

After such preparation, we further process the data with Matlab. The second processing stage starts with filtering of the data by using a zero-phase two-pole Butterworth bandpass filter in the [0.4–1] and [0.5–1] frequency bands (in Hertz). After applying the bandpass filter, we cut the time series into 1-hr time intervals to autocorrelate. In case of an earthquake, waveforms are dominated by high-amplitude wave packets. Bensen et al. (2007) showed that the effect of earthquakes and non-stationary sources close to the stations can effectively be removed by applying a time-domain, or temporal, normalization. Therefore, we also apply such sign-bit normalization that only retains information on zero-crossings in the time domain and obliterates amplitude information. Afterwards, we autocorrelate 1-hr data slices, and then linearly stack them. For the stacking, we have used between 3 months and 2 years of data depending on the quality of the data. Spikes related to instrumental problems have been excluded. Ashruf & Morelli (2022) has shown that for temporal stacking in the [0.4–1] and [0.5–1] frequency bands, 1 month of data is enough to reach a stable correlation between the stacked autocorrelations and the final stack.

The Western Alps is a complex area resulting in a wide variety of seismic velocities (Malusà et al., 2021), so we use for the time to depth conversion the EU60 model of Zhu & Tromp (2013).

5.2.3 Reflectivity changes related to the Moho reflection

In this work we pick reflectivity changes that are based on amplitude and frequency changes along the autocorrelation stack. In the study by Ashruf & Morelli (2022) the best results have been obtained for the 0.5–1 Hz frequency band. We here use the same frequency band and also the 0.4–1 Hz band to analyse the reflectivity changes in two different frequency ranges. We use vertical components, so the P -wave reflectivity beneath the stations are computed. Fig. 5.2 is an example of how we pick the reflectivity changes (highlighted by the horizontal green lines) in the 0.4–1 and 0.5–1 Hz frequency bands. Analysis and comparison of daily stacks allow to check the persistence of stable features, that also appear in the final global linear stack, also shown in the figure. The picked reflectivity changes in Fig. 5.2 are based on changes in the amplitude along the final stack that coincide with a stable reflection along the daily stacks. In both frequency bands the first and second reflectivity change are related to a decrease and increase in amplitude along the final stacks, respectively. To prevent that the picks are biased we do not pick the reflectivity changes inside *a priori* time window that is based on Moho information from previous studies.

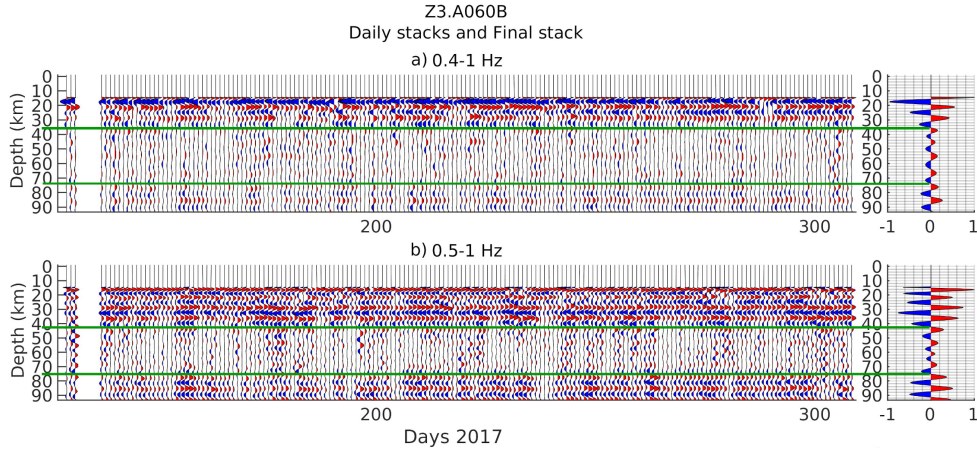


Figure 5.2 The daily autocorrelation stacks of station A060B in the (a) 0.4–1 Hz and (b) 0.5–1 Hz frequency bands. The final stacks of the daily stacks in each frequency band are shown in the graph on the right-hand side. The green horizontal lines mark the clear reflectivity changes detected along the final stacks that coincide with stable reflections along the daily stacks. The positive and negative amplitude lobes are filled with the red and blue colour, respectively.

5.3 Results

We present the depths of the picked reflectivity changes in the [0.4–1] and [0.5–1] Hz frequency bands. We analyse the picked reflectivity changes throughout the Western Alps together with the Moho map by Spada et al. (2013). Afterwards, we plot final autocorrelation stacks of stations that are close to the cross-sections of Fig. 5.1 to analyse the picked reflectivity changes alongside previously inferred crustal structures. In addition, we analyse 4 stations that are positioned in the same geological region to find a relation between the geological unit and picked reflectivity changes. To avoid the dominance of the large pulses at and after 0 s, we muted the stacks up to 5 s two-way traveltime (TWT). For better analysis of the results we migrate the muted autocorrelation stacks to depth.

5.3.1 Picked reflectivity changes

Fig. 5.3 shows the depths of the picked reflectivity changes in coloured circles, of the stations of the AASN network (Fig. 5.1) in the Western Alps, for the 0.4–1 and 0.5–1 Hz frequency bands. The depths of the reflectivity changes are superimposed on the Moho depth map by Spada et al. (2013) and follow the same colouring scale. The black circles in the plots of the first picked reflectivity changes, Figs 5.3(a) and (c), are the stations with no detected reflectivity change due to poor quality

data that might be related to instrumental problems or lack of stable reflections throughout the daily stacks. Despite the small difference, between the low-pass corners of the 0.4–1 and 0.5–1 Hz frequency bands, there are some stations that show significant differences between the depths of the picked reflectivity changes of the different frequency bands.

The first picked reflectivity changes in the 0.5–1 Hz band, Fig. 5.3(c), of the stations situated on the basement of the European plate— 3° – 6° E— are closer aligned to the prior Moho depth map as opposed to results of the 0.4–1 Hz band, Fig. 5.3(a), that result mostly deeper in this area. These deeper results may be due to the fact that the longer wavelengths of the 0.4–1 Hz band have a limited vertical resolution and are not able to resolve shallower discontinuities. In the mountain region of the Western Alps, 6° – 9° E, the first picked reflectivity changes for both frequency bands are mostly shallower than the reference Moho. This may be due to the complex structure of the subduction zone and the picked reflectivity change being associated to mid-crustal discontinuities. The stations situated in the Po Plain, 9° – 13° E, show few correspondence with the prior Moho, in both frequency bands the first picked reflectivity changes are mostly shallower.

The plots of the second picked reflectivity changes for the 0.4–1 Hz, Fig. 5.3(b), and 0.5–1 Hz, Fig. 5.3(d), frequency bands, show a significant amount of stations with no detected reflectivity changes, black circles. This is due to a lack of stable reflections along the daily stacks that coincide with clear reflectivity changes along the final stack. The second picked reflectivity changes of the stations situated in the European basement show generally a greater depth than the prior Moho by Spada et al. (2013) for both frequency bands. In the mountain region of the Western Alps and the Po Plain the second picked reflectivity changes are for both frequency bands in close correspondence with the prior Moho as opposed to the first picked reflectivity changes that result mostly shallower. This may suggest that the first picked reflectivity changes in these areas are related to shallow mid-crustal discontinuities. The second picked reflectivity changes in the 0.4–1 Hz band show for a few stations a deeper depth than the prior Moho, which may be related to the limited vertical resolution.

The results of Fig. 5.3 show a general trend that the first picked reflectivity changes of the stations positioned in the European basement are more aligned to the prior Moho and for the other regions where the prior Moho is deeper the depth of the second picked reflectivity changes result in close correspondence with the prior Moho depth.

5.3.2 P-wave reflectivity Western Alps

To investigate the depths of the picked reflectivity changes further we plot the autocorrelation stacks with prior profiles throughout the Western Alps. In Figs 5.4–

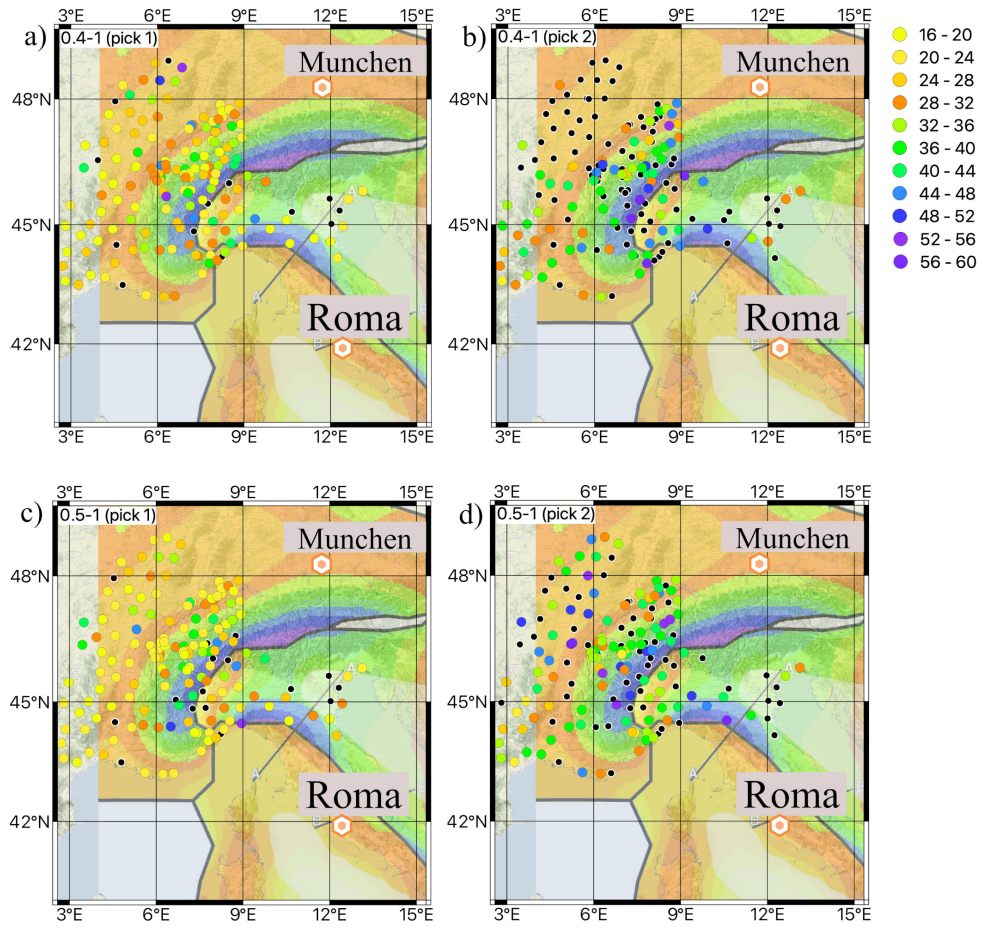


Figure 5.3 The depth (km) of the picked reflectivity changes are plotted on top of the Moho depth map by Spada et al. (2013). The depth of the first picked reflectivity changes in the (a) 0.4–1 Hz and (c) 0.5–1 Hz frequency bands. The depth of the second picked reflectivity changes in the (b) 0.4–1 Hz and (d) 0.5–1 Hz frequency bands. The colour scale is shown on the right-hand side and follows the same scale as used by Spada et al. (2013). The black circles denote the autocorrelation stacks with no detected reflectivity change. These maps were created by using QGIS (QGIS Development Team, 2022).

5.12 we show the final autocorrelation stacks along 9 profiles that run throughout the Western Alps, Fig. 5.1. The profiles are divided into 1 receiver function CCP migrated section of Paul et al. (2021), 3 *S*-wave profiles by Kästle et al. (2018), 2 *S*-wave profiles by Malusà et al. (2021) from the results of Zhao et al. (2020) and 3 geological profiles by Schmid et al. (2017).

Cifalps-2

In Fig. 5.4 we compare autocorrelation stacks filtered in the 0.4–1 and 0.5–1 Hz bands with the receiver function CCP migrated section of Paul et al. (2021) to analyse the detected reflectivity changes with the behavior of the receiver functions. Station A172A shows for the second picked reflectivity change at around 25 km—a clear increase in amplitude—in the 0.4–1 Hz band, Fig. 5.4(c), that coincides with the top of the most prominent Ps/P amplitude. In the 0.5–1 Hz band, Fig. 5.4(d), the second reflectivity change is much deeper at ~ 60 km, which is noticeably at the top of the only positive Ps/P reflection at this depth. The top of this increased amplitude Ps/P arrival corresponds also to a clear reflectivity change, amplitude decrease, in the 0.4–1 Hz band. This shows the ability of reflectivity changes from ambient noise autocorrelations to not only retrieve discontinuities from crustal structures but also from upper mantle structures. Stations A172A and A172B are very close to each other, ~ 5 km, showing coherence between the reflectivity phases in both frequency bands. This coherence results also in the picked reflectivity changes being at the same depths. Stations MRGE and REMY are also very close— ~ 10 km—to each other with coherence between the reflectivity phases, resulting in equal depths of the reflectivity changes.

The first picked reflectivity change for station A169A corresponds in both the 0.4–1 and 0.5–1 Hz frequency bands to the top of the most prominent amplitude of the Ps/P arrival. For station REMY, the second picked reflectivity change at around 45 km, clear decrease in amplitude, filtered in the 0.5–1 Hz band coincides with the bottom of the prominent amplitude of the Ps/P arrival. The second picked reflectivity change in the 0.4–1 Hz band of station CIRO corresponds to the bottom of positive Ps/P arrival that likely coincides with the subducting European plate. For the same station the first picked reflectivity change in the 0.5–1 Hz band corresponds to the top of the Ps/P arrival. This shows the strong differences between frequency bands and the picked reflectivity changes in relation to the most prominent amplitude of the Ps/P arrival that is being interpreted as the Moho discontinuity. The second picked reflectivity changes of stations TRAV and A283B in the 0.5–1 Hz band corresponds to the top of the most prominent amplitude of the Ps/P arrival. For station A283B the depth of the second picked reflectivity change in the 0.4–1 Hz band corresponds also to the top of the most prominent amplitude of the Ps/P arrival.

The results show the difficulty of assigning reflectivity changes along the ambient

noise autocorrelation to specific discontinuities without the use of prior information of the crust–mantle structures.

***V_s*-profiles**

Fig. 5.5 shows the *S*-wave velocity structure along profile B by Kästle et al. (2018) across the Western Alps. The autocorrelation stacks are plotted on top of the *V_s* profile for the 0.4–1 and 0.5–1 Hz bands, Figs 5.5(c) and (d), respectively. Stations A287A and A283B are very close to each other, ~ 43 km, resulting in coherent crustal reflection phases. The first and second reflectivity changes are for both stations related to a decrease and increase in amplitude, respectively. Even though the coherent crustal reflections, the depth of reflectivity changes for station A283B are shallower than of station A287A for both frequency bands. Coherence between reflectivity phases and depth of the reflectivity changes can be detected between the stations A171A and A174A— ~ 35 km inter-station distance— with only slight deepening of the second picked reflectivity changes.

The stations—LSD and TRAV— that are positioned near the subduction zone with inter-station distance ~ 48 km show large differences between the stacks filtered in the 0.4–1 and 0.5–1 Hz bands. These differences might be due to the complex structure of the subducting European plate underneath the Adriatic plate. Only station A284A results into a very clear phase closely to the prior Moho, white dashed line, by Spada et al. (2013).

In the 0.4–1 Hz band, Fig. 5.5(c), the depth of the second picked reflectivity change of station A171A matches the *V_s* contrast by Kästle et al. (2018) related to the Moho discontinuity. In this area the prior Moho depth by Spada et al. (2013), white dashed line, is situated shallower than the results by Kästle et al. (2018). The depths of the first picked reflectivity change of station A175A and second picked reflectivity change of station A178A also matches the *V_s* contrast by Kästle et al. (2018) associated to the Moho discontinuity. The depths of the first picked reflectivity changes of stations A283B and A285A closely matches the prior Moho discontinuity by Spada et al. (2013).

In the 0.5–1 Hz band, Fig. 5.5(d), the depth of the second picked reflectivity changes of stations A287A and A283B closely matches the *V_s* contrast by Kästle et al. (2018) related to the Moho discontinuity as opposed to the prior Moho depth by Spada et al. (2013) that is shallower. The depths of the first picked reflectivity change of station A283B and second picked reflectivity change of station A285A closely matches the prior Moho depth by Spada et al. (2013). The second picked reflectivity change by station A312A is related to an increase in wave frequency. The depth of the pick closely matches the prior Moho discontinuity by Kästle et al. (2018) that is slightly shallower than the prior Moho depth by Spada et al. (2013).

The *S*-wave velocity structure along profile C by Kästle et al. (2018) is shown in Fig. 5.6 with the autocorrelation stacks. Fig. 5.6(c) shows the autocorrelation

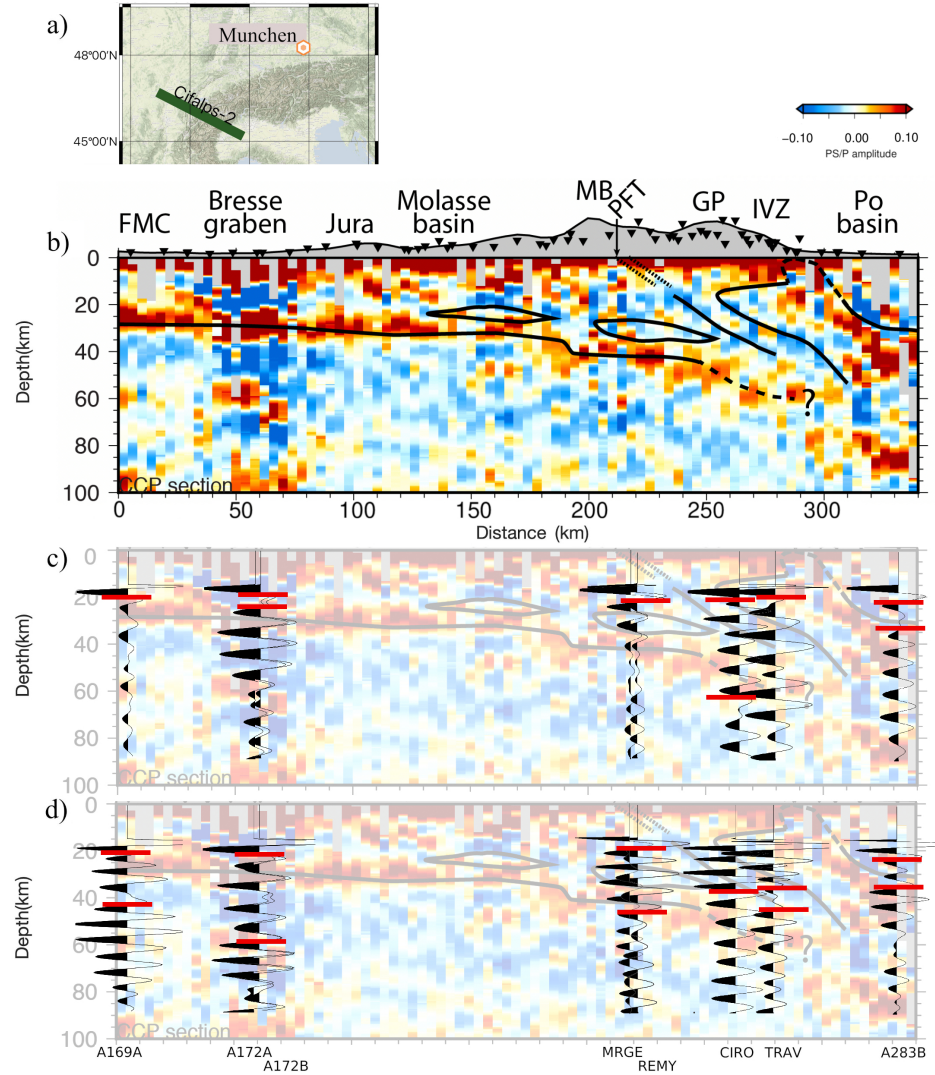


Figure 5.4 (a) The map shows the location, green line, of the CIFALPS-2 profile in the Western Alps region (b) receiver function CCP migrated section for teleseismic earthquakes of 0-100° backazimuth from Paul et al. (2021), (c) autocorrelation stacks of the AASN network stations along the CIFALPS-2 network plotted on top of the RF profile of Paul et al. (2021). The autocorrelation stacks are filtered in the (c) 0.4-1 Hz and (d) 0.5-1 Hz frequency bands. The short red horizontal lines mark the picked reflectivity changes along the autocorrelation stacks. FMC marks the French Massif Central area. MB, Mont Blanc; PFT, Penninic frontal thrust; GP, Gran Paradiso; IVZ, Ivrea-Verbano zone.

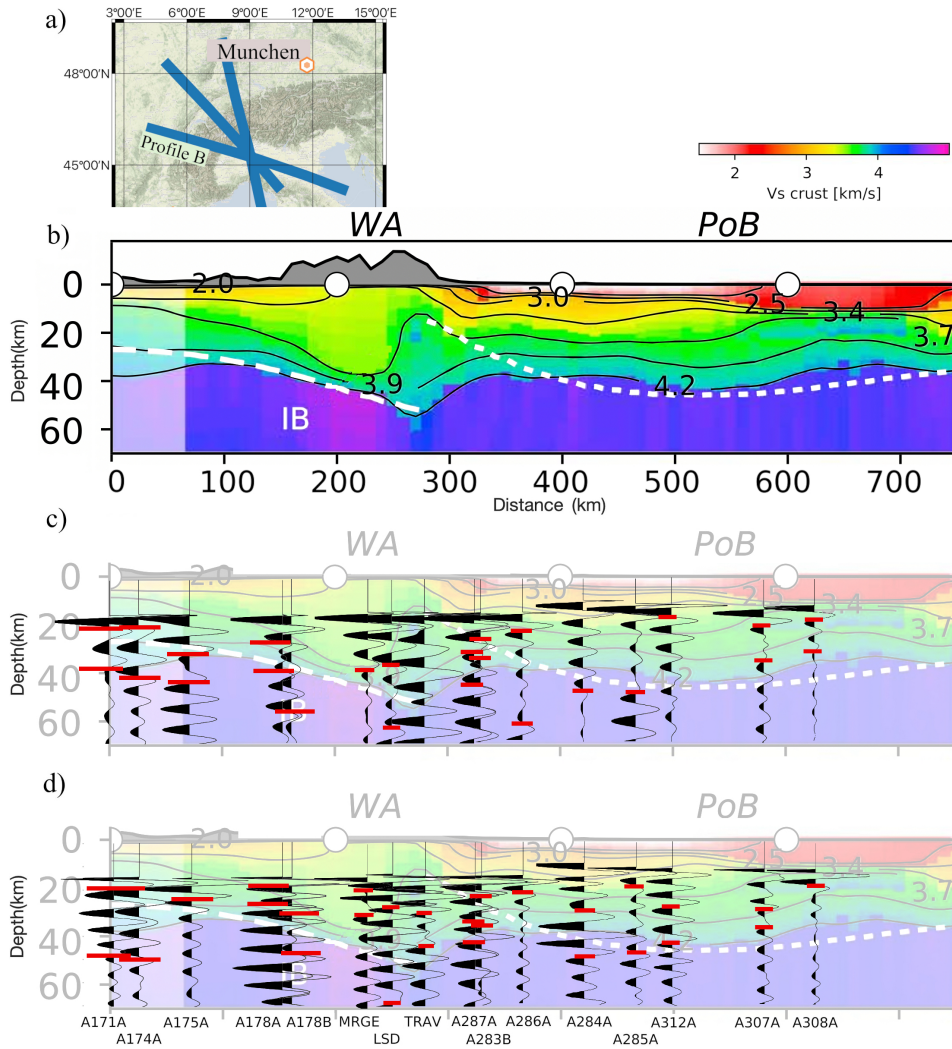


Figure 5.5 (a) The map shows the locations, blue lines, of profile B and two other S-wave profiles by Kästle et al. (2018) in the Western Alps. (b) Shear wave velocity structure along the B profile crustal section. The final autocorrelation stacks of the AASN network stations along profile B are plotted on top of the Vs profile of Kästle et al. (2018) filtered in the (c) 0.4–1 Hz and (d) 0.5–1 Hz frequency bands. The short red horizontal lines mark the reflectivity changes detected on the autocorrelation stacks. Moho boundary lines (white color) in the cross sections for European and Adriatic Plate are taken from the receiver function and CSS study of Spada et al. (2013). IB marks the position of the Ivrea body. WA, Western Alps; PoB, Po Molasse Basin.

stacks filtered in the 0.4–1 Hz band. In this passband the depth of the first picked reflectivity changes of station BRANT closely matches the prior Moho by Spada et al. (2013). The depths of the first picked reflectivity changes of stations A161A and JAUN closely matches the V_s contrast between the crust and mantle by Kästle et al. (2018). The depths of the second picked reflectivity changes of stations A153A and A287A closely matches the V_s contrast between the crust and mantle by Kästle et al. (2018). The depth of the second picked reflectivity change of station EMBD matches both the prior Moho depth by Spada et al. (2013) and Kästle et al. (2018). The depth of the second picked reflectivity change of station A285A closely matches the prior Moho depth by Spada et al. (2013).

In the 0.5–1 Hz band, Fig. 5.6(d), the depths of the first picked reflectivity changes of stations A157B and JAUN closely matches the V_s contrast between the crust and mantle by Kästle et al. (2018). The depths of the second picked reflectivity changes of stations A153A and A287A closely matches the V_s contrast between the crust and mantle by Kästle et al. (2018). The depth of the first picked reflectivity change of station BRANT matches both the prior Moho depth by Spada et al. (2013) and Kästle et al. (2018). The depths of the picked reflectivity changes of stations; A212A, A161A, BRANT, JAUN and A285A matches the prior Moho depth by Spada et al. (2013). Most of the first picked reflectivity changes of the stations that are situated on the Po Plain—PoB in Fig. 5.6— are situated at much shallower depths than the prior Moho depths. These shallow picked reflectivity changes may be related to mid-crustal discontinuities. The first picked reflectivity changes of the stations that are positioned between 0 and 200 km distance of the profile mainly matches the prior Moho depths.

The S -wave velocity structure along profile D by Kästle et al. (2018) is shown in Fig. 5.7 with the autocorrelation stacks. The depths of the first reflectivity picks in the 0.4–1 Hz band, Fig. 5.7(c), of stations ZUR and FUSIO closely matches the crust–mantle V_s contrast by Kästle et al. (2018). For stations A060B and VARE in the 0.4–1 Hz band the depths of the first picked reflectivity changes matches the prior Moho depth by Spada et al. (2013). The depths of the second picked reflectivity changes of the stations; MUO, GRIMS, FUSIO, SARZ and RNCA in the 0.4–1 Hz band closely matches the prior crust–mantle depths by Spada et al. (2013) and Kästle et al. (2018). These stations are positioned in the subduction zones—European Plate subducting under the Adriatic Plate and Adriatic Plate under the Liguro-Provençal-Tyrrhenian Domain (LPTD)—. The depths of the second picked reflectivity changes in the 0.4–1 Hz band for the remaining stations along the profile are all positioned outside of the subduction zones, where the prior Moho—European basement and Po Plain— results mostly flat. Station RNCA is positioned on top of a subduction zone where the depth of the first picked reflectivity change is related to the prior Moho of the LPTD and the depth of the second picked reflectivity change the prior Moho of the Adriatic Plate.

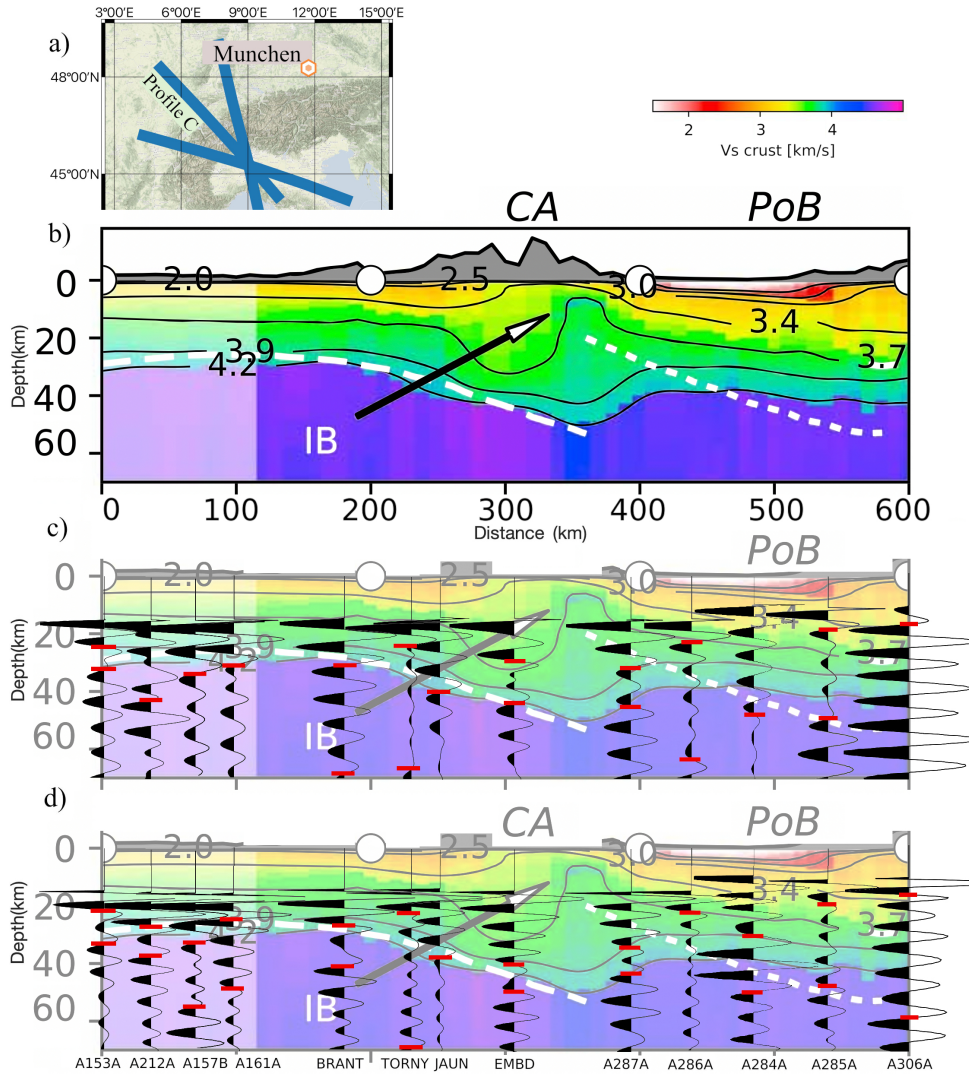


Figure 5.6 (a) The map shows the locations, blue lines, of profile C and two other S-wave profiles by Kästle *et al.* (2018) in the Western Alps. (b) Shear velocity structure along the C profile crustal section. The final autocorrelation stacks of the AASN network stations along profile C are plotted on top of the V_s profile of Kästle *et al.* (2018) filtered in the (c) 0.4–1 Hz and (d) 0.5–1 Hz frequency bands. The short red horizontal lines mark the picked reflectivity changes along the autocorrelation stacks. Moho boundary lines (white color) in the cross sections for European and Adriatic Plate are taken from the receiver function and CSS study of Spada *et al.* (2013). CA marks the Central Alps area. PoB, Po Molasse Basin.

In the 0.5–1 Hz band, Fig. 5.7(d), the depths of the picked reflectivity changes of stations ZUR, A060B, FUSIO, VARE and SARZ corresponds to the crust–mantle V_s contrast by Kästle et al. (2018). The depths of the picked reflectivity changes of stations BERGE, MUO, GRIMS and RNCA corresponds to the crust–mantle boundary by Spada et al. (2013). Station FUSIO has in this frequency band 2 picked reflectivity changes as opposed to only 1 in the 0.4–1 Hz band. The station is positioned on top of the subduction zone where the depth of the first picked reflectivity change closely matches the prior Moho of the Adriatic Plate by Spada et al. (2013). In addition, the depth of the second picked reflectivity change matches the crust–mantle V_s contrast by Kästle et al. (2018) of the European Plate.

Fig. 5.8 shows the autocorrelation stacks of the stations along the ECORS-CROP V_s profile by Malusà et al. (2021) based on TransD inversion of Rayleigh wave group velocity dispersion data by Zhao et al. (2020). The depths of the first picked reflectivity changes in the 0.4–1 Hz band, Fig. 5.8(c), for stations A214A and LULY3 closely matches the prior crust–mantle boundary depth indicated by the white dotted line. The depth of the second picked reflectivity change of station RSP that is situated on top of the subducting European plate matches the prior Moho depth. The stations; PERON, A187A and LSD have picked reflectivity changes that matches closely to the prior Moho discontinuity by Zhao et al. (2020).

In the 0.5–1 Hz band, Fig. 5.8(d), the depths of the picked reflectivity changes at the beginning of the profile— 0 to 75 km distance— are mostly shallower than the depths of the picked reflectivity changes in the 0.4–1 Hz band. The 0.4–1 Hz band has a limited vertical resolution due to the longer wavelengths Yilmaz (2001), which makes it easier for the shorter wavelengths in the 0.5–1 Hz band to detect shallower discontinuities. The depths of the picked reflectivity changes of the stations; PERON, LULY3, SALEV, A187B and MONC closely matches the prior Moho depths.

Fig. 5.9 shows the autocorrelation stacks of the stations along the NFP-20 West V_s profile by Malusà et al. (2021) based on TransD inversion of Rayleigh wave group velocity dispersion data by Zhao et al. (2020). In the 0.4–1 Hz band, Fig. 5.9(c), the depth of the first picked reflectivity change of station A283B closely matches the prior Moho depth. The depth of the second picked reflectivity change do not match the prior Moho depth. The depth of picked reflectivity changes of stations; TORNY, JAUN, A283B and PCP that do not match to the prior crust–mantle boundary, does correspond to the V_s jump of 4.0 to 4.5 km s⁻¹.

In the 0.5–1 Hz band, Fig. 5.9(d), the depth of the second picked reflectivity changes of stations; SENIN, SATI, TRAV and PCP, closely matches the prior crust–mantle V_s boundary. The picked reflectivity changes of stations; TORNY, JAUN, A283B and ROTM matches the V_s jump of 4.0 to 4.5 km s⁻¹. These close matches demonstrate the ability of the shorter wavelengths in the 0.5–1 Hz band to better

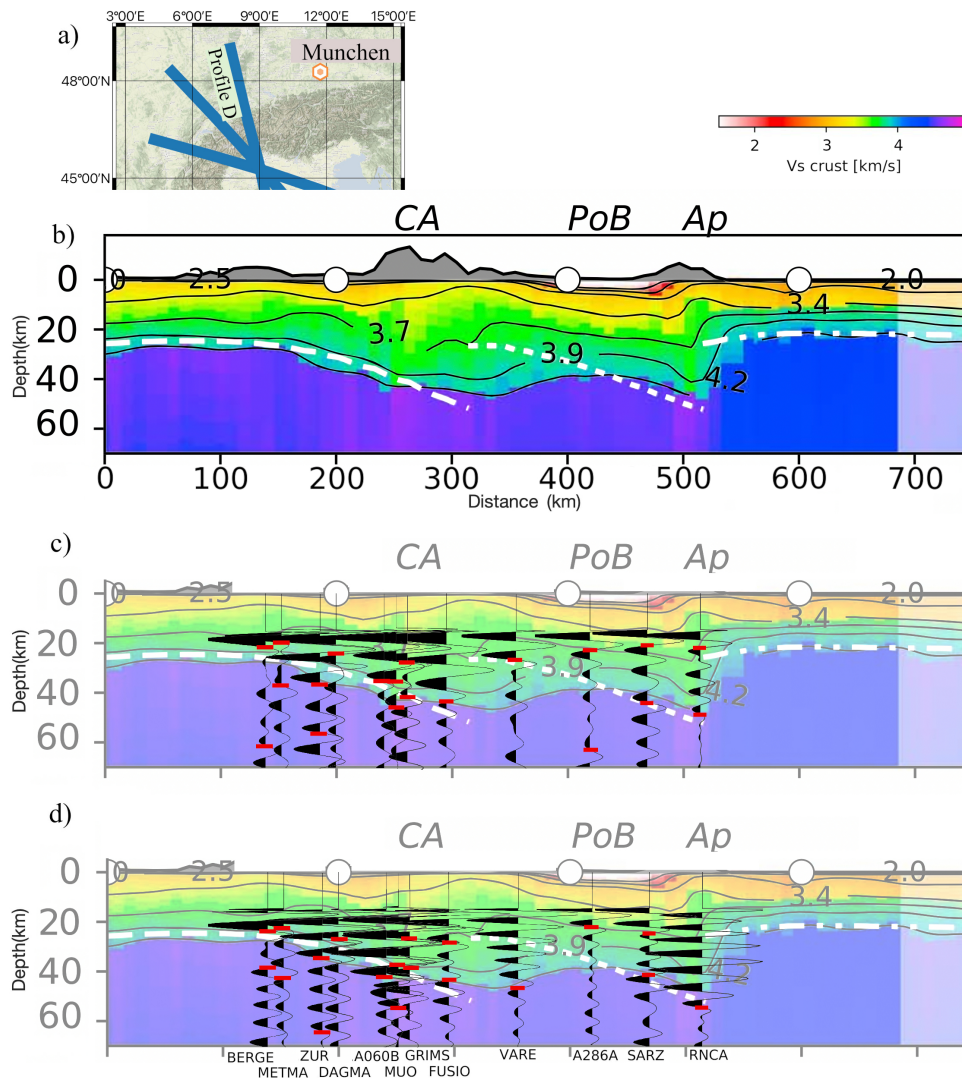


Figure 5.7 (a) The map shows the locations, blue lines, of profile D and two other S-wave profiles by Kästle et al. (2018) in the Western Alps. (b) Shear velocity structure along the D profile crustal section. The final autocorrelation stacks of the AASN network stations along profile D are plotted on top of the V_s profile of Kästle et al. (2018) filtered in the (c) 0.4–1 Hz and (d) 0.5–1 Hz frequency bands. The short red horizontal lines mark the picked reflectivity changes along the autocorrelation stacks. Moho boundary lines (white color) in the cross sections for European and Adriatic Plate and the Liguro-Provençal-Tyrrhenian Domain (LPTD) are taken from the receiver function and CSS study of Spada et al. (2013). CA marks the Central Alps area. PoB, Po Molasse Basin; Ap, Apennines.

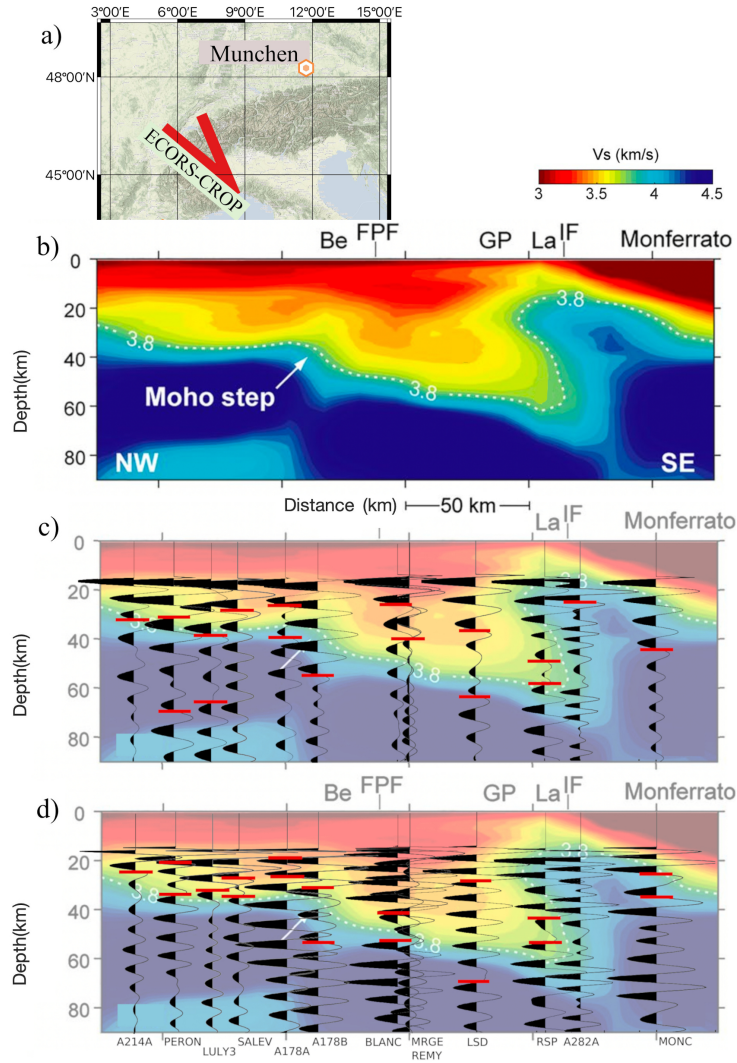


Figure 5.8 (a) The map shows the locations, red lines, of profile ECORS-CROP and NFP-20 West, Fig. 5.9, in the Western Alps. (b) From Malusà et al. (2021), the Vs profile of the crust and the mantle wedge along the ECORS-CROP profile as revealed by Bayesian transdimensional (TransD) inversion of Rayleigh wave dispersion data after Zhao et al. (2020). The white arrow indicates a major (~ 8 km) Moho step beneath the western front of the Belledonne massif (Be). The white dashed isovelocity lines indicate $V_s = 3.8 \text{ km s}^{-1}$ and the crust–mantle boundary. The final autocorrelation stacks filtered in the (c) 0.4–1 Hz and (d) 0.5–1 Hz frequency bands, are superimposed on the profile. The short red horizontal lines mark the reflectivity changes detected on the the autocorrelation stacks. FPF marks the Frontal Pennine Fault. GP, Gran Paradiso; La, Lanzo; IF, Insubric Fault.

detect crustal discontinuities. Along the V_s profile there is in the north-northwest (NNW) a deep V_s discontinuity marking a decreasing in velocity. The depth of this discontinuity matches the depth of the second picked reflectivity change of the station—TORNY—positioned in this area for both the 0.4–1 and 0.5–1 Hz frequency bands.

Geological profiles

Figs 5.10–5.12 shows the geological cross-sections by Schmid et al. (2017) and the final autocorrelation stacks in the 0.4–1 and 0.5–1 Hz frequency bands of the stations along these profiles. The prior Moho, blue line, in these cross-sections is a combination of the results by Wagner et al. (2012) and Spada et al. (2013). The depths of the picked reflectivity changes are outlined by short red horizontal lines. The autocorrelation stacks that have only 1 pick or no picks are due to absent stable reflections along the daily stacks that correspond to a change in reflectivity along the final autocorrelation stack. The depths of the picked reflectivity changes along the Argentera cross-section, Fig. 5.10, do not correspond to the prior Moho. The picked reflectivity changes in the 0.4–1 Hz band of stations A194A and A281A closely corresponds to the upper–lower crust discontinuity of the European Plate and Adriatic Plate, respectively.

Fig. 5.11 shows the geological cross-section of the Pelvoux profile and the autocorrelation stacks along the profile. The depths of the picked reflectivity changes filtered in the 0.4–1 Hz band, Fig. 5.11(b), shows close correspondence with the prior Moho, blue line. The depths of the first picked reflectivity changes of stations A185A and A282A closely matches the prior Moho. The depths of the second picked reflectivity changes of stations A181A and BNI closely matches the prior Moho.

In the 0.5–1 Hz band, Fig. 5.11(c), the depth of the picked reflectivity change of station A185A closely matches the European upper–lower crust boundary and results shallower than the pick in the 0.4–1 Hz band. The depth of the first and second picked reflectivity changes of stations A181A are close to the European upper–lower crust boundary. For the same station a clear phase is detectable at the prior Moho that is not the most distinctive phase along the stack. The depth of the first picked reflectivity change of station RRL closely matches the prior Moho. The depth of the first picked reflectivity change of station MONC matches the Adriatic upper–lower crust boundary. The second picked reflectivity change of station MONC closely matches the prior Moho.

Fig. 5.12 shows the geological cross-section of the Ticino profile and the autocorrelation stacks along the profile. The depths of the first picked reflectivity changes of stations A060B and FUSIO in the 0.4–1 Hz band, Fig. 5.12(b), shows close correspondence with the prior Moho depth, blue line. The depth of the second picked reflectivity change of station GRIMS closely matches the prior Moho depth. The depths of the first picked reflectivity changes of stations GRIMS and VARE closely

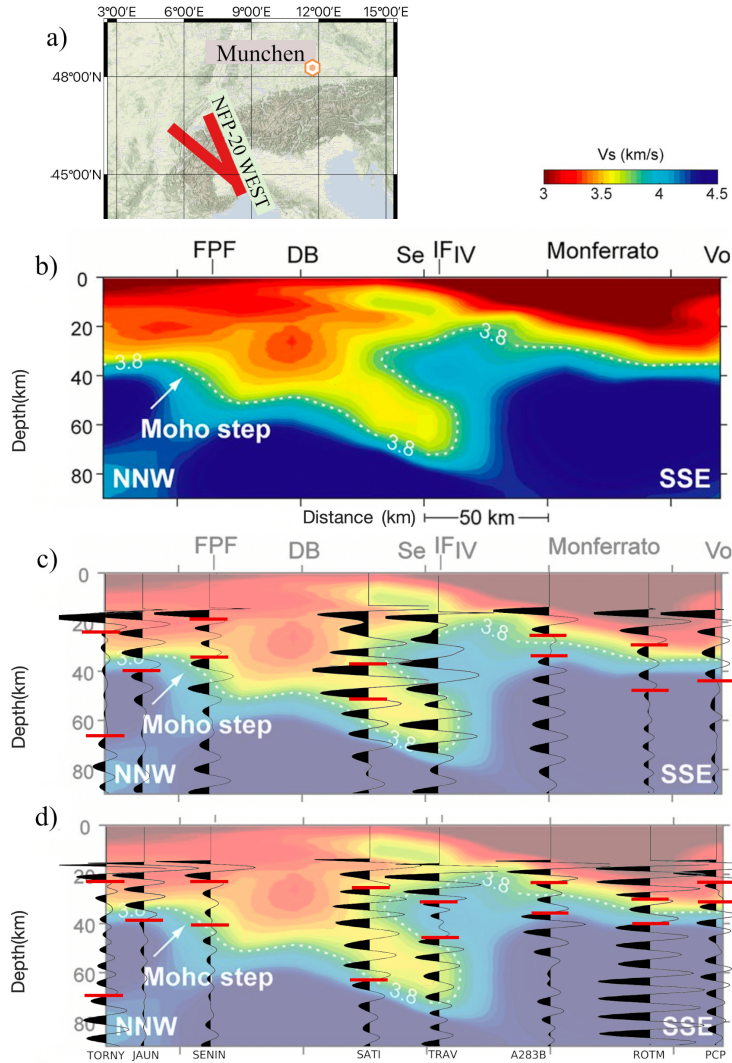


Figure 5.9 (a) The map shows the locations, red lines, of profile NFP-20 West and ECORS-CROP, Fig. 5.8, in the Western Alps. (b) From Malusà et al. (2021), the Vs profile of the crust and the mantle wedge along the NFP-20 West profile as revealed by Bayesian transdimensional (TransD) inversion of Rayleigh wave dispersion data after Zhao et al. (2020). The white arrow indicates a Moho step observed in correspondence with the Frontal Pennine Fault (FPF). The white dashed isovelocity lines indicate $V_s = 3.8 \text{ km s}^{-1}$ and the crust–mantle boundary. The final autocorrelation stacks filtered in the (c) 0.4–1 Hz and (d) 0.5–1 Hz frequency bands, are superimposed on the profile. The red horizontal lines mark the picked reflectivity changes along the autocorrelation stacks. DB marks the Dent Blanche. SE, Sesia-Lanzo; IF, Insubric Fault; IV, Ivrea-Verbano; Vo, Voltri.

corresponds to the prior upper–lower crust boundary of the European Plate and Adriatic Plate, respectively.

In the 0.5–1 Hz band, Fig. 5.12(c), the depths of the first picked reflectivity changes of the stations GRIMS and FUSIO closely matches the European upper–lower crust boundary of the geological profile by Schmid et al. (2017). For the same stations, the depths of the second picked reflectivity changes are slightly shallower than the prior Moho depth, blue line. Station A062A is positioned on top of the subduction zone and shows the same trend of the reflectivity changes of stations GRIMS and FUSIO. For the three stations the first and second picked reflectivity changes corresponds to a decrease and increase in amplitude along the final stacks, respectively.

5.3.3 Geological setting: European basement, External massifs

To probe a relation between a specific geological region and picked reflectivity changes, we select 4 stations that are positioned on top of the European basement (External massifs). In Fig. 5.13 we plot the final autocorrelation stacks of 4 stations—LAUCH, FIESA, GRIMS, NALPS—in the 0.4–1 and 0.5–1 Hz frequency bands. These stations have an ~ 20 –30 km inter-station distance. The reflectivity changes are marked by short green horizontal lines in Figs 5.13(f) and (g). The results of the final stacks show little spatial coherence between the P -wave reflections. The depths of the picked reflectivity changes for stations FIESA and GRIMS that are related to amplitude changes show the same results in the different frequency bands. For these stations there is a large amplitude decrease between the picked reflectivity changes. The depths of the picked reflectivity changes of station FIESA are slightly deeper than of station GRIMS. The daily stacks of stations LAUCH and NALPS resulted in a repeated high frequency occurrence. This may influence the reflectivity changes in the 0.5–1 Hz band and have not been further investigated. The results of these stations show no significant relation between the reflections of the final stacks and the geological region. The depths of the picked reflectivity changes are close to the depth of the prior Moho by Spada et al. (2013).

5.4 Discussion

The majority of the P -wave Moho reflections in the Western Alps are related to reflectivity changes or the base of crustal reflections as opposed to clear distinct phases that were detected by Tibuleac & von Seggern (2012) in the Nevada area and Mroczek & Tilmann (2021) in the Bohemian Massif. The reflectivity changes at the base of crustal reflections were also detected in the southwestern Alps by Ashruf & Morelli (2022).

We have picked the depths of the first two detectable reflectivity changes in the

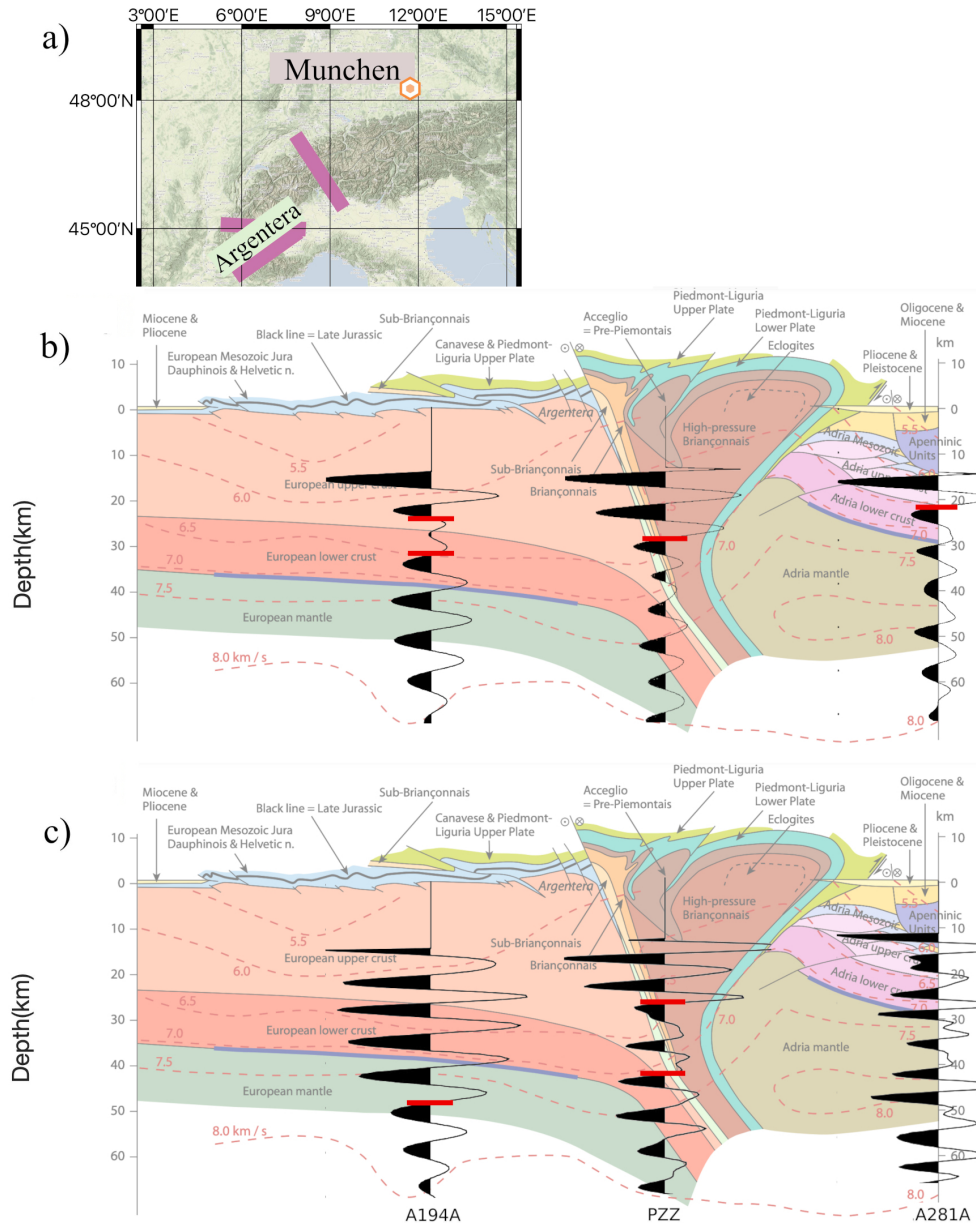


Figure 5.10 (a) The map shows the locations, pink lines, of the Argentera profile and 2 other profiles in the Western Alps by Schmid et al. (2017). The final autocorrelation stacks filtered in the (b) 0.4–1 Hz and (c) 0.5–1 Hz frequency bands are superimposed on the Argentera profile, see Fig. 2.1. The geological profile is superimposed with the P-wave velocity model of Diehl et al. (2009), red dashed lines, and the Moho, blue line, which is a combination from the results by Wagner et al. (2012) and Spada et al. (2013). The short red horizontal lines mark the reflectivity changes detected on the the autocorrelation stacks.

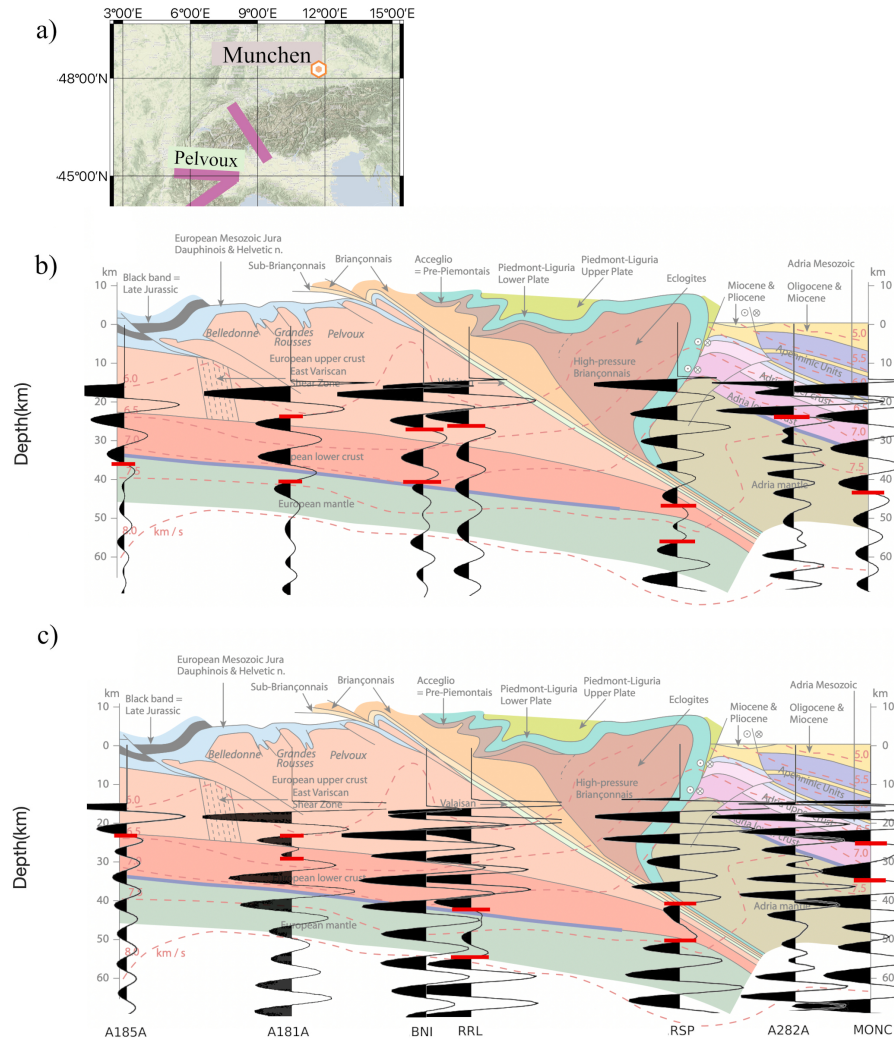


Figure 5.11 (a) The map shows the locations, pink lines, of the Pelvoux profile and 2 other profiles in the Western Alps by Schmid et al. (2017). The final autocorrelation stacks filtered in the (b) 0.4–1 Hz and (c) 0.5–1 Hz frequency bands are superimposed on the Pelvoux profile, see Fig. 2.1. The geological profile is superimposed with the P-wave velocity model of Diehl et al. (2009), red dashed lines, and the Moho, blue line, which is a combination from the results by Wagner et al. (2012) and Spada et al. (2013). The short red horizontal lines mark the reflectivity changes detected on the the autocorrelation stacks.

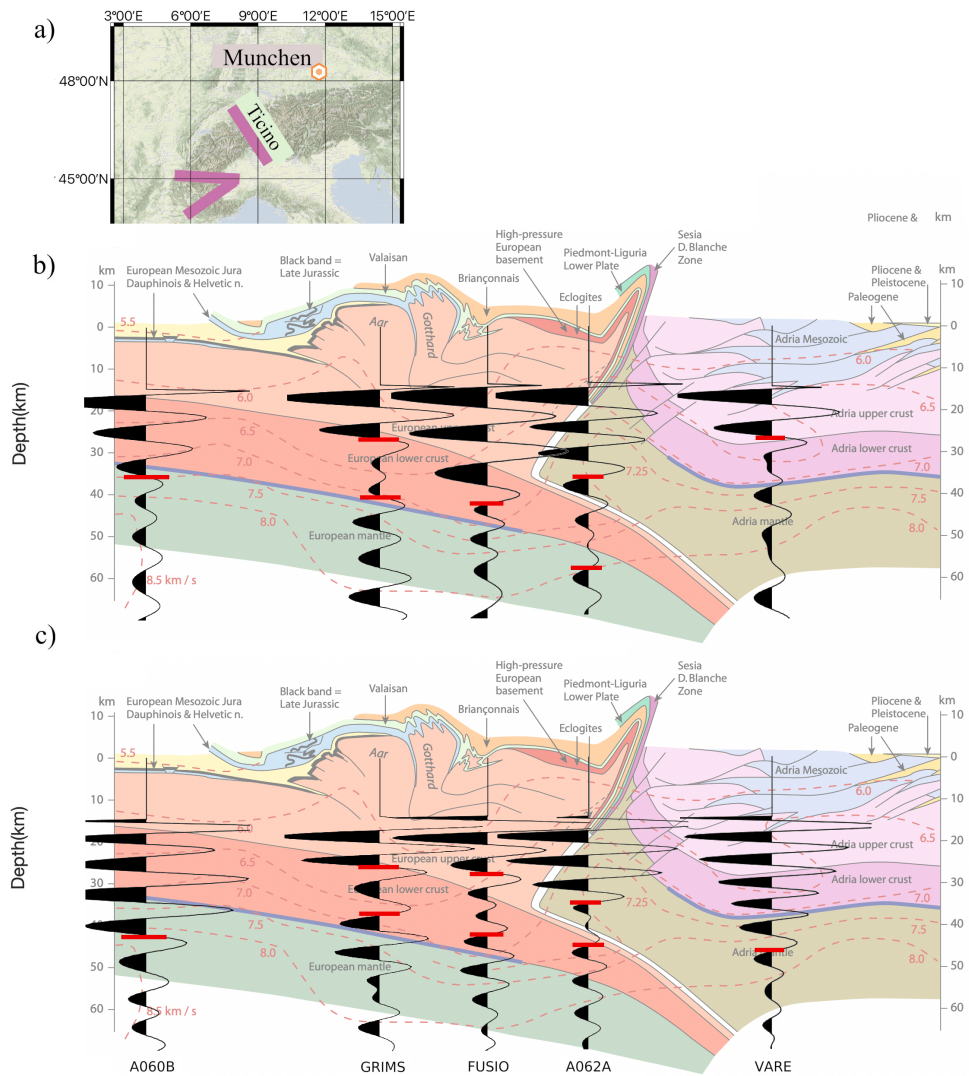


Figure 5.12 (a) The map shows the locations, pink lines, of the Ticino profile and 2 other profiles in the Western Alps by Schmid et al. (2017). The final autocorrelation stacks filtered in the (b) 0.4–1 Hz and (c) 0.5–1 Hz frequency bands are superimposed on the Ticino profile. The short red horizontal lines mark the picked reflectivity changes along the autocorrelation stacks. The geological profile is superimposed with the P-wave velocity model of Diehl et al. (2009), red dashed lines, and the Moho, blue line, which is a combination from the results by Wagner et al. (2012) and Spada et al. (2013).

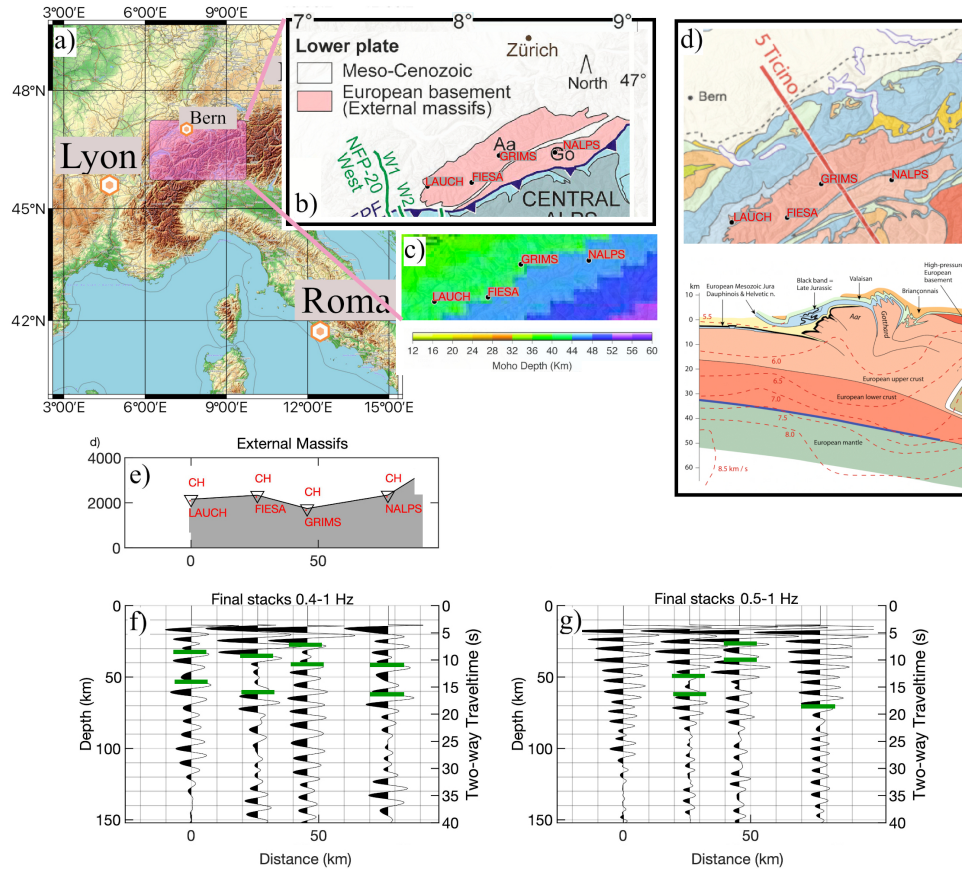


Figure 5.13 a) Topographic map of the Western Alps with the pink rectangle that indicates the area shown in (b) with the 4 stations—LAUCH, FIESA, GRIMS, NALPS—that are situated on top of the European basement (External massifs). (b) Geologic map of Malusà et al. (2021); Aa, Argentera; Go, Gotthard. (c) Moho depth map of Spada et al. (2013). (d) Top: Tectonic map with the stations along the Ticino transect by Schmid et al. (2017). Bottom: Geological cross-section of the Ticino transect. The geological profile is superimposed with the P -wave velocity model of Diehl et al. (2009), red dashed lines, and the Moho, blue line, which is a combination from the results by Wagner et al. (2012) and Spada et al. (2013). (e) The elevation of the stations in metres along the distance (km) from station LAUNCH. The stacked autocorrelations filtered in the (f) 0.4–1 Hz and (g) 0.5–1 Hz frequency bands. The picked reflectivity changes are marked by the short green horizontal lines. We used OpenTopoMap in QGIS (QGIS Development Team, 2022) to create the map in (a).

0.4–1 and 0.5–1 Hz frequency bands without prior Moho information. We have focused on the first two reflectivity changes to probe whether the crust–mantle transition is the only detectable discontinuity without prior information in the Western Alps. The picked reflectivity changes in the mountain region of the Western Alps not only corresponded to the crust–mantle discontinuity but also to the upper–lower crust discontinuity along the cross-sections in Figs 5.4–5.12. The depths of the second picked reflectivity changes in the 0.5–1 Hz band of stations A172A and TORNY in Figs 5.4 and 5.9, respectively, may be due to the deeper Hales discontinuity. This discontinuity has also been previously observed in ambient noise autocorrelation stacks by Taylor et al. (2016). Therefore, identifying the Moho through reflectivity changes without prior information might be biased by other discontinuities. Kennett (2015) shows the high variation at the base of crustal reflection along a reflection profile. Thus, relating the Moho discontinuity to a specific type of reflectivity change at the base of crustal reflection—e.g. increase or decrease in amplitude— might be biased.

The prior profiles to analyse the depths of the picked reflectivity changes, were selected based on their lengths that run at least across the arc of the Western Alps. Therefore, we did not take into account the profiles with shorter lengths obtained from the complementary experiments of the AlpArray Network. However, the migrated receiver function profile by Scarponi et al. (2021), Fig. 5.14, that was created with the use of the IvreaArray complementary experiment and the VARE seismic data, shows a thick velocity increase deepening towards the east. This prominent signal at ~ 28 km depth coincides with the strong amplitude decrease along the final stack of station VARE filtered in the 0.4–1 Hz band. The amplitude decrease is marked by the short red horizontal line in Fig. 5.14(b). In addition, the depth of this strong amplitude decrease along the final stack coincides also with the Moho depth by Spada et al. (2013). The prior Moho depth is marked by the short green horizontal line. The receiver function profile also shows a clear decrease of velocity at ~ 48 km depth that coincides with the amplitude decrease along the final stack of station VARE filtered in the 0.5–1 Hz band. On the contrary, the V_s results by Kästle et al. (2018) in Fig. 5.7 shows at this location and depth a clear increase in velocity. In addition, the V_s profile by Kästle et al. (2018) does not image a strong velocity increase at ~ 28 km depth. The ambient noise autocorrelations has shown the ability to detect both features through changes in reflectivity along the final stacks. The features were detected from two different frequency bands, thus showing the usefulness of filtering the ambient noise autocorrelations in different frequency bands.

We have detected no common relation in the order of picked reflectivity changes to the Moho discontinuity. However, on one hand, the depths of the first picked reflectivity changes show close correspondence with the prior Moho for stations positioned in the European basement. On the other hand, the depths of the second

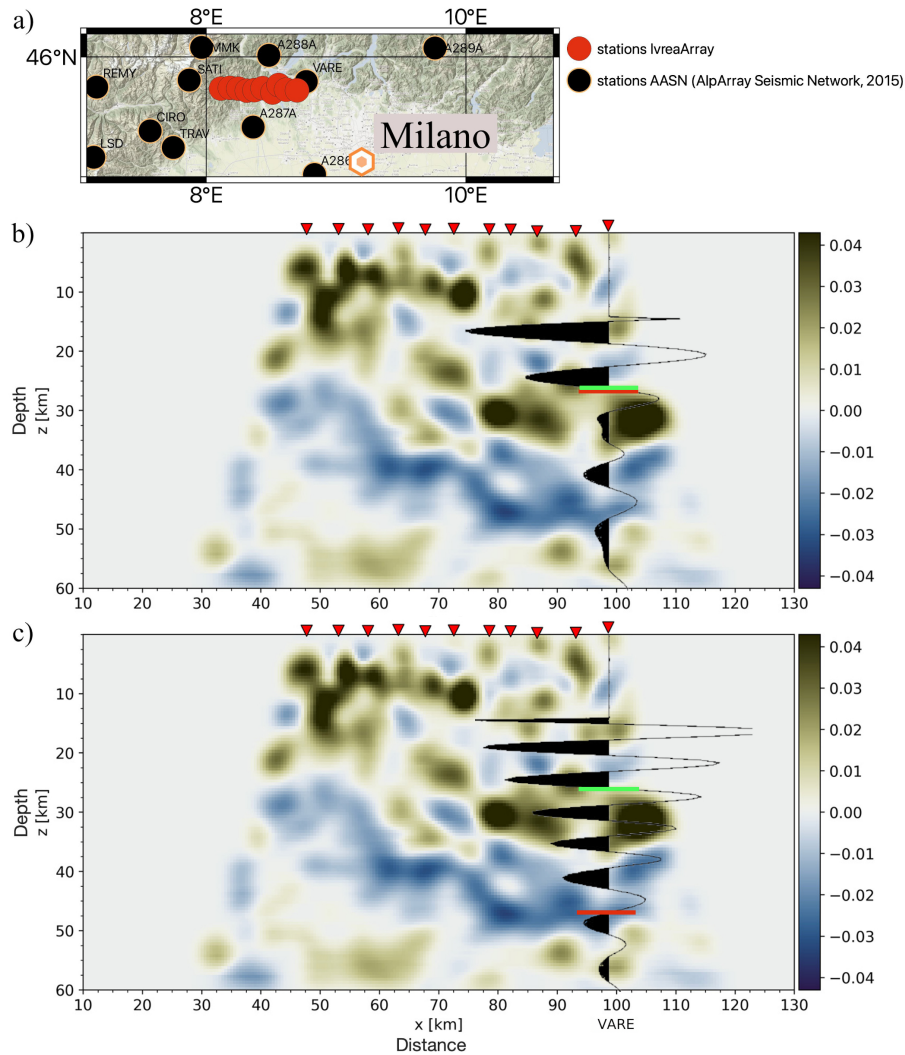


Figure 5.14 (a) The map shows the locations of the stations of the IvreaArray Network (Hetényi et al., 2017), red filled circles, and the nearby AASN stations, e.g. VARE, black filled circles. The final autocorrelation stacks of station VARE filtered in the (b) 0.4–1 Hz and (c) 0.5–1 Hz frequency bands are superimposed on top of the migrated receiver function profile by Scarponi et al. (2021). Colors highlight areas of increasing (brown) and decreasing (blue) shear-wave velocities with depth. The short red horizontal lines mark the picked reflectivity changes along the autocorrelation stacks and the short green horizontal lines the Moho by Spada et al. (2013).

picked reflectivity changes for stations positioned in the mountain region of the Western Alps corresponds to the prior Moho. This might be due to the shallow Moho discontinuity in the European basement deepening towards to the subduction zones in the mountain region. The depths of the first picked reflectivity changes in the subduction zone of the mountain regions closely corresponds to the upper–lower crust discontinuity, Figs 5.10–5.12. In the European basement the upper–lower crust discontinuity is at shallower depths that may not be detected with reflectivity changes in our study due to the muting—0 to 5 s TWT— of the autocorrelation zero-lag sidelobes. To image shallower discontinuities by shortening the zero-lag sidelobes, Romero & Schimmel (2018) shows that increasing the high frequency cut-off the sidelobes become shorter and arrive at earlier lag times.

The autocorrelation stacks are filtered with two different low cut-off frequencies that resulted in different P -wave reflections and depths of the picked reflectivity changes along the final stacks. The sensitivity of the autocorrelation stacks to the frequency range for bandpass filtering has also been shown by Oren & Nowack (2016) and Ashruf & Morelli (2022). In these previous studies the best bandpass filter was chosen based on coherence between the waveforms of the daily stacks and prior information. Picking the best bandpass filter based on prior information might become difficult in an area where there is no prior information.

The low frequency receiver function study by Paul et al. (2021), Fig. 5.4(b), results into wavelengths between 10 and 20 km for the P-to-S converted waves. The lengths are measured from the beginning of the negative polarity, blue pixel, to the end of the positive polarity, red pixel. These wavelengths are much longer than the wavelengths of the autocorrelation stacks, ~ 7 –10 km, that are superimposed on the profile, Figs 5.4(c) and (d). The shorter wavelengths of the autocorrelation stacks favour vertical resolution and may result into better detection of the layer boundaries as opposed to the longer wavelengths of the lower-frequency receiver functions that results into a large positive polarity or single feature for the Moho discontinuity. The large positive polarity may limit the precise depth of the Moho discontinuity.

We have not assessed coherence between the P -wave reflections of the autocorrelation stacks as done by Ashruf & Morelli (2022) in the southwestern Alps that used the CIFALPS network. The CIFALPS network has a dense inter-station distance of 5–10 km as opposed to the large inter-station distance, ~ 52 km, of the AASN. The large inter-station distance might cause spurious interpretation in the continuity or discontinuity of the earth structures. However, the few stations—e.g. MRGE and REMY— that are positioned very close to each other, ~ 10 km, resulted in spatial coherence.

Moho discontinuity from reflectivity changes of ambient noise autocorrelations

Fig. 5.15 shows the depths of the reflectivity changes that are likely associated to the Moho discontinuity in the 0.4–1 and 0.5–1 Hz frequency bands. The depths

of the picked reflectivity changes are a combination of the first and second picked reflectivity changes. We have selected the first picked reflectivity change for the stations situated in the European basement and Po Plain. In addition, the second picked reflectivity change has been selected for the stations situated in the mountain regions of the Western Alps and Apennine.

The Moho depths from the reflectivity changes in the 0.4–1 and 0.5–1 Hz frequency bands, Figs 5.15(a) and (b), show clear deepening— ~ 20 to 70 km—towards the arc of the Western Alps. In addition, there is no uniform deepening and there are clear differences from the east to the west and from the south to the north. This is further evidence of the complex Moho structure in the Western Alps. This complexity and diversity has also been shown by the receiver function study of Paul et al. (2021) by comparing the southwestern Alps with the northwestern Alps. Furthermore, there are some Moho depths that show some differences with the surrounding stations and prior Moho information. These anomalies might be due to the unstable noise field that does not produce a clear stability along the daily stacks. A further study between the noise field and position of the stations might give insight on these anomalous depths.

The reflectivity changes along the final stacks to create the Moho depth maps in Fig. 5.15 are picked without *a priori* time window or uncertainty window as performed by the ambient noise autocorrelation study by Becker & Knapmeyer-Endrun (2018). We used the EU60 velocity model from Zhu & Tromp (2013) that has a maximum average P-wave velocity perturbation of $\sim 5\%$ within the depth range of 0–70 km. This results into a maximum depth uncertainty of ~ 3.5 km for a Moho depth of ~ 70 km.

Mroczek & Tilmann (2021) shows that for a simple 1-layer structure, strong phases occur that are not related to the Moho reflections in the autocorrelation stacks. These strong phases can complicate the associations of the reflectivity changes to the Moho discontinuity further when there is a lack of prior information.

5.5 Conclusions

We image the Moho discontinuity in the Western Alps from independently picking reflectivity changes in the ambient seismic noise autocorrelations. The autocorrelation stacks are filtered in the 0.4–1 and 0.5–1 Hz frequency bands and converted from time to depth. We picked the first two reflectivity changes along the final stack that coincide with stable reflections along the daily stack. The reflectivity changes are picked without prior information of the Earth layers. Afterwards, we compare the depths of the picked reflectivity changes with a prior Moho map and cross-sections of the Western Alps. The depths of the first picked reflectivity changes in the Eu-

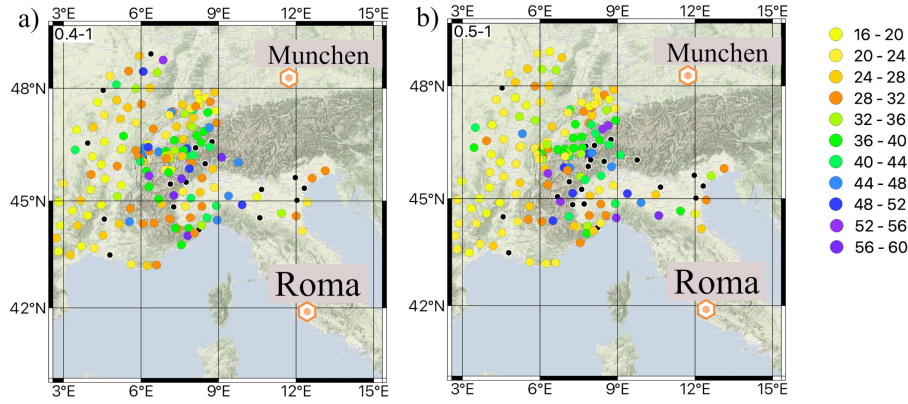


Figure 5.15 The depths (km) of the picked reflectivity changes associated to the Moho discontinuity in the (a) 0.4–1 Hz and (b) 0.5–1 Hz frequency bands. The depths are a combination of the first and second picked reflectivity changes, see text for further explanation. The colour scale is shown on the right-hand side and follows the same scale as used by Spada *et al.* (2013). The black circles denote the stations with no detected reflectivity change. We used Stamen Terrain and Esri Topo in QGIS (QGIS Development Team, 2022) to create the maps.

ropean basement and Po Plain correspond closely to prior information of the Moho discontinuity. In the arc of the Western Alps the depths of the first picked reflectivity changes are mainly shallow and relate to the upper–lower crust discontinuity. In addition to the arc of the Western Alps, the depths of the second picked reflectivity changes are in close correspondence with the prior Moho. This shows that the Moho discontinuity does not produce the only reflectivity change along the autocorrelation stacks. Therefore, in an area where there is no prior information, associating the Moho discontinuity to picked reflectivity changes might be biased. The complex Moho discontinuity shows clear thickening from the European basement, ~ 20 km, towards the arc of the Western Alps, ~ 70 km, that diminishes again towards the Po Plain.

Chapter 6

Conclusions

Ambient seismic noise autocorrelations proves to be a useful method to image the Moho discontinuity of the Western Alps. The new Moho depths are calculated by using more than 200 stations from the CIFALPS network and AASN. The final autocorrelation stacks are created by stacking hourly autocorrelations over a maximum amount of 2 years per station. The effect of earthquakes and non-stationary sources close to the stations are removed through time-domain normalization (Bensen et al., 2007). The ambient noise autocorrelations are filtered using different cut-off frequencies in the 0.09–2 Hz frequency range. The frequency bands with cut-off frequencies lower than 0.4 Hz results into wavelengths that are too long to detect fine crustal boundaries. Furthermore, the frequency bands with cut-off frequency above 1 Hz, results into less stable daily autocorrelation stacks due to the daily and weekly variations linked to human activities. Therefore, the 0.5–1 Hz band gives the best results for imaging the Moho discontinuity along the CIFALPS transect in the southwestern Alps. The resulting Moho depth shows a steeper trend, ~ 55 to ~ 70 km, of the European Plate subducting underneath the Adriatic Plate as compared to previous studies (e.g. Zhao et al., 2015). The autocorrelations reflectivity profile has the ability to image also other crust–mantle structures along the dense CIFALPS network—interstation distance of ~ 5 – 10 km— that is not possible with the larger interstation distance of the AASN. The reflectivity profile of the CIFALPS transect shows spatial coherence and a reflective transparent area due to, respectively, the homogenous crustal structure and the Ivrea mantle wedge reaching shallow crustal depths. The autocorrelations of the AASN stations are also filtered in the 0.4–1 Hz band. The Moho depth maps of the AASN stations for the two different frequency bands resulted for the majority of the stations into similar results. The Moho depth maps show the complex Moho structure in the Western Alps; there is no uniform deepening of the Moho from the European basement, ~ 20 km, towards the arc of the Western Alps, ~ 70 km. In addition, there are clear differences between the Moho depths of the southwestern -and northwestern Alps.

The Moho discontinuity from ambient noise autocorrelations in the Western Alps are associated to changes in reflectivity and not to a single clear pulse. The reflectivity changes are extracted using two techniques. The first technique is derived from the automatic method by Becker & Knapmeyer-Endrun (2018) by extracting from the second derivative autocorrelation envelope, the local maxima inside an *a priori* time window that is based on prior crust–mantle information. For the second technique, the most stable reflection is picked along the daily stacks that coincides with a clear change in reflectivity along the final autocorrelation stack. The second technique is performed without prior information.

The picking of reflectivity changes without prior information is a good alternative for areas with controversial results or with no prior information. However, the Moho is not the only discontinuity that provides reflectivity changes. The shallower discontinuities, e.g. upper–lower crust, and deeper discontinuities, e.g. Hales discontinuity, may cause bias interpretations. Therefore, the reflectivity changes picked alongside the autocorrelations of the AASN stations are compared to previous cross-sections (e.g. Kästle et al., 2018). The first picked reflectivity changes in the European basement and Po Plain corresponds closely to the prior Moho, and in the arc of the Western Alps the depths of the second picked reflectivity changes are in close correspondence with the prior Moho.

Synthetic autocorrelations may help to understand the relations between crustal structure and autocorrelations. Such synthetic experiments may be implemented either via forward calculation of the synthetic reflection response of a flat-layered, 1D, model (e.g. Gorbatov et al., 2013); or else by generating and propagating the noise field in an arbitrarily complex model to the stations, and then autocorrelating the resulting time series (e.g. Romero & Schimmel, 2018). We do not show such experiments here, but keep this as a planned future development.

Ambient seismic noise autocorrelations have shown to be a reliable tool, particularly when some prior information on the depth of discontinuities is available. However, to use the method independently from prior crust–mantle information, some different type of analysis may be required in order to unambiguously identify the reflectivity changes due to the Moho discontinuity. An operator is generally able to draw such conclusions from visual examination. This might convince us that such analysis could be automatically done by developing a machine learning algorithm that can accurately pick the reflectivity changes associated to the Moho discontinuity. This type of algorithm may be developed by training a neural network on ambient noise data and different types of geophysical information to calculate the Moho depth underneath a specific station.

Bibliography

Bibliography

Akinci, A., Mueller, C., Malagnini, L., & Lombardi, A., 2004. Seismic hazard estimate in the alps and apennines (italy) using smoothed historical seismicity and regionalized predictive ground-motion relationships, *Boll. Geofis. Teor. Appl.*, **45**(4), 285–304.

AlpArray Seismic Network, 2015. Alpparray seismic network (aasn) temporary component.

Ashruf, T. N. & Morelli, A., 2022. The Moho reflectivity of the subduction beneath the Southwestern Alps from ambient seismic noise autocorrelations, *Geophysical Journal International*, **230**(1), 298–316.

Ashruf, T. N. & Morelli, A., in preparation. Moho structure of the Western Alps from seismic noise autocorrelation of AlpArray data.

Asten, M., 1976. The use of microseisms in geophysical exploration, *Ph. D. thesis, Macquarie University*.

Becker, G. & Knapmeyer-Endrun, B., 2018. Crustal thickness across the trans-european suture zone from ambient noise autocorrelations, *Geophysical Journal International*, **212**(2), 1237–1254.

Becker, G. & Knapmeyer-Endrun, B., 2019a. Crustal thickness from horizontal component seismic noise auto-and cross-correlations for stations in central and eastern europe, *Geophysical Journal International*, **218**(1), 429–445.

Becker, G. & Knapmeyer-Endrun, B., 2019b. Reply to âComment on âCrustal thickness across the Trans-European Suture Zone from ambient noise autocorrelationsâ by G. Becker and B. Knapmeyer-Endrunâ by G. Helffrich, *Geophysical Journal International*, **217**(2), 1261–1266.

- Beller, S., Monteiller, V., Operto, S., Nolet, G., Paul, A., & Zhao, L., 2018. Lithospheric architecture of the south-western alps revealed by multiparameter teleseismic full-waveform inversion, *Geophysical Journal International*, **212**(2), 1369–1388.
- Bensen, G., Ritzwoller, M., Barmin, M., Levshin, A., Lin, F., Moschetti, M., Shapiro, N., & Yang, Y., 2007. Processing seismic ambient noise data to obtain reliable broad-band surface wave dispersion measurements, *Geophysical Journal International*, **169**(3), 1239–1260.
- Bonnefoy-Claudet, S., Cotton, F., & Bard, P.-Y., 2006. The nature of noise wavefield and its applications for site effects studies: A literature review, *Earth-Science Reviews*, **79**(3-4), 205–227.
- CERN, 2016. Cern seismic network.
- Claerbout, J. F., 1968. Synthesis of a layered medium from its acoustic transmission response, *Geophysics*, **33**(2), 264–269.
- Closs, H. & Labrouste, Y., 1963. *Recherches séismologiques dans les Alpes occidentales au moyen de grandes explosions en 1956, 1958 et 1960: mémoire collectif du Groupe d'Études des explosions Alpines*.
- Diehl, T., Husen, S., Kissling, E., & Deichmann, N., 2009. High-resolution 3-dp-wave model of the alpine crust, *Geophysical Journal International*, **179**(2), 1133–1147.
- Gorbatov, A., Saygin, E., & Kennett, B., 2013. Crustal properties from seismic station autocorrelograms, *Geophysical Journal International*, **192**(2), 861–870.
- Grellet, B., Combes, P., & Granier, T., 1993. *Sismotectonique de la France métropolitaine dans son cadre géologique et géophysique: avec atlas de 23 cartes au 1/4 000 000ème et une carte au 1/1 000 000ème*, vol. 2, Société géologique de France.
- Handy, M. R., Schmid, S. M., Bousquet, R., Kissling, E., & Bernoulli, D., 2010. Reconciling plate-tectonic reconstructions of alpine tethys with the geological–geophysical record of spreading and subduction in the alps, *Earth-Science Reviews*, **102**(3-4), 121–158.
- Helfrich, G., 2019. Comment on âCrustal thickness across the Trans-European Suture Zone from ambient noise autocorrelationsâ by G. Becker and B. Knapmeyer-Endrun, *Geophysical Journal International*, **217**(2), 906–908.
- Hetényi, G., Plomerová, J., Solarino, S., Scarponi, M., Vecsey, L., Munzarová, H., Babuška, V., Jedlička, P., Kotek, J., & Colavitti, L., 2017. Ivreaarray an alparray complementary experiment, *Zenodo*.

Hetényi, G., Molinari, I., Clinton, J., Bokelmann, G., Bondár, I., Crawford, W. C., Dessa, J.-X., Doubre, C., Friederich, W., Fuchs, F., et al., 2018. The alparray seismic network: a large-scale european experiment to image the alpine orogen, *Surveys in geophysics*, **39**(5), 1009–1033.

INGV Seismological Data Centre, 1997. Rete sismica nazionale (rsn).

Ito, Y., Shiomi, K., Nakajima, J., & Hino, R., 2012. Autocorrelation analysis of ambient noise in northeastern japan subduction zone, *Tectonophysics*, **572**, 38–46.

Kästle, E. D., El-Sharkawy, A., Boschi, L., Meier, T., Rosenberg, C., Bellahsen, N., Cristiano, L., & Weidle, C., 2018. Surface wave tomography of the alps using ambient-noise and earthquake phase velocity measurements, *Journal of Geophysical Research: Solid Earth*, **123**(2), 1770–1792.

Kennett, B., 2015. Lithosphere–asthenosphere p-wave reflectivity across australia, *Earth and Planetary Science Letters*, **431**, 225–235.

Kennett, B., Salmon, M., Saygin, E., & Group, A. W., 2011. Ausmoho: the variation of moho depth in australia, *Geophysical Journal International*, **187**(2), 946–958.

Kennett, B., Saygin, E., & Salmon, M., 2015. Stacking autocorrelograms to map moho depth with high spatial resolution in southeastern australia, *Geophysical Research Letters*, **42**(18), 7490–7497.

Krischer, L., Megies, T., Barsch, R., Beyreuther, M., Lecocq, T., Caudron, C., & Wassermann, J., 2015. ObsPy: a bridge for seismology into the scientific python ecosystem, *Computational Science & Discovery*, **8**(1), 014003.

Lai, X., Li, S., & Sun, Y., 2010. Exploration of fault-zone trapped waves at pingtong town, in wenchuan earthquake region, *Geodesy and Geodynamics*, **1**(1), 29–33.

Langston, C. A., 1979. Structure under mount rainier, washington, inferred from teleseismic body waves, *Journal of Geophysical Research: Solid Earth*, **84**(B9), 4749–4762.

Li, H., Zhu, L., & Yang, H., 2007. High-resolution structures of the landers fault zone inferred from aftershock waveform data, *Geophysical Journal International*, **171**(3), 1295–1307.

Lombardi, D., Braunmiller, J., Kissling, E., & Giardini, D., 2008. Moho depth and poisson’s ratio in the western-central alps from receiver functions, *Geophysical Journal International*, **173**(1), 249–264.

- Lu, Y., Stehly, L., Paul, A., & Group, A. W., 2018. High-resolution surface wave tomography of the european crust and uppermost mantle from ambient seismic noise, *Geophysical Journal International*, **214**(2), 1136–1150.
- Lyu, C., Pedersen, H. A., Paul, A., Zhao, L., & Solarino, S., 2017. Shear wave velocities in the upper mantle of the western alps: new constraints using array analysis of seismic surface waves, *Geophysical Journal International*, **210**(1), 321–331.
- Malusà, M. G., Guillot, S., Zhao, L., Paul, A., Solarino, S., Dumont, T., Schwartz, S., Aubert, C., Baccheschi, P., Eva, E., et al., 2021. The deep structure of the alps based on the cifalps seismic experiment: A synthesis, *Geochemistry, Geophysics, Geosystems*, **22**(3), e2020GC009466.
- MedNet Project Partner Institutions, 1988. Mediterranean very broadband seismographic network (mednet).
- Mohorovičić, A., 1910. Das beben vom 8. x. 1909, *Jahrbuch des meteorologischen Observatoriums in Zagreb (Agram) für das Jahr 1909*, **9**(4), 1–63.
- Mroczek, S. & Tilmann, F., 2021. Joint ambient noise autocorrelation and receiver function analysis of the Moho, *Geophysical Journal International*, **225**(3), 1920–1934.
- Nakata, N., Gualtieri, L., & Fichtner, A., 2019. *Seismic ambient noise*, Cambridge University Press.
- Nicolas, A., Hirn, A., Nicolich, R., & Polino, R., 1990. Lithospheric wedging in the western alps inferred from the ecors-crop traverse, *Geology*, **18**(7), 587–590.
- Nicole, B., Christian, S., Anne, P., Jean, V., Julien, F., François, T., & Marco, C., 2007. Local tomography and focal mechanisms in the south-western alps: comparison of methods and tectonic implications, *Tectonophysics*, **432**(1-4), 1–19.
- Nishida, K., 2017. Ambient seismic wave field, *Proceedings of the Japan Academy, Series B*, **93**(7), 423–448.
- Nouibat, A., Stehly, L., Paul, A., Schwartz, S., Bodin, T., Dumont, T., Rolland, Y., & Brossier, R., 2022. Lithospheric transdimensional ambient-noise tomography of w-europe: implications for crustal-scale geometry of the w-alps, *Geophysical Journal International*.
- Oren, C. & Nowack, R. L., 2016. Seismic body-wave interferometry using noise auto-correlations for crustal structure, *Geophysical Journal International*, p. ggw394.

Panza, G. & Mueller, S., 1979. The plate boundary between eurasia and africa in the alpine area, *Mem. Sci. Geol.*, **33**, 43–50.

Paul, A., Nouibat, A., Zhao, L., Solarino, S., Schwartz, S., Malusà, M., Stehly, L., Aubert, C., Dumont, T., Eva, E., et al., 2021. Striking differences in lithospheric structure between the north-and south-western alps: insights from receiver functions along the civalps profiles and a new vs model, Tech. rep., Copernicus Meetings.

Phạm, T.-S. & Tkalčić, H., 2017. On the feasibility and use of teleseismic p wave coda autocorrelation for mapping shallow seismic discontinuities, *Journal of Geophysical Research: Solid Earth*, **122**(5), 3776–3791.

Piana Agostinetti, N., Salimbeni, S., Pondrelli, S., Malusa, M., Zhao, L., Eva, E., Solarino, S., Paul, A., Guillot, S., Schwartz, S., et al., 2017. Mantle wedge anisotropy beneath the western alps: insights from receiver function analysis, in *EGU General Assembly Conference Abstracts*, vol. 19, p. 12545.

QGIS Development Team, 2022. *QGIS Geographic Information System*, Open Source Geospatial Foundation.

Robertson, E. C., 2001. *The interior of the Earth*, Washington: Government Printing Office.

Romero, P. & Schimmel, M., 2018. Mapping the basement of the ebro basin in spain with seismic ambient noise autocorrelations, *Journal of Geophysical Research: Solid Earth*, **123**(6), 5052–5067.

Roux, P., Sabra, K. G., Kuperman, W. A., & Roux, A., 2005. Ambient noise cross correlation in free space: Theoretical approach, *J. Acoust. Soc. Am.*, **117**(1), 79–84.

Ruigrok, E., Campman, X., & Wapenaar, K., 2011. Extraction of p-wave reflections from microseisms, *Comptes Rendus Geoscience*, **343**(8-9), 512–525.

Salimbeni, S., Malusà, M. G., Zhao, L., Guillot, S., Pondrelli, S., Margheriti, L., Paul, A., Solarino, S., Aubert, C., Dumont, T., et al., 2018. Active and fossil mantle flows in the western alpine region unravelled by seismic anisotropy analysis and high-resolution p wave tomography, *Tectonophysics*, **731**, 35–47.

Saygin, E., Cummins, P. R., & Lumley, D., 2017. Retrieval of the p wave reflectivity response from autocorrelation of seismic noise: Jakarta basin, indonesia, *Geophysical Research Letters*, **44**(2), 792–799.

Scarponi, M., Hetényi, G., Plomerová, J., Solarino, S., Baron, L., & Petri, B., 2021. Joint seismic and gravity data inversion to image intra-crustal structures:

The Ivrea geophysical body along the Val Sesia profile (Piedmont, Italy), *Frontiers in Earth Science*, **9**, 671412.

Schimmel, M., 1999. Phase cross-correlations: Design, comparisons, and applications, *Bulletin of the Seismological Society of America*, **89**(5), 1366–1378.

Schimmel, M., Stutzmann, E., & Ventosa, S., 2018. Low-frequency ambient noise autocorrelations: Waveforms and normal modes, *Seismological Research Letters*, **89**(4), 1488–1496.

Schimmel, M., Stutzmann, E., Lognonné, P., Compaire, N., Davis, P., Drilleau, M., Garcia, R., Kim, D., Knappmeyer-Endrun, B., Lekic, V., et al., 2021. Seismic noise autocorrelations on Mars, *Earth and Space Science*, p. e2021EA001755.

Schmid, S. & Kissling, E., 2000. The arc of the western Alps in the light of geophysical data on deep crustal structure, *Tectonics*, **19**(1), 62–85.

Schmid, S., Kissling, E., Diehl, T., van Hinsbergen, D. J., & Molli, G., 2017. Ivrea mantle wedge, arc of the western Alps, and kinematic evolution of the Alps–Apennines orogenic system, *Swiss Journal of Geosciences*, pp. 1–32.

Schuster, G., 2009. *Seismic interferometry*, Cambridge University Press.

Spada, M., Bianchi, I., Kissling, E., Agostinetti, N. P., & Wiemer, S., 2013. Combining controlled-source seismology and receiver function information to derive 3-D Moho topography for Italy, *Geophysical Journal International*, **194**(2), 1050–1068.

Swiss Seismological Service (SED) At ETH Zurich, 1983. National seismic networks of Switzerland.

Swiss Seismological Service (SED) At ETH Zurich, 2005. Temporary deployments in Switzerland associated with aftershocks and other seismic sequences.

Taylor, G., Rost, S., & Houseman, G., 2016. Crustal imaging across the North Anatolian fault zone from the autocorrelation of ambient seismic noise, *Geophysical Research Letters*, **43**(6), 2502–2509.

Thouvenot, F., Paul, A., Frechet, J., Béthoux, N., Jenatton, L., & Guiguet, R., 2007. Are there really superposed Mohos in the southwestern Alps? New seismic data from fan-profiling reflections, *Geophysical Journal International*, **170**(3), 1180–1194.

Tibuleac, I. M. & von Seggern, D., 2012. Crust–mantle boundary reflectors in Nevada from ambient seismic noise autocorrelations, *Geophysical Journal International*, **189**(1), 493–500.

University of Genoa, 1967. Regional seismic network of north western Italy.

- van Hinsbergen, D. J., Torsvik, T. H., Schmid, S. M., MaÅlenco, L. C., Maffione, M., Vissers, R. L., Grer, D., & Spakman, W., 2020. Orogenic architecture of the Mediterranean region and kinematic reconstruction of its tectonic evolution since the Triassic, *Gondwana Res.*, **81**, 79–229.
- Viens, L., Jiang, C., & Denolle, M. A., 2022. Imaging the Kanto Basin seismic basement with earthquake and noise autocorrelation functions, *Geophysical Journal International*, ggac101.
- Wagner, M., Kissling, E., & Husen, S., 2012. Combining controlled-source seismology and local earthquake tomography to derive a 3-d crustal model of the western alpine region, *Geophysical Journal International*, **191**(2), 789–802.
- Wapenaar, K., Draganov, D., & Robertsson, J. O., 2008. *Seismic interferometry: History and present status*, Society of Exploration Geophysicists.
- Wapenaar, K., Draganov, D., Snieder, R., Campman, X., & Verdel, A., 2010. Tutorial on seismic interferometry: Part 1âbasic principles and applications, *Geophysics*, **75**(5), 75A195–75A209.
- Yilmaz, O., 2001. *Seismic data analysis: Processing, inversion, and interpretation of seismic data*, vol. 2, Society of Exploration Geophysicists.
- Zhang, Y. & Zindler, A., 1993. Distribution and evolution of carbon and nitrogen in earth, *Earth and Planetary Science Letters*, **117**(3-4), 331–345.
- Zhao, L., Paul, A., Guillot, S., Solarino, S., Malusà, M. G., Zheng, T., Aubert, C., Salimbeni, S., Dumont, T., Schwartz, S., et al., 2015. First seismic evidence for continental subduction beneath the western alps, *Geology*, **43**(9), 815–818.
- Zhao, L., Paul, A., Solarino, S., & RESIF, 2016. Seismic network YP: CIFALPS temporary experiment (China-Italy-France Alps seismic transect) [data set], *RESIF - Reseau Sismologique et geodesique Francais*.
- Zhao, L., Malusà, M. G., Yuan, H., Paul, A., Guillot, S., Lu, Y., Stehly, L., Solarino, S., Eva, E., Lu, G., et al., 2020. Evidence for a serpentinized plate interface favouring continental subduction, *Nature communications*, **11**(1), 1–8.
- Zhu, H. & Tromp, J., 2013. Mapping tectonic deformation in the crust and upper mantle beneath europe and the north atlantic ocean, *Science*, **341**(6148), 871–875.

Appendices

Chapter A

Station list: CIFALPS

Table A.1: Station information of the stations selected from the China-Italy-France Alps, CIFALPS, seismic network(Zhao et al., 2016).

Network code	Station code	Latitude	Longitude	Elevation (m)
YP	CT01	44.256200	4.799100	167.0
YP	CT02	44.287300	4.913900	164.0
YP	CT03	44.324400	5.027500	450.0
YP	CT04	44.371000	5.147700	454.0
YP	CT05	44.370500	5.267700	575.0
YP	CT06	44.382400	5.387200	745.0
YP	CT07	44.410500	5.517000	877.0
YP	CT08	44.411900	5.605100	901.0
YP	CT09	44.429500	5.714400	776.0
YP	CT10	44.437300	5.794000	895.0
YP	CT11	44.453700	5.902600	1037.0
YP	CT12	44.475100	5.982600	1007.0
YP	CT13	44.459600	6.055900	687.0
YP	CT14	44.460900	6.137500	725.0
YP	CT15	44.469300	6.236200	805.0
YP	CT16	44.477100	6.314000	1086.0
YP	CT17	44.504100	6.357600	1174.0
YP	CT18	44.500600	6.455500	1188.0
YP	CT19	44.540900	6.519800	1226.0
YP	CT20	44.585400	6.538900	1128.0
YP	CT21	44.654000	6.568590	1171.0
YP	CT22	44.666300	6.624800	1067.0
YP	CT23	44.664200	6.684800	1531.0

Table A.1 continued from previous page

Network code	Station code	Latitude	Longitude	Elevation (m)
YP	CT24	44.728800	6.744900	1598.0
YP	CT25	44.725500	6.770500	1586.0
YP	CT26	44.765000	6.804200	1733.0
YP	CT27	44.766200	6.879900	1983.0
YP	CT28	44.795400	6.923700	1684.0
YP	CT29	44.774200	6.954800	1671.0
YP	CT30	44.773200	7.039300	1789.0
YP	CT31	44.798200	7.081400	1006.0
YP	CT32	44.809100	7.130100	780.0
YP	CT33	44.825000	7.201000	760.0
YP	CT34	44.827500	7.258100	626.0
YP	CT35	44.921400	7.332900	430.0
YP	CT36	44.989400	7.394700	371.0
YP	CT37	45.035000	7.496700	438.0
YP	CT38	45.018600	7.748400	463.0
YP	CT39	45.072300	7.792800	589.0
YP	CT40	45.069300	7.917000	460.0
YP	CT41	45.086600	8.042600	479.0
YP	CT42	45.099000	8.172900	359.0
YP	CT43	45.092200	8.317300	282.0
YP	CT44	45.065700	8.426500	230.0
YP	CT45	45.044100	8.542500	0.0
YP	CT46	44.989000	8.668700	0.0

Chapter B

Station list: AASN

Table B.1: Station information of the stations selected from the AlpArray Seismic Network (AlpArray Seismic Network, 2015).

Network code	Station code	Latitude	Longitude	Elevation (m)
Z3	A151A	48.882000	6.379850	214
Z3	A152A	48.724800	6.853920	279
Z3	A153A	48.318000	4.796800	238
Z3	A154A	48.441700	5.515230	352
Z3	A155A	48.431200	6.084040	501
Z3	A156A	47.946700	4.534100	380
Z3	A157A	48.0025	5.73258	444.0
Z3	A157B	47.992900	5.799340	359
Z3	A158A	48.004400	6.347000	622
Z3	A159A	47.643900	4.317890	366
Z3	A160A	47.690800	5.050200	465
Z3	A161A	47.583500	6.010800	272
Z3	A162A	47.305500	4.579350	567
Z3	A163A	47.197000	5.201020	222
Z3	A164A	47.104200	5.810400	272
Z3	A165A	46.910200	3.498400	271
Z3	A166A	46.981600	4.147980	580
Z3	A166B	46.9821	4.14769	580.0
Z3	A167A	46.746900	5.319510	203
Z3	A168A	46.560400	3.932900	125
Z3	A169A	46.596300	4.581830	300
Z3	A170A	46.378100	3.447400	140
Z3	A171A	46.200800	4.112500	378

Table B.1 continued from previous page

Network code	Station code	Latitude	Longitude	Elevation (m)
Z3	A172A	46.385800	5.213200	273
Z3	A172B	46.4101	5.26468	271.0
Z3	A173A	46.329600	6.680800	1030
Z3	A174A	45.992600	4.461900	625
Z3	A175A	45.942700	5.074700	315
Z3	A176A	45.717800	4.066600	410
Z3	A177A	45.596300	4.608600	520
Z3	A178A	45.8107	6.2004	0.0
Z3	A178B	45.6877	6.30458	895.0
Z3	A179A	45.472300	2.972200	1084
Z3	A180A	45.311300	4.042700	845
Z3	A181A	45.380500	6.302000	1305
Z3	A182A	44.969500	2.806900	880
Z3	A183A	45.010700	3.663000	1107
Z3	A184A	44.892000	4.451600	750
Z3	A185A	45.120900	5.072800	420
Z3	A186A	44.7932	5.5891	978.0
Z3	A186B	44.793000	5.589200	978
Z3	A187A	44.734300	3.339800	935
Z3	A188A	44.600100	3.936700	1085
Z3	A190A	44.324600	2.869500	940
Z3	A191A	44.319300	3.537800	950
Z3	A192A	44.506900	4.586900	249
Z3	A192B	44.5006	4.57526	179.0
Z3	A193A	44.371200	5.147620	390
Z3	A194A	44.393300	6.502300	1255
Z3	A195A	43.975200	2.719300	290
Z3	A196A	44.051500	4.528000	259
Z3	A198A	43.600600	2.800400	720
Z3	A199A	43.743800	3.688300	341
Z3	A200A	43.692700	4.188500	61
Z3	A201A	43.500600	4.791700	5
Z3	A202A	43.502500	3.260200	212
Z3	A204A	43.241300	5.609900	512
Z3	A205A	43.200100	6.233500	384
Z3	A206A	43.219700	6.601000	363
Z3	A210A	48.827700	5.922540	622
Z3	A211A	48.407100	6.619520	279

Table B.1 continued from previous page

Network code	Station code	Latitude	Longitude	Elevation (m)
Z3	A212A	48.093100	5.044400	358
Z3	A213A	47.496700	5.479900	282
Z3	A214A	46.362000	5.800300	476
Z3	A215A	45.430700	5.232260	450
Z3	A216A	44.429100	5.549890	1245
Z3	A217A	44.370100	6.073300	1087
Z3	A060A	47.0305	7.8904	1112.1
Z3	A060B	46.993	7.97764	1049.1
Z3	A061A	47.09835	8.92522	914.0
Z3	A062A	46.1808	9.1126	1733.2
Z3	A280A	44.5391	7.9089	288.0
Z3	A281A	44.8534	7.7099	292.0
Z3	A282A	45.2545	7.6133	428.0
Z3	A283A	45.2296	8.3208	185.0
Z3	A283B	45.238	8.2885	195.0
Z3	A284A	45.1371	9.3837	99.0
Z3	A285A	44.8939	9.9098	152.0
Z3	A286A	45.366	8.8338	170.0
Z3	A287A	45.6225	8.361	423.0
Z3	A288A	46.0082	8.4818	1306.0
Z3	A289A	46.0473	9.761	1780.0
Z3	A300A	45.819313	13.127954	6.0
Z3	A301A	45.619781	12.620993	2.0
Z3	A302A	45.63353	11.971315	26.0
Z3	A303A	45.344273	12.31822	11.0
Z3	A304A	45.016739	12.033501	1.0
Z3	A305A	44.959236	12.432347	-3.0
Z3	A306A	44.535919	10.596118	463.0
Z3	A307A	44.660755	11.436312	9.0
Z3	A308A	44.582485	12.005684	-2.0
Z3	A309A	44.170353	12.244515	32.0
Z3	A312A	45.10738	10.481657	30.0
Z3	A313A	45.313467	10.662822	64.0
8D	LULY1	46.1831	6.06823	414.5
8D	LULY2	46.13879	6.03344	446.5
8D	LULY3	46.15266	6.12702	478.5
C4	CERN1	46.235876	6.054836	356.3
C4	CERN5	46.309893	6.07608	418.2

Table B.1 continued from previous page

Network code	Station code	Latitude	Longitude	Elevation (m)
C4	CERNS	46.266947	6.066212	463.2
CH	ACB	47.58772	8.25474	468.0
CH	AIGLE	46.34176	6.95295	785.0
CH	BALST	47.33599	7.69485	860.0
CH	BERGE	47.87161	8.17798	963.0
CH	BNALP	46.87034	8.4249	1549.0
CH	BOURR	47.39364	7.2301	846.8
CH	BRANT	46.938011	6.47298	1145.0
CH	DAGMA	47.230884	8.012475	560.0
CH	EMBD	46.21652	7.83223	1180.0
CH	EMING	47.89519	8.84676	619.0
CH	EMMET	47.43757	8.01358	740.0
CH	FIESA	46.435268	8.11043	2338.0
CH	FULLY	46.15633	7.13579	603.0
CH	FUSIO	46.45481	8.6629	1460.0
CH	GIMEL	46.53364	6.26545	1094.0
CH	GRIMS	46.578146	8.318864	1746.0
CH	GRYON	46.25053	7.11106	1282.0
CH	HASLI	46.756809	8.15117	1280.0
CH	ILLEZ	46.21934	6.94038	1395.0
CH	JAUN	46.63395	7.29096	1658.0
CH	LADOL	46.43213	6.13151	1455.0
CH	LAUCH	46.41554	7.77166	2160.0
CH	LKBD2	46.37455	7.64433	2128.0
CH	MESRY	46.346559	6.30842	425.7
CH	METMA	47.71217	8.25262	671.0
CH	MMK	46.0507	7.96409	2200.0
CH	MTI02	47.37927	7.16525	508.0
CH	MUO	46.96765	8.63706	1920.0
CH	NALPS	46.595121	8.74828	2345.68
CH	OTER1	47.57732	7.604136	253.0
CH	PERON	46.19107	5.90792	707.5
CH	ROTHE	47.47612	7.92093	681.0
CH	SAIRA	47.30267	7.08645	966.0
CH	SALAN	46.14415	6.97302	1881.3
CH	SALEV	46.06019	6.09704	1083.6
CH	SAVIG	46.065923	5.973429	529.0
CH	SENIN	46.36335	7.2993	2035.0

Table B.1 continued from previous page

Network code	Station code	Latitude	Longitude	Elevation (m)
CH	SIMPL	46.23962	8.01958	1930.0
CH	SLE	47.7645	8.49236	648.0
CH	SULZ	47.52753	8.11187	668.0
CH	TORNY	46.77363	6.95874	710.0
CH	TRULL	47.6487	8.68161	525.0
CH	VANNI	46.21006	7.59678	1520.0
CH	VINZL	46.45175	6.27815	553.0
CH	WGT	47.09838	8.92525	913.9
CH	WILA	47.41483	8.9077	853.0
CH	WIMIS	46.66488	7.62418	770.0
CH	WOLEN	46.9978	7.36878	623.0
CH	ZUR	47.36921	8.58088	510.0
GU	BHB	44.8355	7.263	576.0
GU	BLANC	45.8444	6.934	3279.0
GU	BURY	43.7825	7.557	18.0
GU	CANO	44.2075	8.2372	590.0
GU	CIRO	45.6019	7.5681	2462.0
GU	ENR	44.2294	7.4182	1114.0
GU	GBOS	44.2416	7.8399	845.0
GU	LSD	45.4596	7.1339	2271.0
GU	MGRO	44.0426	7.8082	1690.0
GU	PCP	44.5413	8.5455	772.0
GU	PZZ	44.5065	7.1157	1397.0
GU	REMY	45.8378	7.1565	2390.0
GU	RNCA	44.4711	8.9512	193.0
GU	RORO	44.1125	8.0667	246.0
GU	ROTM	44.8493	8.3523	186.0
GU	RRL	44.921	6.79	2086.0
GU	RSP	45.1482	7.2649	1265.0
GU	SATI	45.8754	7.8685	2935.0
GU	STV	44.2451	7.3263	968.0
GU	TRAV	45.5122	7.7461	973.0
IV	MONC	45.0739	7.9271	480.0
IV	MRGE	45.76975	7.06101	1660.0
IV	QLNO	44.32425	8.34592	547.0
IV	SARZ	44.867306	8.913604	266.0
IV	VARE	45.867695	8.77	1219.0
MN	BNI	45.052	6.678	1395.0

Acknowledgements

Thank you very much Andrea Morelli for giving me the opportunity to be one of your doctoral students. I will be forever grateful for your knowledge, patience, the freedom to explore and guidance during the uncertain periods. My thankfulness goes also out to my co-supervisor Maria Elina Belardinelli for her support and knowledge. Furthermore, I thank Lapo Boschi and György Hetényi for reviewing my PhD thesis and their constructive feedback.

I thank Martin Schimmel for the useful and inspiring discussions; and for the kind hospitality during my two weeks abroad at the Institute of Earth Sciences Jaume Almera in Barcelona, (ICTJA). The stay was very short due to the pandemic but the research and guidance made a lasting impact.

I would like to thank my colleagues of the *80/90's rooms* at the Istituto Nazionale di Geofisica e Vulcanologia di Bologna (INGV); Anderlini Letizia, Almagro Vidal Carlos, Elisa, Massaro Silvia, Pintori Francesco, Sgattoni Giulia. The research period would not have been as fun without our lunch, coffee and dinner breaks. I wish to thank Simone Salimbeni and Irene Molinari for their constructive feedback and help provided in the beginning of acquiring the data.

I am also grateful to the operators of the French Seismologic and Geodetic Network for managing and making the data freely available at the Résif Seismological data portal. In addition, I thank the operators of the European seismic networks who make their data available through the ORFEUS data center, EIDA.

I am extremely grateful to my mother who transformed into the *helpful grandmother* during the summer months. I thank my father and brother who supported me from far away and also my husband's parents for their kind support.

At last, I cannot begin to express my thanks to my husband, Marco. He endured alongside me all the joys and hardships the past 5 years have brought us, and helped me to pursue this PhD. Our kids, Isabella and Cesare, made sure that this experience became even more special by reminding me every day to live in the present and enjoy the little things in life. Thank you my little ones.

Never let the future disturb you. You will meet it, if you have to, with the same weapons of reason which today arm you against the present.

—Marcus Aurelius

Curriculum Vitae

Tahira Nicole Ashruf

Born 01 December 1990 in Suriname — Nationality: Surinamese

Nov. 2017 - 2022 **Doctoral candidate in Geophysics**

University of Bologna

Financed by the National Institute of Geophysics and Volcanology

June 2021 - Nov. 2021

Maternity leave second child

Jan. 2018 - Jan. 2019

Maternity leave first child

2015 - 2017 **Lecturer Anton de Kom University of Suriname**

Teaching: Geophysics and Geophysical Exploration,

to undergraduate students in mineral resource and management.

2013 - 2015 **IDEA League Joint Master's in Applied Geophysics**

TU Delft, ETH Zürich, RWTH Aachen

Thesis: Surface Wave analysis for the characterization of granular materials

Internship: Total EP - Netherlands

2008 - 2011 **B.Sc. Mineral Resource and Management**

Anton de Kom University of Suriname

Thesis: Static model of the Uitkijk T2 reservoir

Internship: Paradise Oil Company (Stateoil) - Suriname

Peer reviewed article

Ashruf, T.N. & Morelli, A., 2022. The Moho reflectivity of the subduction beneath the Southwestern Alps from ambient seismic noise autocorrelations, *Geophysical Journal International*, **230**(1), 298–316, doi:10.1093/gji/ggac079